Theoretical Studies on Structure, Dynamics, and Membrane Insertion of Polytheonamide B

Mahroof KALATHINGAL

Department of Functional Molecular Science

School of Physical Sciences

The Graduate University for Advanced Studies, SOKENDAI

September 2021

Contents

Chapter 1

Introduction

The dynamic processes in living cells result from conformational fluctuations and changes in biological macromolecules such as proteins. These biomolecular dynamics are complex and fascinating, occurring on a wide range of timescales from subpicoseconds to seconds and longer. Experimental studies can provide comprehensive structures of various biological macromolecules. However, experiments alone are incapable of revealing how the structures of individual molecules change on short time scales, and the molecular mechanisms of fast processes such as enzymatic reactions and ion transport through biological channels. Molecular dynamics (MD) simulations can fill these gaps by dissecting key interactions, reactions, changes and fluctuations, and movements that are important in determining the specific biological activity. The utility of MD simulations strongly depends on the accessible time scales and the accuracy of the force fields used. Despite these limitations, the MD simulations can reveal the protein structure and dynamics in atomic detail, which are difficult to be obtained from experiments. Herein, the structure and dynamics in model transmembrane peptide, polytheonamide B (pTB), are investigated theoretically using all-atom MD simulations.

The pTB is a potent cytotoxic peptide obtained from the marine sponge *Theonella swinhoei*. The pTB consists of 48-residues and is the most heavily posttranslationally modified biomolecule known at present. The potent cytotoxicity of pTB is related to its channel-forming activity across the target cell membrane by spontaneously inserting into the membrane. The prefolding of the 48-residue long right-handed $\beta^{6.3}$-helix occurs

in the aqueous environment before insertion. The alternate D- and L-amino acids throughout the sequence allow the peptide to take a right-handed $\beta^{6.3}$-helical conformation, similar to the gramicidin A (gA) channel. There are eight types of unnatural amino acids in pTB: β-hydroxyvaline (Hva), *tert*-leucine (Tle), γ-N-methylasparagine (Asm), γ-N-methyl-*threo*-β-hydroxyasparagine (Ham), β-methylglutamine (Mgn), β-methylisoleucine (Mil), β,β-dimethylmethionine sulphoxide (Mme), and *allo*-threonine (aTh). Also, the hydrophobicity of residues decreases gradually from the N-terminal to the C-terminal. The long and short side chain – side chain hydrogen bond strands outside the pore reinforce the stability of the long $\beta^{6.3}$-helix of pTB. Structural features suggest that the pTB inserts into the membrane led by the hydrophobic N-terminal and stays in the membrane stably. The highly hydrophobic N-terminal blocking group, 5,5-dimethyl-2-oxo-hexanoyl (Mhe), is thought to anchor the spontaneous "vectorial insertion" of pTB into the target cell membrane. The 40 Å long pTB can readily span the membrane as a monomeric channel and allows the permeation of monovalent cations with the ionic current in the order of $H^+ > Cs^+ > Rb^+ > K^+ > Na^+ > Li^+$. In the present Ph.D. thesis, the structure, fluctuations, and dynamics of pTB channel and solvent molecules inside the channel in different environments; and the energetics and dynamics of membrane insertion of pTB are investigated theoretically at the molecular level.

It has been suggested that the collective dynamics of water molecules inside ionic channels have a significant role in permeating ions through the channels. Therefore, in Chapter 2, as a first step toward understanding the ion permeation mechanism of the pTB channel, the structure, fluctuation, and dynamics of pTB itself and solvent molecules inside pTB in three different environments, water, POPC bilayer, and 1:1 chloroform/methanol mixture, are investigated. Since there are eight non-standard residues in pTB, the molecular parameters for these residues are developed prior to the

MD simulations. The newly determined parameters are validated by comparing the average structure of pTB calculated in the mixed solvent with the NMR-derived structure in the mixed solvent. The current study reveals that the water molecules inside the pTB channel show collective motions, both translationally and orientationally, due to the strong hydrogen bonds between neighboring water molecules. It is found that the motions of methanol molecules inside the channel are not correlated because of the absence of strong hydrogen bonds between adjacent methanol molecules.

In Chapter 3, the spontaneous membrane insertion of pTB, which is important for understanding its cytotoxicity, is investigated. The process of spontaneous membrane insertion of transmembrane peptides is crucial for toxin actions, viral infections, and antimicrobial defense. The understanding of the mechanism of membrane insertion is essential for the development of novel therapeutic drugs against bacterial and viral infections. However, the mechanism of this process is not clearly understood yet. The pTB is one such potent cytotoxic peptide that spontaneously inserts into the target cell membranes, and is an ideal model transmembrane peptide to explore the underlying molecular mechanism of the insertion process. The free energy calculations using the replica-exchange umbrella sampling simulations present an energy cost of 4.3 kcal/mol located at the membrane surface for the membrane uptake of pTB from bulk water. The simulation results support the experimental observation of the spontaneous membrane insertion of pTB led by the hydrophobic N-terminal. It is found that the insertion of pTB proceeds with only the local lateral compression of the membrane, in three successive phases: “landing,” “penetration,” and “equilibration” phases. Depending on whether or not pTB is trapped in the upper leaflet of the membrane during the penetration phase, the insertion process can occur in two possible pathways, namely “trapped” and “untrapped” insertions. The mechanism of the spontaneous “vectorial insertion” of pTB can be exploited to design new peptides and therapeutic drugs of

similar features.

The studies summarized in this thesis do not only deepen the understanding of pTB and its cytotoxicity, but also, and more importantly, can provide useful insights to understand other single transmembrane peptides prefolded in aqueous solution and their spontaneous vectorial insertion into the membrane. These theoretical studies reveal that anchoring by the N-terminal hydrophobic group (Mhe) from aqueous solution to the membrane surface is crucial for the subsequent membrane insertion, which arises from the asymmetric structure of pTB, i.e., the hydrophobicity of residues decreases gradually from the N-terminal to the C-terminal. This finding reinforces the importance of membrane anchoring for the vectorial insertion. As for the cytotoxic action of pTB, the membrane insertion is followed by the ion channel activity across the cell membrane.

Chapter 2

Structure and Dynamics of Solvent Molecules inside Polytheonamide B Channel in Different Environments: A Molecular Dynamics Study

Introduction

Polytheonamide B (pTB), a potent cytotoxic channel-forming peptide obtained from the marine sponge *Theonella swinhoei*, has been widely studied due to its unique characteristics.[1–17] The pTB consists of 48-residues and is the most heavily posttranslationally modified biomolecule known at present, i.e., 28 of its total residues are altered.[9,15,16] The pTB has several unique structural features.[4,5,12,14] First, pTB has alternate D- and L- amino acids throughout the sequence as shown in Fig. 2-1a, which permit the peptide to take a right-handed $\beta^{6.3}$-helical conformation similar to formerly well-studied antibiotic gramicidin A (gA).[18] Second, there are eight types of unnatural, i.e., non-proteinogenic, amino acids in pTB: β-hydroxyvaline (Hva), *tert*-leucine (Tle), γ-N-methylasparagine (Asm), γ-N-methyl-*threo*-β-hydroxyasparagine (Ham), β-methylglutamine (Mgn), β-methylisoleucine (Mil), β,β-dimethylmethionine sulphoxide (Mme), and *allo*-threonine (aTh). As a result, 23 residues in pTB are the unnatural amino acids. Third, the N-terminal is capped by a highly hydrophobic 5,5-dimethyl-2-oxo-hexanoyl (Mhe) group. Moreover, the hydrophobicity of residues decreases gradually from the N-terminal to the C-terminal.

The pTB channel has unique tertiary structural features.[4,5,12,14] The pTB has a long side chain – side chain hydrogen bond (SSHB) strand outside the pore, starting from the middle of the N-terminal half up to the C-terminal, as seen in Fig. 2-1b. The long SSHB strand, formed between the side chain amide groups of Asm-15, 21, 27, 33, 39 and Asn-45, runs parallel to the channel axis, and covers two-thirds of the total length of the pTB channel. The pTB also has two short SSHB strands near the C-terminal located on the opposite side of the long SSHB strand, formed between Ham-29 and Asm-35 and between Ham-37 and Asn-43. All Asm and Ham residues having posttranslational N-methylation of the side chain amide groups are involved in the SSHBs.

The potent cytotoxicity of pTB is related to its channel forming activity across the target cell membranes.[2,5] Structural features suggest that pTB inserts into the membrane lead by the hydrophobic N-terminal (vectorial insertion).[5,13,17] The 40 Å long pTB channel can readily span the membrane as a monomeric channel, and stays in the membrane stably.[5,12,14] With an inner pore diameter of 4 Å, pTB allows permeation of monovalent cations with the selectivity sequence of $H^+ > Cs^+ > Rb^+ > K^+ > Na^+ > Li^+$, which has been examined using the planar lipid bilayer methods.[2,5,12,14] Single-channel current recordings further revealed the rectified conduction for these cations.[14]

Only two theoretical and computational studies on the pTB channel have been reported till now. The normal mode analysis by Mori et al.[8] has suggested that the pTB channel employs a similar ion permeation mechanism, i.e., the libration mechanism, as that of the gA channel. The molecular dynamics (MD) study by Renevey and Riniker[16] has found that the posttranslational N-methylation of Asm and Ham residues are vital in stabilizing the hydrogen-bonded chains outside the pore, thereby providing an "exoskeleton" for the $\beta^{6.3}$-helix.

a)

Gly[1]-L-Mil-Gly-L-Tle-D-Tle-L-Tle-D-Ala-L-Tle-D-Tle-
L-Ala-Gly-L-Ala-D-Tle-L-Ala-D-Asm-L-Hva-Gly-L-Ala-
Gly-L-Tle-D-Asm-L-Mgn-D-Hva-L-Ala-Gly-Gly-D-Asm-
L-Ile-D-Ham-L-Tle-D-Hva-Gly-D-Asm-L-Ile-D-Asm-
L-Val-D-Ham-L-Ala-D-Asm-L-Val-D-Ser-L-Val-D-Asn-
L-Mme-D-Asn-L-Gln-D-aTh-L-Thr[48]

b)

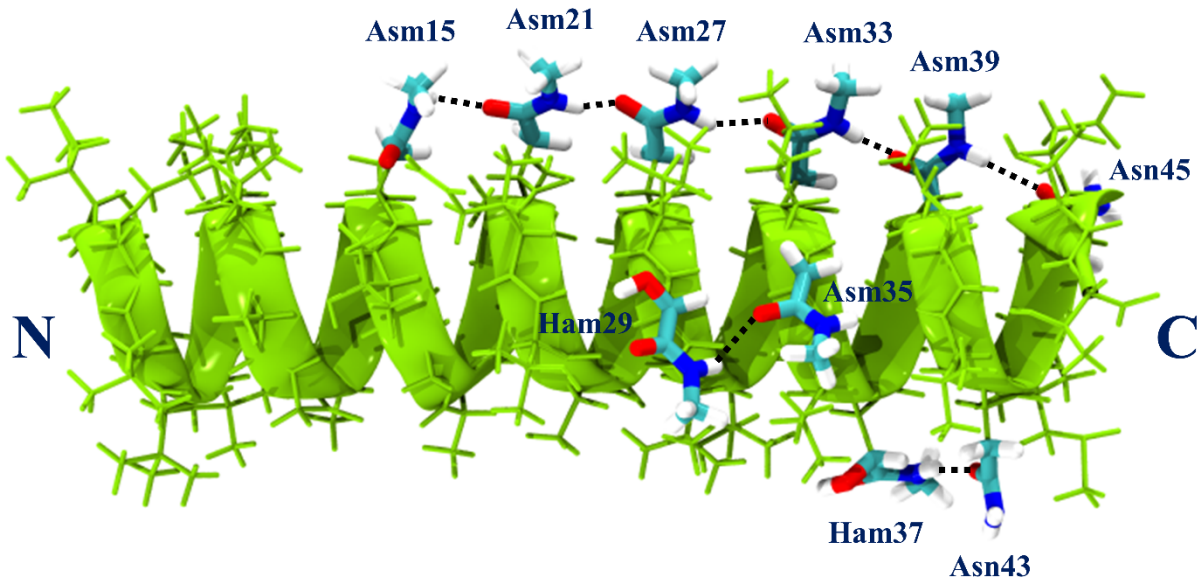

Figure 2-1: Structure of Polytheonamide B (pTB). **(a)** Primary structure of pTB. The residues shown in green, red, and blue are Glycine, D-type, and L-type residues, respectively. The residues are numbered from the N-terminal to the C-terminal. **(b)** The right-handed $\beta^{6.3}$-helical backbone of pTB is shown as a green ribbon and side chains as thin green stick models. The thick stick models represent the side chains of residues involved in the side chain – side chain hydrogen bonds, which are labeled with their residue numbers. The black dots indicate hydrogen bonds.

In this study, the $\beta^{6.3}$-helical channel of pTB is examined in water, POPC bilayer, and 1:1 chloroform/methanol mixture using all-atom MD simulations. The average structures of the pTB channel in the three environments are analyzed, for example, in

terms of the channel length, inner pore diameter, and backbone dihedral angles (ϕ,ψ). The validation of the parameters used for the non-standard groups in pTB is performed by comparing the average structural properties of pTB in the mixed solvent with the experimental structure obtained in the mixed solvent. To understand the fluctuations of the $\beta^{6.3}$-helix of pTB, I calculate the root mean square displacements (RMSD) of the backbone atoms with respect to the NMR-derived structure and the B-factors for the backbone atoms of each residue in the three environments. The configuration and dynamics of solvent molecules inside the pore are investigated by calculating various quantities, e.g., positional fluctuations, O-H vector orientations, and dipole moment orientations. I find that the water molecules inside the pore show collective motions in which all water molecules tend to orient in the same direction along the channel axis, and translate by one water-water distance at a time, due to the strong hydrogen bonds (HBs) between neighboring water molecules. It is suggested that such a collective behavior of water molecules inside the pore are indispensable in understanding the ion permeation mechanism of the pTB channel. On the other hand, the motions of methanol molecules inside the pore are not correlated because of the absence of strong HBs between adjacent methanol molecules.

This chapter is organized as follows. Section 2 describes the methods of system preparation and the simulation details. In Section 3, I present my simulation results for pTB in the three environments and discuss the results using various analyses. Finally, conclusions are given in Section 4.

Methods

In the present study, I examined the equilibrium structures and fluctuations of pTB in three environments, i.e., water, POPC bilayer, and 1:1 chloroform/methanol mixture, using all-atom MD simulations. The force field parameters for the natural amino acids

were taken from the AMBER ff14SB force field.[19] The TIP3P model was used for water molecules.[20] The POPC bilayer parameters were taken from the Lipid14 force field.[21] The parameters developed by Cieplak et al. were used for chloroform molecules.[22] The methanol parameters were taken from the work by Caldwell and Kollman.[23] The ions were modeled using the monovalent ion parameters developed by Joung and Cheatham.[24]

As mentioned in Introduction, pTB has eight kinds of non-proteinogenic amino acids, and the N-terminal is capped with a hydrophobic group. Thus, the parameters for the non-standard groups (Hva, Tle, Asm, Ham, Mgn, Mil, Mme, and Mhe) are obtained by following the AMBER protocol.[25] Note that I parametrize the non-standard groups in pTB for use with the AMBER force filed, while Renevey and Riniker,[16] and Mori et al.[8] have already parametrized the pTB for use with the GROMOS and CHARMM force fields, respectively. The parameters for aTh are the same as those of Thr as they are stereoisomers of each other. The atomic point charges for the non-standard groups are evaluated using the multi-conformational RESP protocol[26] (See Figs. S2-1 and S2-2 of Supporting Information for the details of point charges on each non-standard group). The obtained charges for the unnatural amino acids are found to be similar to the corresponding precursor amino acids except for the modified groups. The bond, angle, torsion, and van der Waals parameters for the non-standard groups are determined based on atom-type similarity with the existing residues in the AMBER ff14SB[19] and the GAFF[27] force fields. Since the parametrization strategy of all the basis force fields (Water, Chloroform, Methanol, Ions, Lipid, and non-standard groups in pTB) used in this study are consistent with the approach used in constructing the standard AMBER force field, I assume that all these basis force fields are compatible with each other.

All MD simulations were performed at three-dimensional periodic boundary conditions using AMBER14 package.[28] The bonds involving hydrogen were constrained using the SHAKE algorithm,[29] enabling a time step of 2 fs. Long-range electrostatic interactions were taken into account using the particle mesh Ewald approach[30] with a real space cutoff of 12 Å. The initial structure of pTB was taken from the NMR structure (PDB entry: 2RQO).[4]

In the calculation of pTB in water, the system was comprised of one pTB molecule, 9757 water molecules, and one Cs^+ ion added for balancing the net charge of the deprotonated C-terminal residue, resulting in a total of 29999 atoms. The Cs^+ ion was chosen because of its high ionic conductivity in the planar lipid bilayer experiments of the pTB channel.[5,12] In the calculation of pTB in POPC bilayer, the system was made up of one pTB molecule, 120 POPC lipid molecules, 8311 water molecules, 27 Cs^+ ions and 26 Cl^- ions, resulting in a total of 41793 atoms. For the preparation of POPC bilayer, a fully hydrated POPC bilayer having 64 lipid molecules in each layer was first constructed using the CHARMM-GUI Membrane Builder.[31] The generated membrane patch had 35 Å thick hydration layer on each side, and 0.15 M CsCl salt concentration added to the water layers. Subsequently, eight lipid molecules (4 from each layer) from the center of the membrane patch were removed to create a pore, and the equilibrium structure of pTB (obtained from MD simulation of pTB in water) was inserted into that pore. One Cs^+ ion was added for neutralizing the net charge of the deprotonated C-terminal of pTB. In the calculation of pTB in 1:1 chloroform/methanol mixture, the system was composed of one pTB molecule, 1000 chloroform molecules, 2000 methanol molecules, and one Cs^+ ion added for charge neutrality, resulting in a total of 17728 atoms. Since the pKa of the chloroform/methanol mixture is much higher than that of the C-terminal of pTB (pKa for carboxyl part of Thr is 2.63), the C-terminal was in its

deprotonated state, and one Cs^+ ion was added to neutralize the net charge of pTB in 1:1 chloroform/methanol mixture.

For each system, the energy minimization of 10000 steps was performed prior to starting MD simulations. The systems of pTB in water and 1:1 chloroform/methanol mixture were heated from 0 K to 300 K under the NVT condition using the Langevin thermostat[32] with a collision frequency of $\gamma = 1.0$ ps^{-1}. Subsequently, each system was equilibrated for 200 ps under the NPT condition and then for 100 ns under the NVT condition. The pressure was controlled by the isotropic Berendsen barostat[33] (1 atm) with a pressure relaxation time of 1.0 ps at 300 K. The simulation box dimensions of the equilibrated systems of pTB in water and 1:1 chloroform/methanol mixture were 59 × 59 × 86 and 58 × 58 × 83 $Å^3$, respectively. Each equilibrated system was then simulated for 2 μs under the NVT condition and the structural data was recorded every 10 ps. Besides, a separate 10 ns simulation of each equilibrated system under the NVT condition by saving the data every 50 fs was performed to analyze fast dynamics.

The system of pTB in POPC bilayer was initially equilibrated at the NPT condition using anisotropic Berendsen regulation[33] (1 atm) with a pressure relaxation time of 1.0 ps for 35 ns at the relevant experimental temperature of 303 K, as recommended by the original literature on the Lipid14 force field.[21] The equilibration of the system was confirmed by comparing the average area per lipid (APL) from the equilibrium simulations with the APL reported in the recent experimental study (64.3 $Å^2$)[34] and the original literature on the Lipid14 force field (65.6±0.5 $Å^2$).[21] The plus-minus (±) errors refer to the standard deviation in the calculation of the average APL. The average APL calculated from the 35 ns equilibrium simulations is 64.2±0.8 $Å^2$, which is very close to the values reported in the experimental and previous simulation study. Since the APL has converged to the experimental value, the volume and APL of

the system is not expected to change considerably further. Therefore, I decided to switch to the NVT condition in the following equilibration and production runs for computational efficiency. Subsequently, long equilibration run of 2 μs was performed under the NVT condition to ensure the equilibration of the tilt angle of pTB in POPC bilayer. The Langevin thermostat[32] (γ = 1.0 ps^{-1}) was used to maintain the temperature at 303 K. The simulation cell dimensions of the fully equilibrated system were 61 × 61 × 108 $Å^3$. Using the equilibrated system, production runs under the NVT condition were carried out for 2 μs by saving the data every 10 ps. Moreover, a separate 10 ns simulation of the equilibrated system using the NVT condition with data collected every 50 fs was also carried out to analyze fast dynamics. Note that only the production run data of each system was used for the subsequent analyses. The standard CPPTRAJ analysis routines[35] and in-house written scripts were applied for analyses. All snapshot images from the simulations were generated using the Visual Molecular Dynamics package.[36] Note that the atom names used throughout the chapter are those in the NMR PDB file.[4]

Results and Discussions

Average Structures of pTB

I first validated the parameters of the non-standard groups in pTB by comparing the average structure of pTB in 1:1 chloroform/methanol mixture with the NMR resolved structure obtained in the mixed solvent.[4] I evaluated the length of pTB channel defined as the distance between the centers of mass (COMs) of first six Cα atoms at each terminal. The average channel length in the mixed solvent is 32.9±0.4 Å, which is in excellent agreement with the 32.3 Å of the NMR resolved structure. I evaluated the inner pore diameter of pTB defined as the shortest distance excluding the van der Waals

radius from the Cα atoms of residues 7-42 to the line connecting the COMs of Cα atoms of residues 7-12 and 37-42. The first six Cα atoms at each terminal are not considered for the calculation of inner pore diameter. The mean inner pore diameter of pTB in the mixed solvent is 4.4±0.3 Å, which is in good agreement with the inner pore diameter of 4.4 Å of the NMR-derived structure. I calculated the mean backbone dihedral angles (ϕ,ψ) of the D- and L-type residues (the ϕ/ψ angles of first and last residues are excluded from the averages). The average dihedral angles (ϕ,ψ) of the D-type and L-type residues in the mixed solvent are (129.2±18.6°,-108.8±21.4°) and (-121.5±19.8°,127.8±17.3°), respectively. The NMR experimental values in the mixed solvent are (126.0°,-113.2°) and (-125.4°,138.3°) for the D- and L-type residues, respectively.

I then compared a total of 200 experimental NOE proton-proton upper distance bounds of pTB in 1:1 chloroform/methanol mixture[4] with the corresponding average proton-proton distances calculated using $< r^{-6} >^{-\frac{1}{6}}$ from the simulations of pTB in 1:1 chloroform/methanol mixture. A NOE violation is obtained by subtracting the experimental upper distance bound from the corresponding calculated $< r^{-6} >^{-\frac{1}{6}}$ value. As seen in Fig. 2-2, only six violations are observed above the maximal violation of 0.1 Å reported in the NMR structural analysis.[4] Thus, the average structure of pTB calculated in the mixed solvent using the current parameter set is in good agreement with the experimentally determined structure.

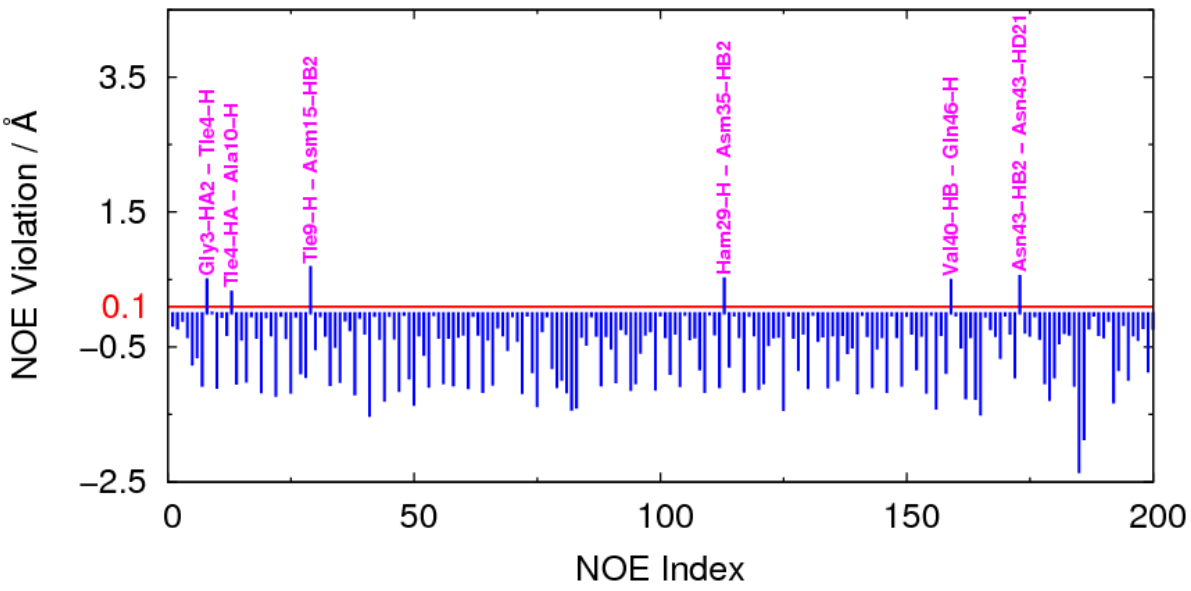

Figure 2-2: Violations of 200 experimental NOE proton-proton upper distance bounds of pTB as a function of NOE sequence number in 1:1 chloroform/methanol mixture calculated using 2 μs data. The maximal violation of 0.1 Å reported in the NMR structural analysis of pTB is marked with a red line. The NOE violations above the maximal violation are labelled using pink labels.

I then examined the average structure of pTB in water and POPC bilayer. The average channel lengths in water and the membrane are 32.5±1.6 and 32.8±0.3 Å, respectively. It is noted that the mean length of pTB in POPC bilayer is close to the mean bilayer thickness of 31.8 Å, calculated as the peak-to-peak distance from the electron density profile of POPC bilayer along the bilayer normal. Therefore, the pTB channel can readily span the membrane and can function as a monomeric channel. The mean inner pore diameter of pTB in both water and the membrane is also 4.4±0.3 Å. The average dihedral angles (ϕ,ψ) of the D-type residues in water and the membrane are (121.9±40.3^o,-103.4±39.8^o) and (128.6±17.3^o,-109.0±19.1^o), respectively; those of the L-type residues in water and the membrane are (-118.4±30.0^o,127.6±26.5^o) and (-121.1±19.1^o,129.9±15.2^o), respectively.

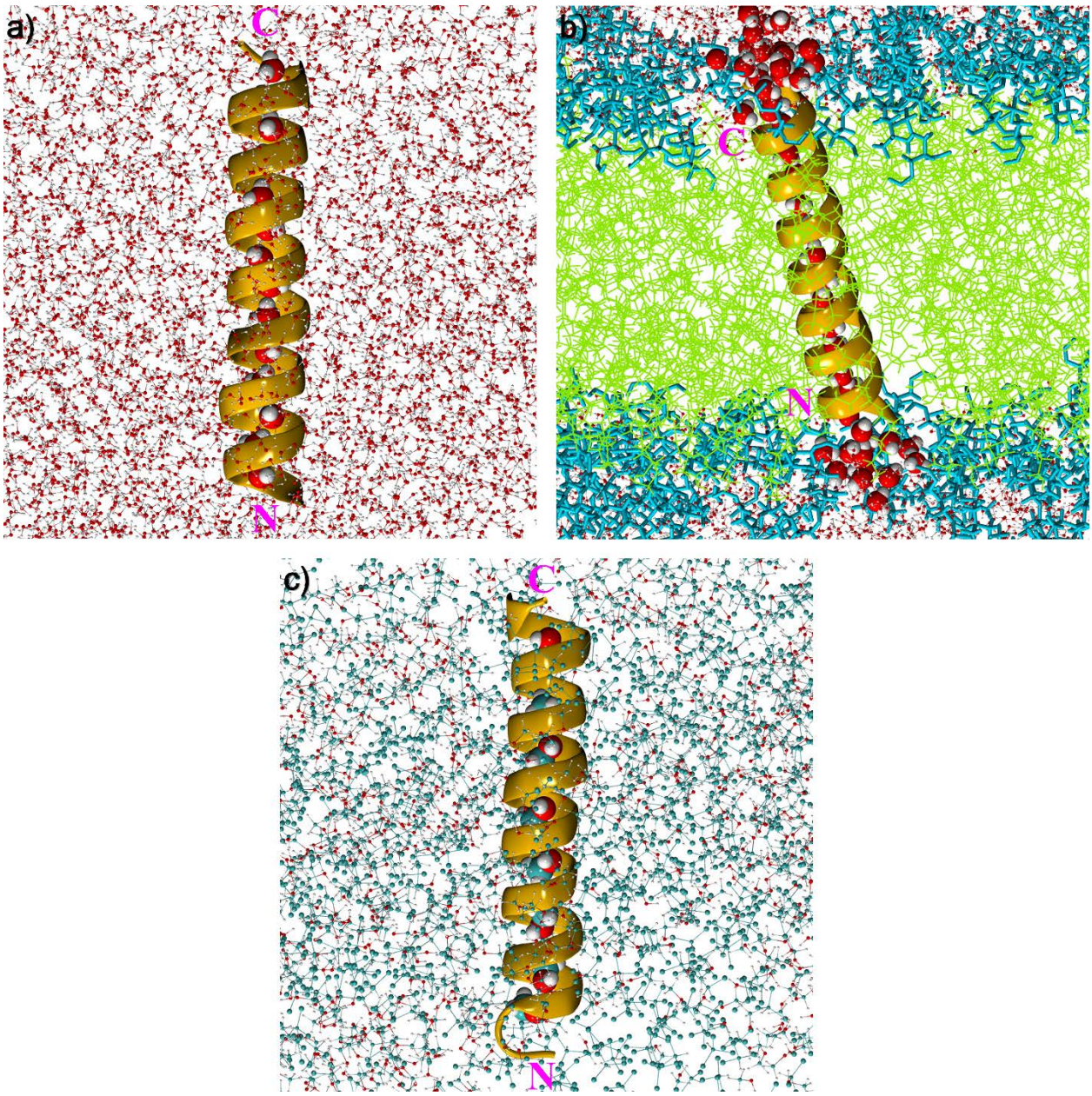

Figure 2-3: Snapshot images of pTB in **(a)** water, **(b)** POPC bilayer, and **(c)** 1:1 chloroform/methanol mixture. The snapshot images are taken after 2 μs of production runs.

It has been suggested from the NMR structural analysis that the SSHBs outside the pore reinforce the stability of the long $\beta^{6.3}$-helix of pTB.[4] Therefore, I examined the SSHBs in the three environments. The hydrogen bond probabilities of the prominent SSHBs are shown in Fig. 2-4a. The criterion for an HB is a maximum donor-acceptor distance of 3.5 Å and a minimum donor-hydrogen-acceptor angle of 135°. The maximum

donor-acceptor distance of 3.5 Å is the position of the first minima in the radial distribution of donor-acceptor distances of prominent SSHBs in pTB. The minimum donor-hydrogen-acceptor angle of 135^{o} is the value used in many previous studies for defining the HBs in proteins.[16] The first five entries in Fig. 2-4a correspond to the SSHBs involved in the longest strand in the order of positions from the N-terminal half to the C-terminal, whereas the remaining two entries correspond to the two short SSHB strands near the C-terminal. It is found that the probabilities of SSHBs at the C-terminal half are higher than those at the N-terminal half (Asm15-NH – Asm21-O and Asm21-NH – Asm27-O), due to the presence of multiple SSHBs at the C-terminal half. The probabilities of Asm39-NH – Asn45-O in all the environments and Ham37-NH – Asn43-O in water are slightly lower than their nearest neighbors because of the breakage of backbone HBs near the C-terminal by surrounding solvent molecules. The present results are consistent with the previous study.[16] The SSHB probabilities decrease in the order of the membrane, the mixed solvent, and water. The relatively low probabilities of SSHBs in both water and the mixed solvent arise from the fact that the HB forming side chains can sometimes make stable HBs with surrounding solvent molecules (water/methanol) instead of another side chain. However, the tendency of SSHB breakage through solvation is low in the mixed solvent compared to that in water, due to the presence of non-polar chloroform molecules. In contrast, when pTB resides inside the membrane, the SSHBs are less disrupted, hence have higher probabilities than the SSHBs of pTB in solutions.

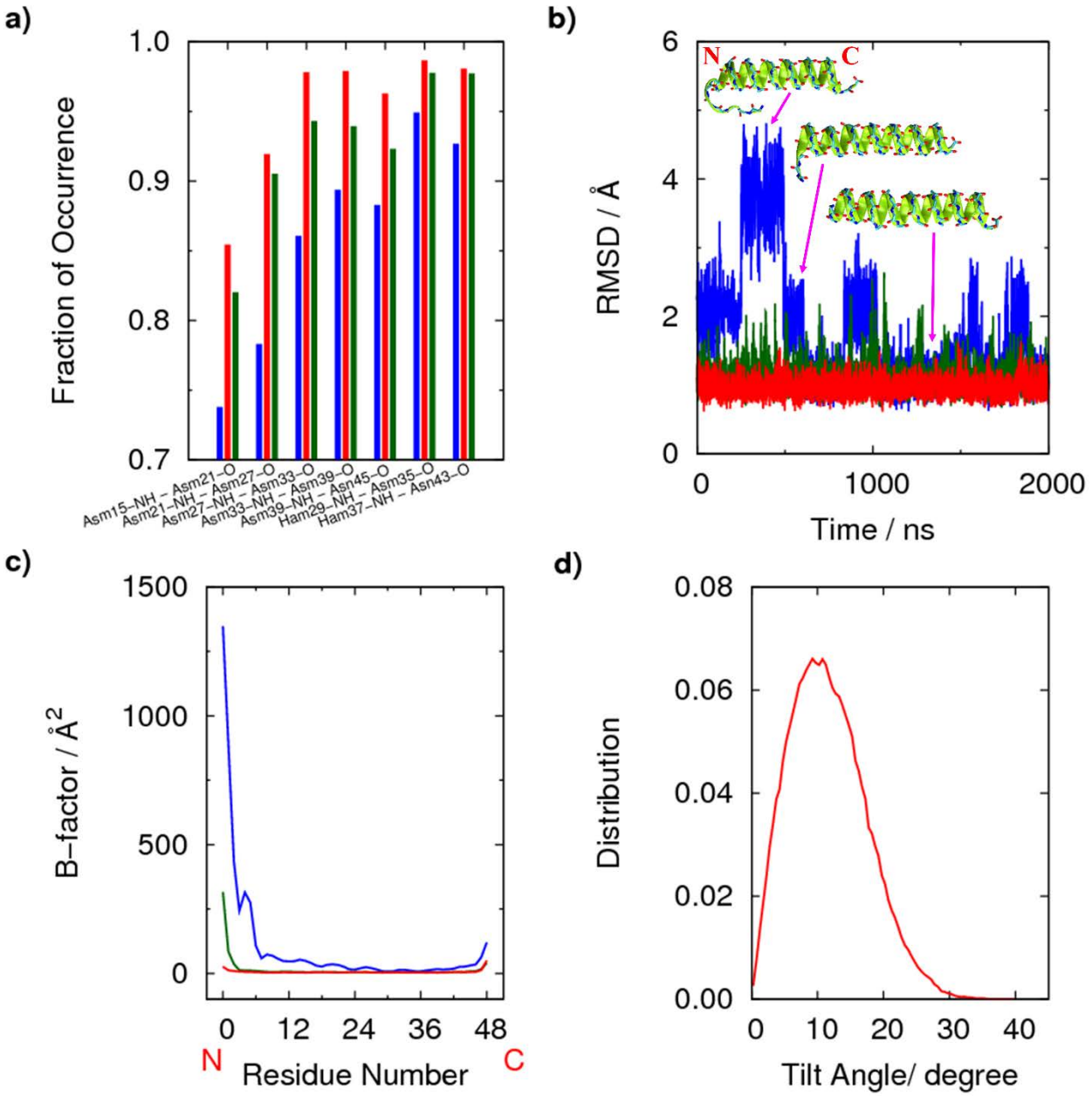

Figure 2-4: Structure and fluctuations of $\beta^{6.3}$-helix in water (blue), POPC bilayer (red), and 1:1 chloroform/methanol mixture (dark-green) from 2 μs data. **(a)** Probabilities of all prominent side chain – side chain hydrogen bonds. **(b)** Positional RMSDs of the backbone atoms with respect to the NMR-derived structure. Three different conformers of pTB in water are also shown: RMSDs of ~ 4.0 Å, ~ 2.5 Å, and ~ 1.0 Å. **(c)** B-factors for the backbone atoms of each residue. Zeroth residue number corresponds to the N-terminal hydrophobic group. **(d)** Distribution of tilt angle of pTB in POPC bilayer.

Structural Fluctuations of pTB

I next analyzed the fluctuations of the $\beta^{6.3}$-helix of pTB. Figure 2-4b shows the RMSD of backbone atom positions (N, Cα, and C) with respect to the NMR resolved structure. The RMSD fluctuations in water, the membrane, and the mixed solvent are in the range of 0.5-5, 0.5-1.7, and 0.5-2.7 Å, respectively. There are at least three different conformations of pTB in water over the course of the simulation as shown in Fig. 2-4b, i.e., RMSDs of ~ 4.0, ~ 2.5, and ~ 1.0 Å. When RMSD is ~ 4 Å in water, the helix near the N-terminal is found to be unfolded: The significantly large RMSD fluctuations in water correspond to the destabilization of the helix due to the breakage of the SSHBs.

To understand residues contributing to the RMSD fluctuations shown in Fig. 2-4b, the fluctuations of individual residues are analyzed in terms of the B-factors, which are defined as $B_f = 8\pi^2(RMSF)^2/3$, where $RMSF$ is the root mean square fluctuation. Figure 2-4c shows the B-factors for the backbone atoms of each residue. The backbone atoms used in the B-factor calculation for amino acid residues are N, Cα, and C, whereas those for the N-terminal hydrophobic group are C1, C2, and C3. The B-factor values in water, particularly for the first 13 residues near the N-terminal including the N-terminal hydrophobic group, are significantly larger than those in the other environments. The high B-factor values near the N-terminal in water arise from the repeat of unfolding and refolding of the helix. The surrounding water molecules can easily break the backbone HBs near the N-terminal by forming stable HBs with the backbone atoms. In the membrane, the fluctuations of the $\beta^{6.3}$-helix are significantly suppressed due to the presence of membrane, and the residues near the C-terminal are slightly more flexible than those near the N-terminal, because the negative charge on the C-terminal residue interacts with the charged lipid head groups. In the mixed solvent, the B-factor values near the N-terminal are also large. It is indeed found in the NMR structural analysis of

pTB[4] that the helix near the N-terminal is less rigid compared to the other parts due to the absence of SSHBs which reinforce the stability of the long helical structure of pTB.

The destabilization of the helix near the N-terminal by surrounding solvent molecules causes the bending of the long cylindrical tube of pTB near the N-terminal. The bend angle was calculated as a measure of the rigidity of the tube. Here, I define the bend angle as the angle between the vectors pointing from the COM of Cα atoms of residues 13 – 18 (the preferred point about which tube bending occurs) to the COMs of first six Cα atoms at each terminal. The average bend angles in water, the membrane, and the mixed solvent are 163.5±20.6^{o}, 175.7±2.2^{o}, and 175.0±2.9^{o}, respectively. The result shows that pTB in water is more bent than in other two environments. The bend angle of the NMR resolved structure[4] obtained in the mixed solvent is 170.6^{o}.

I further analyzed the tilt angle of pTB in the membrane, i.e., the angle the pTB channel makes with the bilayer normal. The distribution of the tilt angle is given in Fig. 2-4d. It is found that the pTB channel is slightly tilted in the membrane with an average tilt angle of 11.6±5.8^{o}, such that the C-terminal end touches the membrane surface and the N-terminal end resides just below the membrane surface (Fig. 2-3b). Moreover, the lipid head groups are sometimes found near the channel openings, which might block the ions from entering the channel during the ion permeation process. It is also found that there are more water molecules near the C-terminal than near the N-terminal in the membrane (Fig. 2-3b).

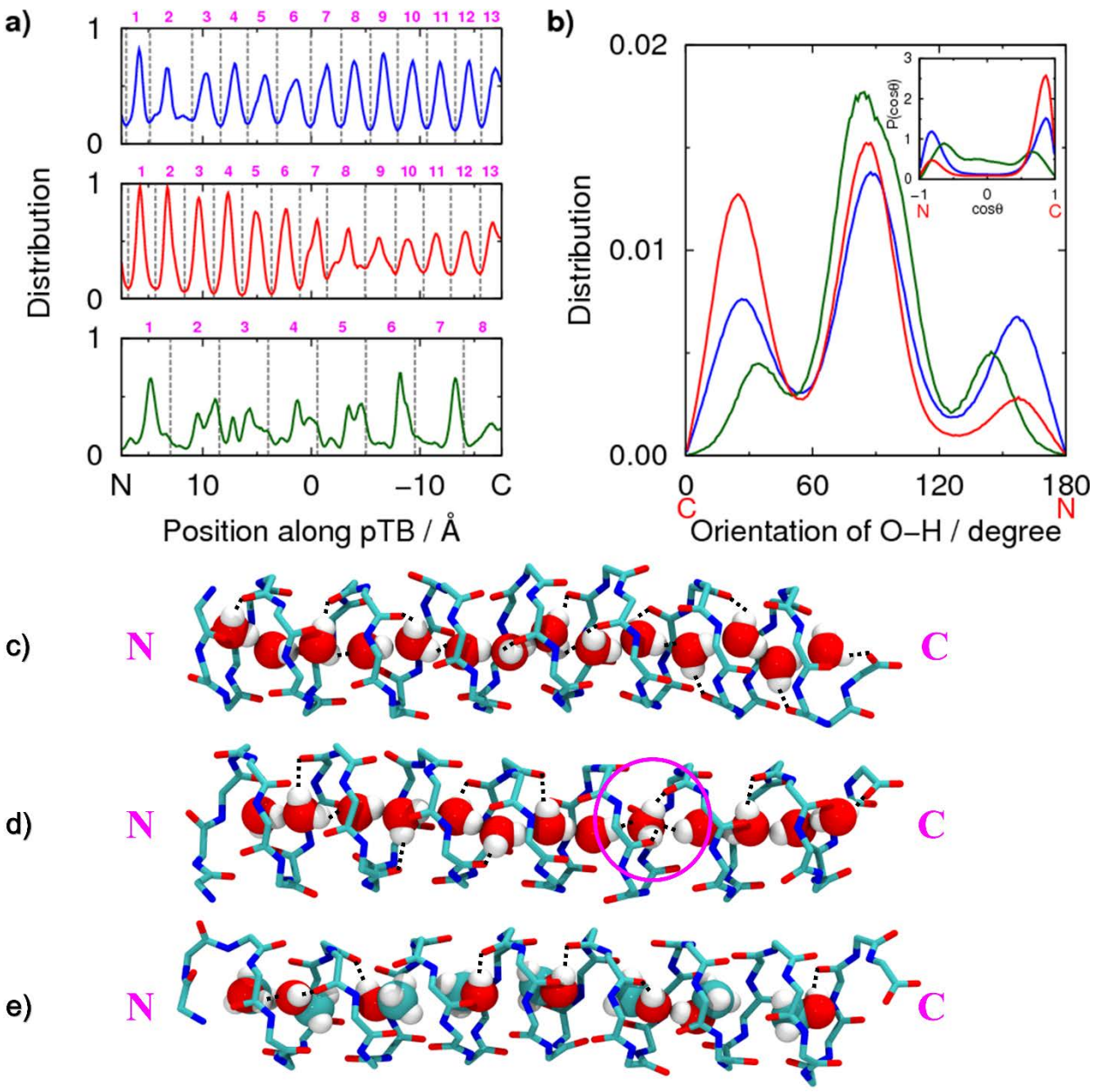

Figure 2-5: Positions and orientations of solvent molecules inside the pore in water (blue), POPC bilayer (red), and 1:1 chloroform/methanol mixture (dark-green) calculated using 1.5 μs data in water, and 2 μs data in both the membrane and the mixed solvent. **(a)** Occupancy distributions along the channel axis for solvent molecules inside the pore. Individual sites are separated using gray dashed lines and are numbered from the N-terminal side to the C-terminal side using pink labels. **(b)** Distributions of O-H vector orientations about the channel axis. Distributions of individual dipole moment orientations along the channel axis are shown in the inset. Cosine values -1 and 1 represent the orientations toward the N- and C-terminals, respectively. Hydrogen bond structures of solvent molecules inside the pore in **(c)** water, **(d)** POPC bilayer, and **(e)** 1:1 chloroform/methanol mixture. The stick and sphere models represent the backbone of pTB and the solvent molecules inside the pore, respectively. The black dots indicate hydrogen bonds. The four-coordinated water molecule is highlighted with a pink circle.

The analyses of the configuration and dynamics of solvent molecules inside the pore discussed in the later sections of results and discussions require the proper definition of sites inside the pore. It is hard to define the sites inside the pore in water for certain structures during the first 0.5 μs of the production run, for example, RMSD of ~ 4.0 Å (Fig. 2-4b). Therefore, note that I will be using the last 1.5 μs data of the production run for the system of pTB in water and the whole 2 μs data of the production run for the systems of pTB in the membrane and the mixed solvent for the analyses discussed in the later sections of results and discussions.

Configuration of Molecules inside the Pore

Next, I examined the molecules inside the pore in water, the membrane, and the mixed solvent. In all the simulations of pTB, the mean inner pore diameter of 4.4 Å is broad enough to allow the polar solvent molecules (water/methanol) to permeate through the channel in a single-file fashion. However, the chloroform molecules are not able to enter the channel because of the small pore size. Also, neither Cs^+ nor Cl^- ions can enter the channel.

Figure 2-5a shows the occupancy distribution along the channel axis for solvent molecules inside the pore in the three environments. The distributions were calculated using the COM positions of water and methanol molecules inside the pore. The average number of water molecules inside the pore is 13 in both water and the membrane. The water molecules inside the pore are positioned at an average COM-COM distance of 2.7±0.3 Å, which is close to the COM-COM spacing of 2.82 Å in neat water.[37] In the mixed solvent, the average number of methanol molecules inside the pore is 8. The mean COM-COM spacing of methanol molecules inside the pore is 4.5±0.9 Å, which is much longer than the COM-COM spacing of 3.29 Å in neat methanol.[38]

The probabilities of zero and double occupancies, and the average number of molecules at sites 2-11 and 2-7 for the water and methanol molecules inside the pore, respectively, are given in Tables S2-1 - S2-3 of Supporting Information. The sites for water molecules inside the pore in both water and the membrane are determined based on the distance between adjacent minima in the occupancy distributions given in Fig. 2-5a. The sites near the N-terminal in water and those near the C-terminal in the membrane are broad compared to the rest, because of the flexibility of pTB at these regions in the respective environments. As a result, the average number of water molecules inside the pore in these sites deviate from one, contrast to the other sites with approximately one molecule. The sites for methanol molecules inside the pore are determined by dividing the channel into equal parts having a width of COM-COM spacing, because the methanol molecules can rotate freely inside the channel. The methanol molecules at sites 2-5 largely fluctuate, and are more delocalized compared to those at sites 1 and 6-8, because of the lack of strong HB interactions inside the channel.

The water molecules inside the pore form an extended hydrogen-bonded chain comprising both water-water and water-channel HBs, which is intact most of the time. Most of the water molecules are involved in the following three HBs (three-coordinated water molecules): two hydrogen atoms are donated to a pore-lining carbonyl group and a neighboring water molecule respectively, and one hydrogen atom is accepted from a nearby water molecule. The life time of the three-coordinated water molecule is very long, because the extended hydrogen-bonded chain inside the channel is intact most of the time. Snapshot images showing the HB structures of water molecules inside the pore in water and the membrane are given in Figs. 2-5c and 2-5d. In addition to the three-coordinated water molecules, I occasionally find one metastable four-coordinated water molecule in the channel, which forms four HBs by donating both of its hydrogen atoms

to pore-lining carbonyl groups and accepting two hydrogen atoms from adjacent water molecules. The life time of the four-coordinated water molecule is very short, on the order of sub-picoseconds. Such a four-coordinated water molecule has already been reported in the gA channel.[39] Because of the significant fluctuations of the helix in water, the four-coordinated water molecule can be found anywhere along the channel in water. On the other hand, the four-coordinated water molecule in the membrane is rather localized at the C-terminal half, which is created by the fluctuations of water molecules near the C-terminal. Note that the HB patterns of water molecules inside the pore are crucial in understanding the orientations of water dipole moments inside the pore discussed later.

In contrast to the water molecules inside the pore, each methanol molecule inside the pore has at least two maxima in each site arising from the free rotation about its COM. The methanol molecules inside the pore can rotate freely because of the weak HBs between adjacent methanol molecules: A methanol molecule inside the pore can have only one HB, either with a neighboring methanol molecule or with a pore-lining carbonyl group. Figure 2-5e shows a snapshot image of the HB structure of methanol molecules inside the pore in the mixed solvent. The number of methanol-methanol HBs are very few in the mixed solvent as seen in Fig. 2-5e, and also their life time is very short as the methanol molecules can rotate freely inside the channel.

To understand the directionality of the HBs between molecules inside the pore, I analyzed the orientations of solvent O-H vectors inside the pore about the channel axis. Figure 2-5b shows the distributions of the O-H vector orientations in the three environments. Here, I define the O-H vector orientation as the angle between the O-H vector and the channel axis. As seen in Fig. 2-5b, the peaks at ~30^{o}, ~90^{o}, and ~150^{o} correspond to the orientations toward the C-terminal, the pore-lining carbonyl groups,

and the N-terminal, respectively. The tallest peak at ~90^{o} in all the environments corresponds to the HB interactions with the pore-lining carbonyl groups. Note that one of the O-H vectors of each three-coordinated water molecule turns to ~90^{o} and the dominant HB interactions of methanol molecules inside the pore are with the pore-lining carbonyl oxygens. In both water and the mixed solvent, the distribution is rather symmetric about 90^{o}, indicating that the HBs between molecules do not have a preferable direction. On the other hand, the distribution is asymmetric in the membrane; the peak at ~25^{o} corresponds to the O-H vector of water molecule inside the pore orienting toward the C-terminal.

The inset of Fig. 2-5b shows the distributions of individual dipole moment orientations along the channel axis for molecules inside the pore in the three environments. The dipole moment orientations of water molecules inside the pore show bimodal distributions, corresponding to the orientations toward either the N- or C-terminals in both water and the membrane. In contrast, the orientation of an individual dipole moment of methanol molecule inside the pore is rather uniform in the mixed solvent because of the absence of strong HBs between adjacent molecules. Hence, it is concluded that there is a high propensity for the water dipole moments inside the pore to be oriented in the same direction along the channel axis, which is different from the methanol dipole moments inside the pore. It is also suggested that the ion-permeation mechanism of the pTB channel is strongly affected by the HB patterns of water molecules inside the pore, because these patterns are essential for the stabilization of ions inside the pore. Note that the direction of HB patterns observed in this study may be affected by the potential gradient applied across the bilayer in studying the ion-permeation process through the pTB channel.

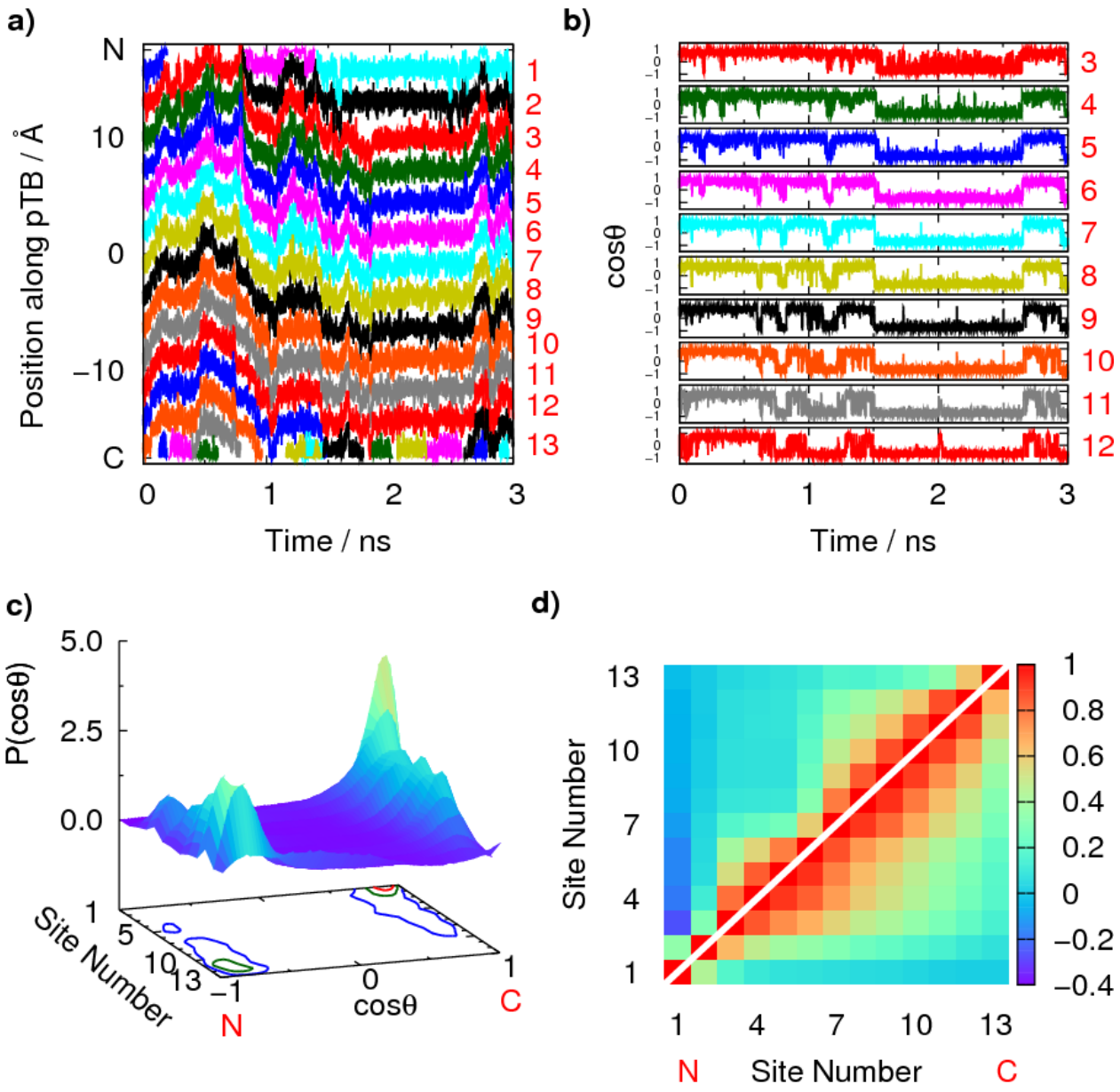

Figure 2-6: Time courses of **(a)** positions and **(b)** dipole moment orientations along the channel axis for water molecules inside the pore in water for 3 ns of simulations. Dipole moment orientations are shown only for those water molecules which remained inside the channel throughout the 3 ns under study. **(c)** The distribution of individual dipole moment orientations along the channel axis as a function of site number in water, calculated using 1.5 μs data. **(d)** Correlation coefficients for the positional fluctuations (upper-left) and the orientational fluctuations (lower-right) of water molecules at individual sites in water, calculated using 1.5 μs data. Cosine values -1 and 1 represent the orientations toward the N- and C-terminals, respectively.

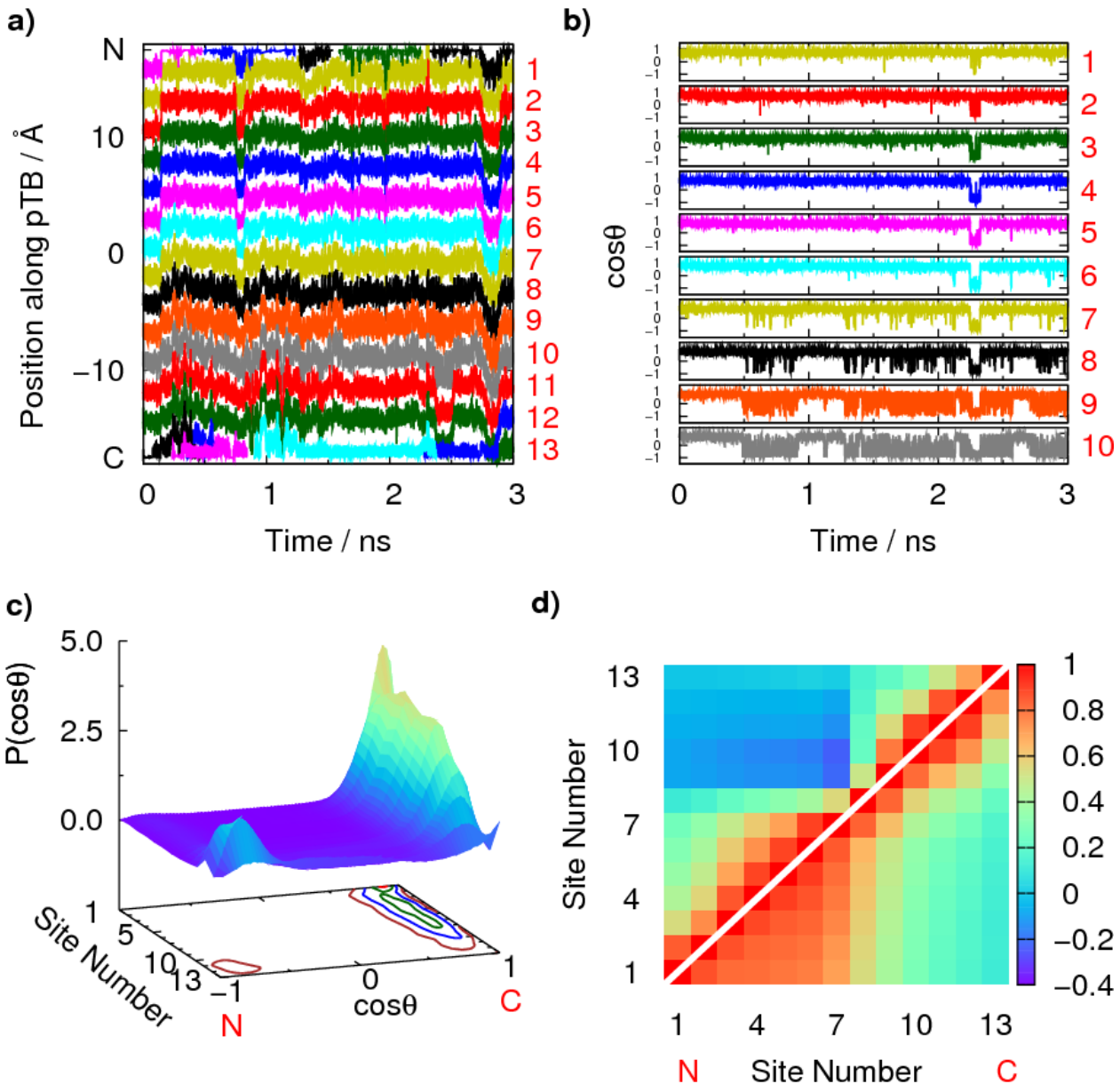

Figure 2-7: Time courses of **(a)** positions and **(b)** dipole moment orientations along the channel axis for water molecules inside the pore in POPC bilayer for 3 ns of simulations. Dipole moment orientations are shown only for those water molecules which remained inside the channel throughout the 3 ns under study. **(c)** The distribution of individual dipole moment orientations along the channel axis as a function of site number in the membrane, calculated using 2 μs data. **(d)** Correlation coefficients for the positional fluctuations (upper-left) and the orientational fluctuations (lower-right) of water molecules at individual sites in the membrane, calculated using 2 μs data. Cosine values -1 and 1 represent the orientations toward the N- and C-terminals, respectively.

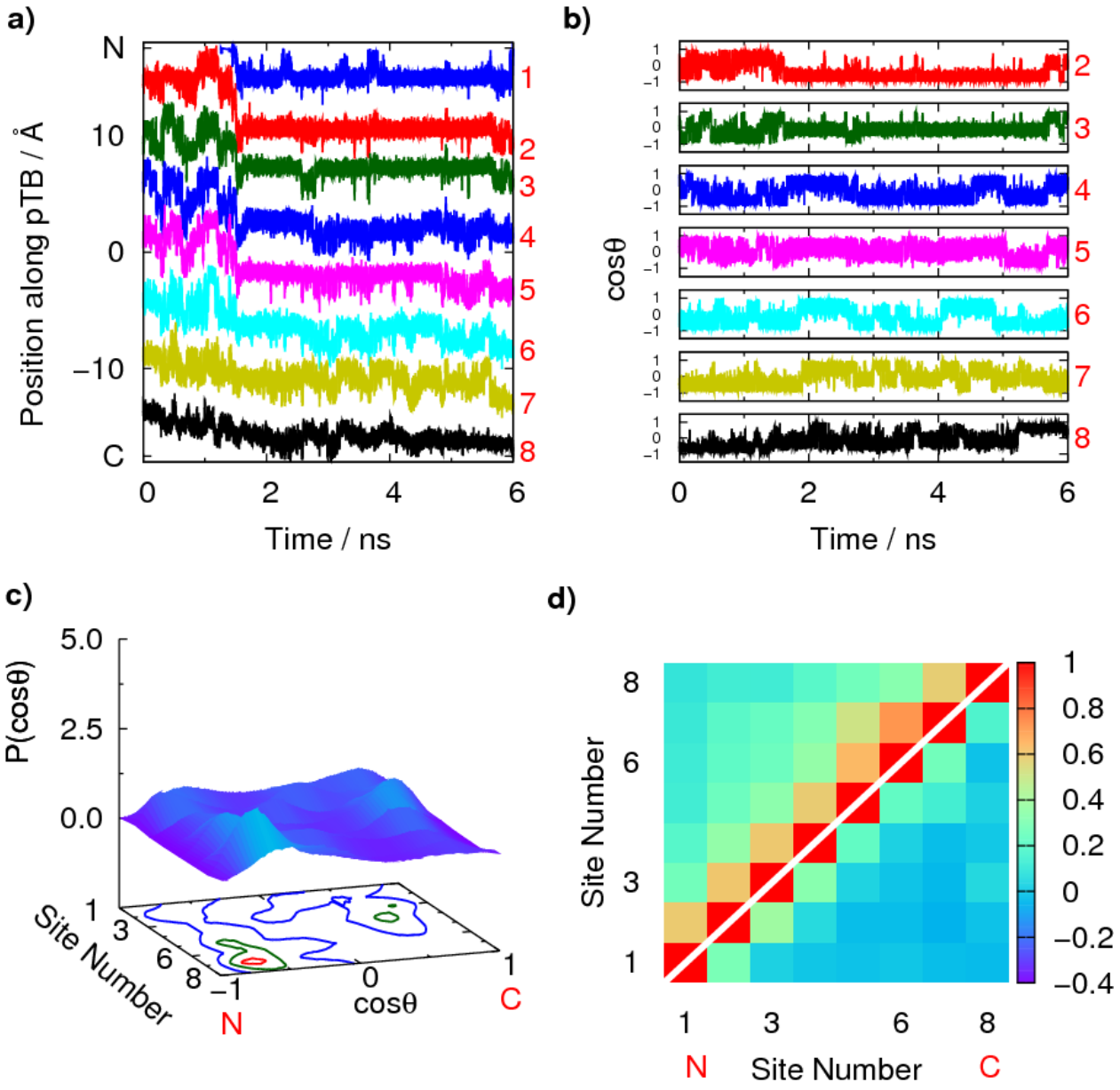

Figure 2-8: Time courses of **(a)** positions and **(b)** dipole moment orientations along the channel axis for methanol molecules inside the pore in 1:1 chloroform/methanol mixture for 6 ns of simulations. Dipole moment orientations are shown only for those methanol molecules which remained inside the channel throughout the 6 ns under study. **(c)** The distribution of individual dipole moment orientations along the channel axis as a function of site number in the mixed solvent, calculated using 2 μs data. **(d)** Correlation coefficients for the positional fluctuations (upper-left) and the orientational fluctuations (lower-right) of methanol molecules at individual sites in the mixed solvent, calculated using 2 μs data. Cosine values -1 and 1 represent the orientations toward the N- and C-terminals, respectively.

Dynamics of Molecules inside the Pore

Next, I analyzed the translational dynamics of molecules inside the pore in the three environments. The characteristic examples of time courses of positions along the channel axis for molecules inside the pore are presented in Figs. 2-6a, 2-7a, and 2-8a. It is found that the translational fluctuations of water molecules inside the pore are well correlated due to the well-packed structure with strong HBs between water molecules in both water and the membrane, whereas those of methanol molecules inside the pore are not well correlated because of the lack of a well-packed structure inside the channel in the mixed solvent. I see intermittent translational motions, i.e., active and resting states, in all the three environments. In the active states, the hopping of the single-file column of molecules inside the pore by one molecule-molecule distance occurs, which is induced by the entry of a new molecule into the channel. The hopping of water molecules, not ions, inside the pore occurs by the so-called “knock-on” mechanism.[40] In the resting states, on the other hand, the molecules inside the pore show thermal fluctuations at individual sites. The duration of resting states in the mixed solvent are longer than those in water and the membrane, due to the less frequent entries of new methanol molecules into the channel.

To examine the spatial correlation of positional fluctuations between sites for molecules inside the pore, the correlation coefficients were calculated with $< \delta r_i \delta r_j > / \sqrt{< \delta r_i^2 >< \delta r_j^2 >}$, where *i* and *j* are site numbers. Here, δr_i denotes the positional fluctuation at site *i*. In water, the correlation matrix of positional fluctuations is rather diagonal. In the membrane, island structures representing strongly correlated sites are seen in the correlation matrix of positional fluctuations (Fig. 2-7d). In the membrane, there are two islands formed between sites 1-7 and between sites 8-13, which are negatively correlated with each other: The positional fluctuations at sites 8-13 are

different from those at sites 1-7 due to the presence of metastable four-coordinated water molecule at the C-terminal half. Similar to the case of water molecules inside the pore in water, the correlation matrix of positional fluctuations for the methanol molecules inside the pore in the mixed solvent does not show any island structures, instead diagonal. The correlation length of the positional fluctuations of methanol molecules inside the pore are short compared to that of water molecules inside the pore, because of the absence of strong HBs between adjacent methanol molecules.

I also examined the orientational fluctuations of individual molecules inside the pore. Figures 2-6b, 2-7b, and 2-8b show the characteristic examples of the time courses of dipole moment orientations along the channel axis for molecules inside the pore. The site-dependent distributions of the individual dipole moment orientations along the channel axis are given in Figs. 2-6c, 2-7c, and 2-8c. As discussed earlier, the dipole moment orientation of a water molecule inside the pore shows a bimodal distribution, corresponding to the orientation either toward the N- or C-terminals. In water, the water dipole moments near the N-terminal (sites 1 and 2) prefer to align toward the C-terminal, whereas those near the C-terminal (sites 11-13) prefer to align toward the N-terminal, i.e., the oxygen atom of the terminal water molecule inside the pore is located near the mouths than the hydrogen atoms to maximize the HB interactions with the outside water molecules. However, the probabilities of preferred alignments near the C-terminal are relatively small compared to those near the N-terminal because of the fluctuations caused by the negative charge on the C-terminal residue. For sites 3-10 in water, the water molecules show frequent changes of the direction of dipole moments along the channel axis.

Figure 2-7c shows that the dipole moment orientations of water molecules inside the pore in the membrane located at sites 1, 2, and 11-13 follow the similar distributions

as in water. Contrary to the case in water, the distributions at sites 3-10 are rather asymmetric in the membrane, resulting from the preferred alignment of the water dipole moments toward the C-terminal. Since the fluctuations of the helix are widely suppressed by the presence of the membrane as seen in Fig. 2-4c, the water dipole moments at sites 3-10 prefer to align in the same direction as that of sites 1 and 2 to maximize the HB interactions. Hence, the distribution of individual dipole moments given in the inset of Fig. 2-5b is asymmetric. It is also noted that the direction of water molecules inside the pore in the membrane is not determined by the head groups of the membrane.

The correlation coefficients $< \delta\boldsymbol{\mu}_i \delta\boldsymbol{\mu}_j > / \sqrt{< \delta\mu_i^2 >< \delta\mu_j^2 >}$ calculated for the orientational fluctuations of water molecules inside the pore at individual sites are given in Figs. 2-6d and 2-7d. I can see island structures in the correlation matrices of orientational fluctuations in both water and the membrane. In water, one large island is formed between sites 2-13, although the correlations between water molecules farther than 6 sites are not larger than 0.5. On the other hand, in the membrane, there are two island structures formed between sites 1-7 and between sites 8-13. As expected from Fig. 2-7b, there exist strong correlations in the island formed between sites 1-7. However, the correlations between the orientational fluctuations of molecules in the island formed between sites 8-13 are weak, because of the change of orientations induced by the metastable four-coordinated water molecule. It is also found that the correlation between the water molecules inside the pore is larger and longer for the orientational fluctuations than the positional fluctuations because of the directionality of HBs.

In contrast, the orientations of methanol dipole moments inside the pore are rather uniform for all sites as seen in Fig. 2-8c. Moreover, there appears to be no strong

correlation between the orientational fluctuations of methanol molecules inside the pore, due to the absence of strong HB interactions between methanol molecules. The orientational fluctuations of even the adjacent methanol molecules inside the pore are therefore weakly anti-correlated with each other. Thus, islands are absent, and only diagonal elements are found for the orientational fluctuations of methanol molecules inside the pore (Fig. 2-8d).

The orientation of the total dipole moment along the channel axis, i.e., the collective orientation, of molecules inside the pore was then analyzed to further clarify the environment dependence of the directionality of HBs. Here, I define the collective orientation as the angle between the total dipole moment vector ($\boldsymbol{M}$) and the channel axis. The total dipole moment is given by $\boldsymbol{M} = \sum_{i=1}^{N} \boldsymbol{\mu}_i$, where $\boldsymbol{\mu}_i$ is the individual dipole moment and N is the number of molecules inside the pore. The number of molecules with the orientation toward the N- or C-terminals can be found by calculating $|M_z|/\mu_z^*$ with the total dipole moment $|M_z|$ and the effective dipole moment μ_z^* along the channel axis. For the systems in water and the membrane, μ_z^* is the dipole moment along the channel axis at cosθ having the peak value of P(cosθ) in the inset of Fig. 2-5b. Therefore, the ratio $|M_z|/\mu_z^*$ in water and the membrane approximately shows the effective number of water molecules inside the pore with the orientation toward the N- or C-terminals. On the other hand, μ_z^* is taken as the dipole moment of methanol in the mixed solvent, because the orientations of methanol dipole moments inside the pore are rather uniform. Note that $\boldsymbol{M}$ is approximately the sum of O-H vectors of methanol molecules inside the pore in the mixed solvent. The characteristic examples of the time courses of the collective orientations and the number of molecules with the orientation toward the N- or C-terminals for the three systems are shown in Fig. 2-9a.

The correlations in the collective orientations of molecules inside the pore can be

quantified by the so-called Kirkwood g-factor, $g_k = < M^2 > / (N < \mu^2 >)$. The g_k larger (less) than 1 indicates the presence of positive (negative) correlation between the individual dipole moments, whereas no correlation exists when g_k is ~1. The g_k values are 3.2, 5.0, and 1.3 in water, the membrane, and the mixed solvent, respectively. The g_k value in bulk water is 4.5.[41] Thus, the results in water, the membrane, and bulk water show the presence of constructive correlation between the dipole moments, though the correlation between the dipole moments in water is slightly reduced due to the fluctuation of the helical structure of pTB. On the other hand, g_k value of ~1 in the mixed solvent is attributed to the absence of correlation between the dipole moments, due to the lack of strong HB interactions between methanol molecules inside the pore.

The distributions of collective orientations in the three systems are shown in Fig. 2-9b. As seen in Fig. 2-9a, the collective orientations of water molecules inside the pore have two values, -1 or 1, because of the strong HBs between water molecules. The orientations toward the N- and C-terminals are equally probable in water, because the metastable four-coordinated water molecule can move freely along the channel, resulting in a rather symmetric distribution in Fig. 2-9b. On the other hand, the total dipole moment prefers to align toward the C-terminal in the membrane. The asymmetric distribution of collective orientations in the membrane can be seen as a result of the asymmetry in the pTB structure, i.e., the hydrophobicity of residues decreases gradually from the N-terminal to the C-terminal. As a result, the two terminals will interact differently with the lipid head group regions. Moreover, I have found that the C-terminal end touches the membrane surface with more water molecules near the channel mouth, and the N-terminal end resides just below the membrane surface with relatively small number of water molecules near the channel mouth (Fig. 2-3b). The presence of more water molecules near the C-terminal end causes large fluctuations of water molecules near this end, and leads to the formation of the metastable four-coordinated water

molecule at the C-terminal half. The presence of metastable four-coordinated water molecule at the C-terminal half, in turn, causes the change of water dipole moment orientations at this half. On the other hand, the fluctuations of water molecules near the N-terminal end is very small because of the presence of relatively small number of water molecules near the N-terminal end. Therefore, the water dipole moments at the N-terminal half have a preferred alignment toward the C-terminal which is intact most of the time, resulting in an asymmetric distribution of collective orientations in the membrane. In contrast to the distributions of collective orientations in water and the membrane, that in the mixed solvent is rather uniform, because the methanol molecules inside the pore can rotate freely about their COMs.

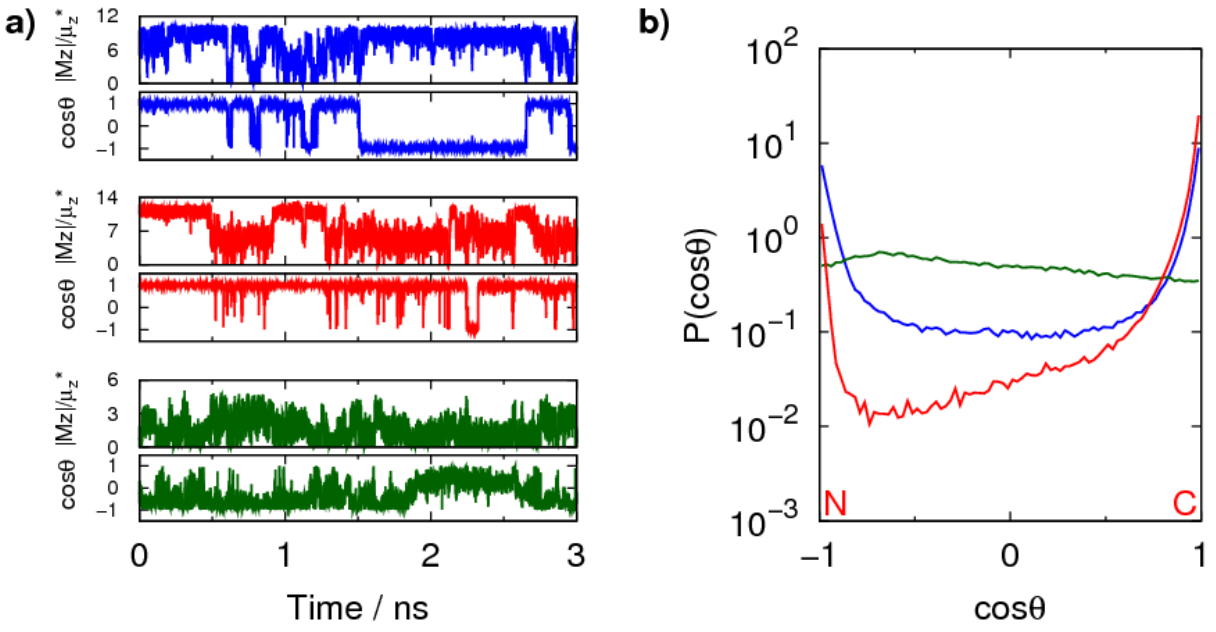

Figure 2-9: Collective orientations of molecules inside the pore in water (blue), POPC bilayer (red), and 1:1 chloroform/methanol mixture (dark-green). **(a)** Time courses of total dipole moment orientations along the channel axis and the number of molecules with the orientation toward the N- or C-terminals for 3 ns of simulations. **(b)** Distributions of total dipole moment orientations along the channel axis calculated from 1.5 μs data in water, and 2 μs data in both the membrane and the mixed solvent. Cosine values -1 and 1 represent the orientations toward the N- and C-terminals, respectively.

I finally analyzed the residence time of a molecule at a particular site. Here, the residence time is defined as the time the molecule remains within a given site before making any transitions to the nearby sites. The residence time distributions (RTDs) averaged over all sites for the three environments are given in Fig. 2-10a, calculated using the data saved every 10 ps. The site numbers employed in the RTD calculations are 2-11 and 2-7 for water and methanol molecules inside the pore, respectively. The mean residence times in water, the membrane, and the mixed solvent are 126, 136, and 248 ps, respectively. The RTD in water is almost identical with that in the membrane. The residence time in the mixed solvent is, however, found to be longer than those in water and the membrane. The longer residence times in the mixed solvent are attributed to the absence of a well-packed structure inside the channel.

I also examined the RTDs of individual sites in the three environments. It is found that the site-dependence of the RTD is very weak in water and the mixed solvent. In water, the translational dynamics at individual sites are rather homogeneous, because the metastable four-coordinated water molecule can move freely along the channel. In contrast, I find a remarkable site-dependence of the RTDs in the membrane as seen in Fig. 2-10b: the RTDs at sites 2-8 have a high probability of longer residence times, whereas those at sites 9-11 have a low probability of longer residence times, compared to the RTD averaged over all the sites. The shorter residence times at sites 9-11 in the membrane can be related to the preferred residence of the metastable four-coordinated water molecule at the C-terminal half. There is a higher chance of double occupancy at site 8 in the membrane as given in Table S2-2 of Supporting Information, because the site 8 is at the center of fast and slow dynamic regions, and has longer residence times. The present study thus shows the inhomogeneous translational motions of water

molecules inside the pore in the membrane by the appearance of a metastable four-coordinated water molecule at the C-terminal half.

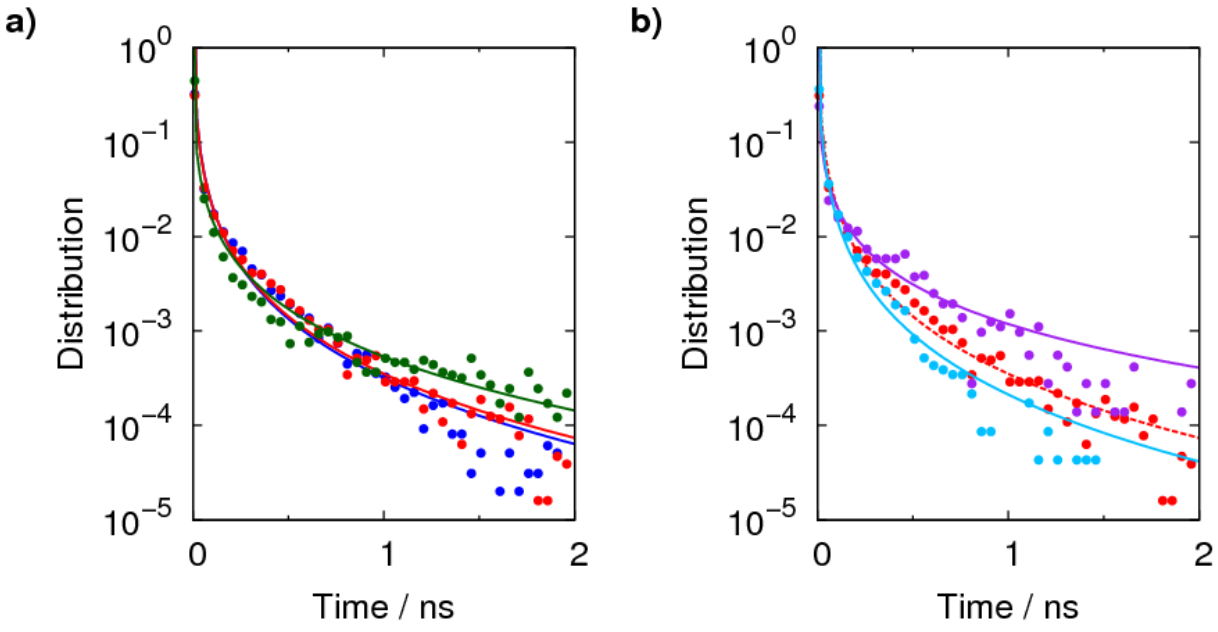

Figure 2-10: Residence time distributions for molecules inside the pore. Distributions are calculated using 1.5 μs data in water, and 2 μs data in both the membrane and the mixed solvent. Distributions are fitted using stretched-exponential functions. **(a)** Distribution averaged over all the sites in water (blue), POPC bilayer (red), and 1:1 chloroform/methanol mixture (dark-green). **(b)** Distribution at sites 2 (purple) and 11 (sky-blue) in the membrane. The distribution averaged over all the sites in the membrane (red) is also shown for comparison.

Conclusions

The structure and fluctuations of the pTB channel, and the dynamics of molecules inside the pore were explored in water, POPC bilayer, and 1:1 chloroform/methanol mixture using all-atom MD simulations. The average structure of pTB calculated in the mixed solvent with the current parameters for the non-standard groups is in excellent agreement with the NMR-derived structure in the mixed solvent. My simulations show that the $\beta^{6.3}$-helix of pTB is indeed stable in all the three environments.

Since the parameters used for the non-standard groups in pTB were validated, I

examined the structure and dynamics of HBs by the molecules inside the pore in detail. I found that the water molecules inside the pore are well-stabilized through extended HBs among water molecules and the pore-lining carbonyl oxygens, whereas such an HB network is absent in the mixed solvent. The present study showed the correlated motions of water molecules inside the pore, involving the tendency of all water molecules to align in the same direction and to hop by one water-water distance at a time. However, the orientational motions of water molecules inside the pore are found to be less directional in water than in the membrane. The highly correlated motions of water molecules inside the pore in the membrane are essential for the permeation of ions through the pTB channel. On the other hand, the motions of methanol molecules inside the pore are not correlated because of the absence of strong HBs between adjacent methanol molecules.

The membrane insertion of pTB is the cause of its potent cytotoxicity.[5] It is, therefore, important to comprehend how a toxin like pTB gets insert into the membrane. Moreover, I can consider the membrane insertion of pTB as a process of pore formation in the membrane, which is a fundamental process of interest for many biophysical processes.[42,43] The ion permeation mechanism of the pTB channel is another interesting problem, which is not well understood both experimentally and theoretically. The precise molecular mechanisms of membrane insertion of pTB, and ion permeation through the pTB channel will be investigated in my future studies.

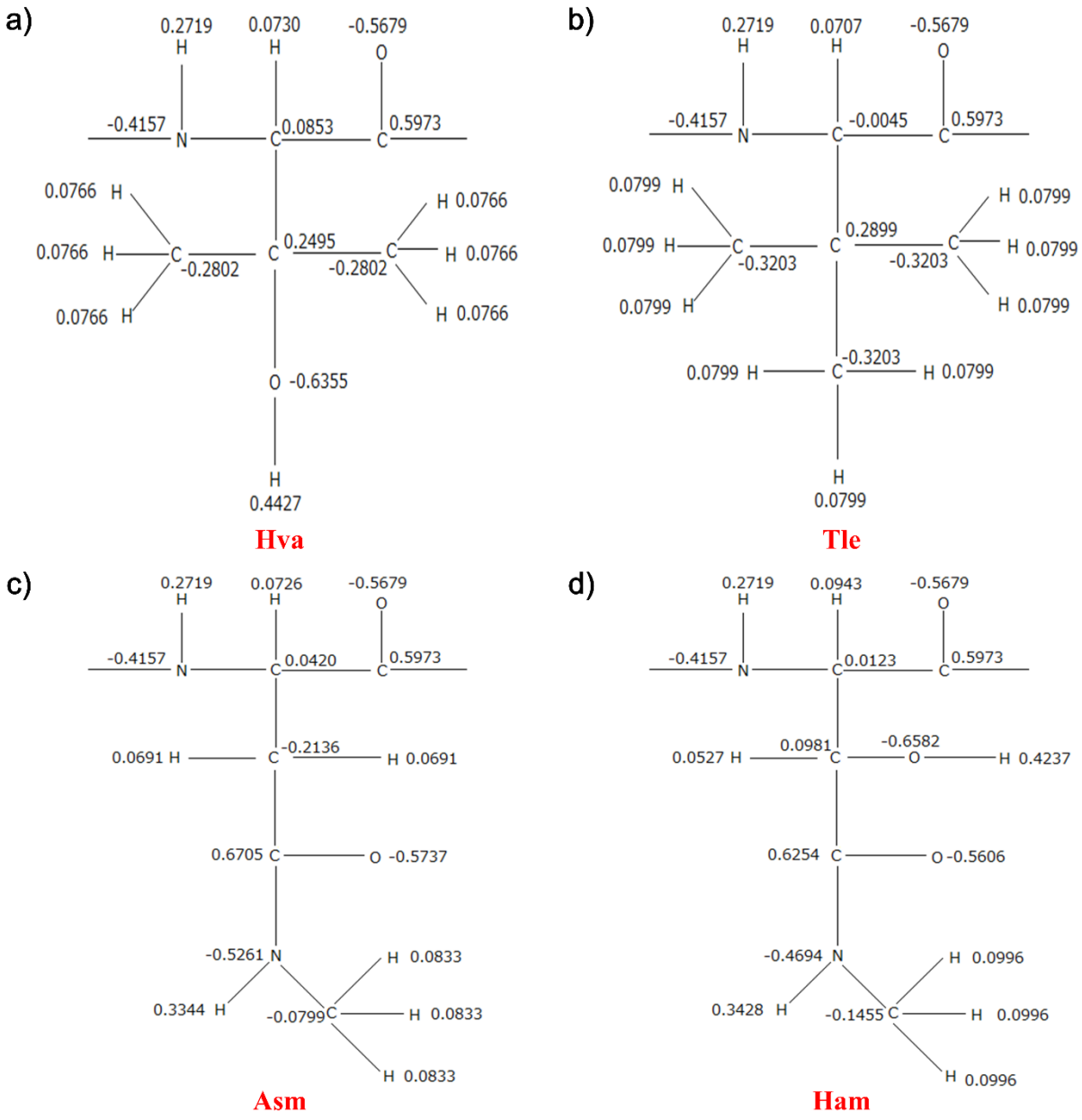

Figure S2-1: Point charges for the non-standard groups in pTB. **(a)** β-hydroxyvaline (Hva). **(b)** *tert*-leucine (Tle). **(c)** γ-N-methylasparagine (Asm). **(d)** γ-N-methyl-*threo*-β-hydroxyasparagine (Ham).

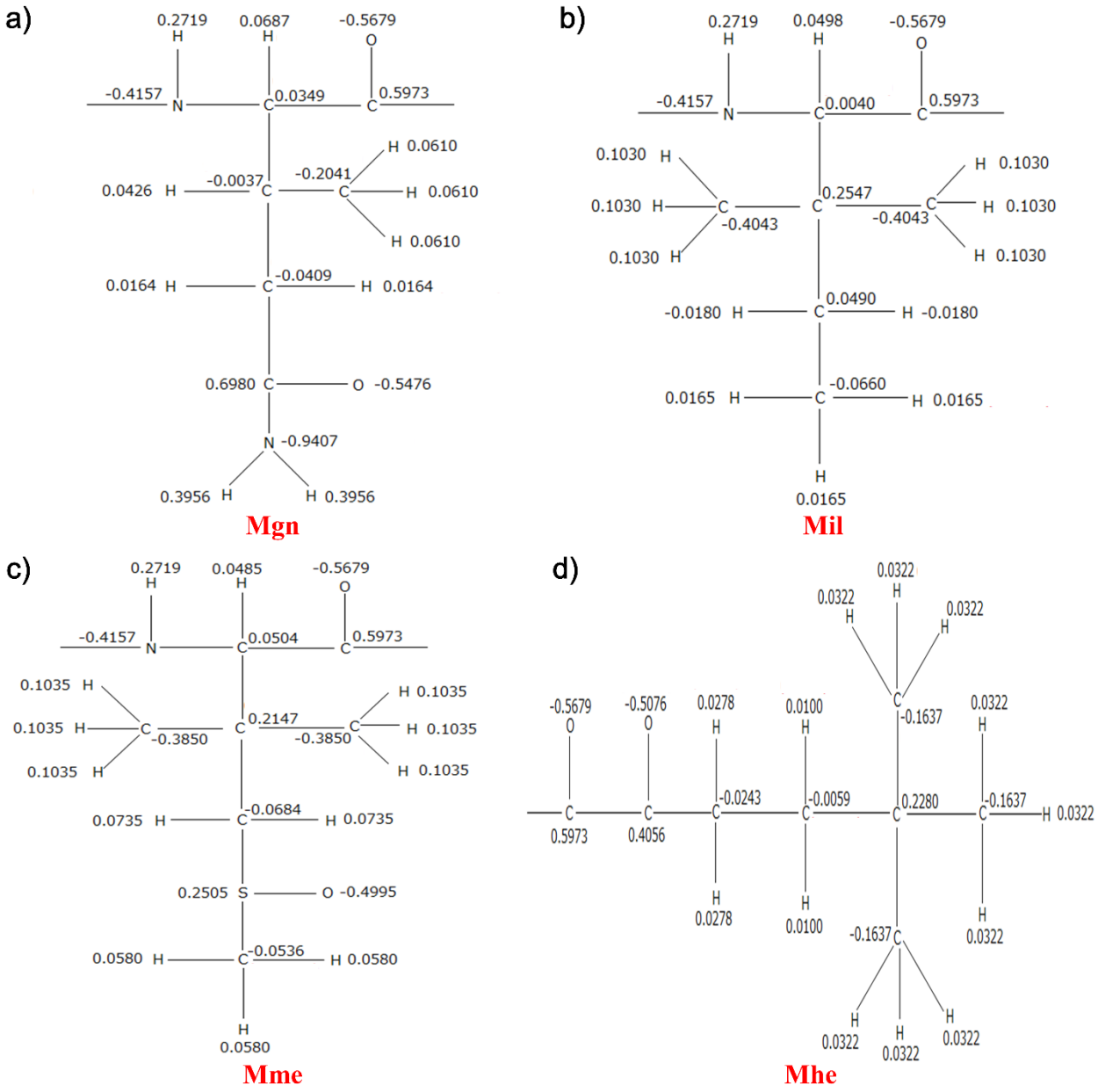

Figure S2-2: Point charges for the non-standard groups in pTB. **(a)** β-methylglutamine (Mgn). **(b)** β-methylisoleucine (Mil). **(c)** β,β-dimethylmethionine sulphoxide (Mme). **(d)** 5,5-dimethyl-2-oxo-hexanoyl (Mhe).

Table S2-1: Probabilities of zero and double occupancies, and average number of molecules at sites 2-11 for water molecules inside the pore in water, calculated from 1.5 μs data.

Site Number	2	3	4	5	6	7	8	9	10	11
P(n=0)	0.0662	0.0657	0.0760	0.0402	0.0134	0.0154	0.0068	0.0261	0.0160	0.0728
P(n=2)	0.2804	0.0204	0.0255	0.0205	0.0769	0.0430	0.0320	0.0068	0.0179	0.0080
<n>	1.2146	0.9547	0.9495	0.9803	1.0635	1.0277	1.0251	0.9807	1.0019	0.9351

Table S2-2: Probabilities of zero and double occupancies, and average number of molecules at sites 2-11 for water molecules inside the pore in POPC bilayer, calculated from 2 μs data.

Site Number	2	3	4	5	6	7	8	9	10	11
P(n=0)	0.0022	0.0069	0.0032	0.0033	0.0076	0.0249	0.0008	0.0133	0.0386	0.0659
P(n=2)	0.0228	0.0125	0.0057	0.0050	0.0084	0.0099	0.2572	0.0497	0.0155	0.0086
<n>	1.0206	1.0056	1.0025	1.0017	1.0008	0.9850	1.2564	1.0364	0.9769	0.9427

Table S2-3: Probabilities of zero and double occupancies, and average number of molecules at sites 2-7 for methanol molecules inside the pore in 1:1 chloroform/methanol mixture, calculated from 2 μs data.

Site Number	2	3	4	5	6	7
P(n=0)	0.0854	0.0569	0.0505	0.0709	0.0409	0.0824
P(n=2)	0.0275	0.0640	0.0520	0.0508	0.0712	0.0167
<n>	0.9421	1.0071	1.0015	0.9800	1.0303	0.9342

References

(1) Hamada, T.; Sugawara, T.; Matsunaga, S.; Fusetani, N. Polytheonamides, Unprecedented Highly Cytotoxic Polypeptides, from the Marine Sponge Theonella Swinhoei. *Tetrahedron Lett.* **1994**, *35* (5), 719–720.

(2) Oiki, S.; Muramatsu, I.; Matsunaga, S.; Fusetani, N. A Channel-Forming Peptide Toxin: Polytheonamide from Marine Sponge (Theonella Swinhoei). *Nihon Yakurigaku Zasshi.* **1997**, *110* (Suppl. 1), 195P–198P.

(3) Hamada, T.; Matsunaga, S.; Yano, G.; Fusetani, N. Polytheonamides A and B, Highly Cytotoxic, Linear Polypeptides with Unprecedented Structural Features, from the Marine Sponge, Theonella Swinhoei. *J. Am. Chem. Soc.* **2005**, *127* (1), 110–118.

(4) Hamada, T.; Matsunaga, S.; Fujiwara, M.; Fujita, K.; Hirota, H.; Schmucki, R.; Güntert, P.; Fusetani, N. Solution Structure of Polytheonamide B, a Highly Cytotoxic Nonribosomal Polypeptide from Marine Sponge. *J. Am. Chem. Soc.* **2010**, *132* (37), 12941–12945.

(5) Iwamoto, M.; Shimizu, H.; Muramatsu, I.; Oiki, S. A Cytotoxic Peptide from a Marine Sponge Exhibits Ion Channel Activity through Vectorial-Insertion into the Membrane. *FEBS Lett.* **2010**, *584* (18), 3995–3999.

(6) Inoue, M.; Shinohara, N.; Tanabe, S.; Takahashi, T.; Okura, K.; Itoh, H.; Mizoguchi, Y.; Iida, M.; Lee, N.; Matsuoka, S. Total Synthesis of the Large Non-Ribosomal Peptide Polytheonamide B. *Nat Chem* **2010**, *2* (4), 280–285.

(7) Ducho, C. Convergence Leads to Success: Total Synthesis of the Complex Nonribosomal Peptide Polytheonamide B. *Angew. Chemie Int. Ed.* **2010**, *49* (30), 5034–5036.

(8) Mori, T.; Kokubo, H.; Oiki, S.; Okamoto, Y. Dynamic Structure of the Polytheonamide B Channel Studied by Normal Mode Analysis. *Mol. Simul.* **2011**, *37* (12), 975–985.

(9) Freeman, M. F.; Gurgui, C.; Helf, M. J.; Morinaka, B. I.; Uria, A. R.; Oldham, N. J.; Sahl, H.-G.; Matsunaga, S.; Piel, J. Metagenome Mining Reveals Polytheonamides as Posttranslationally Modified Ribosomal Peptides. *Science (80-.).* **2012**.

(10) Shinohara, N.; Itoh, H.; Matsuoka, S.; Inoue, M. Selective Modification of the N-Terminal Structure of Polytheonamide B Significantly Changes Its Cytotoxicity and Activity as an Ion Channel. *ChemMedChem* **2012**, *7* (10), 1770–1773.

(11) Itoh, H.; Inoue, M. Chemical Construction and Structural Permutation of Potent Cytotoxin Polytheonamide B: Discovery of Artificial Peptides with Distinct Functions. *Acc. Chem. Res.* **2013**, *46* (7), 1567–1578.

(12) Iwamoto, M.; Matsunaga, S.; Oiki, S. Paradoxical One-Ion Pore Behavior of the Long β-Helical Peptide of Marine Cytotoxic Polytheonamide B. *Sci. Rep.* **2014**, *4*, 3636.
(13) Iwamoto, M.; Oiki, S. Contact Bubble Bilayers with Flush Drainage. *Sci. Rep.* **2015**, *5*, 9110.
(14) Matsuki, Y.; Iwamoto, M.; Mita, K.; Shigemi, K.; Matsunaga, S.; Oiki, S. Rectified Proton Grotthuss Conduction Across a Long Water-Wire in the Test Nanotube of the Polytheonamide B Channel. *J. Am. Chem. Soc.* **2016**, *138* (12), 4168–4177.
(15) Freeman, M. F.; Helf, M. J.; Bhushan, A.; Morinaka, B. I.; Piel, J. Seven Enzymes Create Extraordinary Molecular Complexity in an Uncultivated Bacterium. *Nat. Chem.* **2016**, *9* (4), 387–395.
(16) Renevey, A.; Riniker, S. The Importance of N-Methylations for the Stability of the $\beta^{6.3}$ -Helical Conformation of Polytheonamide B. *Eur. Biophys. J.* **2017**, *46* (4), 363–374.
(17) Iwamoto, M.; Oiki, S. Membrane Perfusion of Hydrophobic Substances Around Channels Embedded in the Contact Bubble Bilayer. *Sci. Rep.* **2017**, *7* (1), 6857.
(18) Andersen, O. S.; Koeppe, R. E.; Roux, B. Gramicidin Channels. *IEEE Trans. Nanobioscience* **2005**, *4* (1), 10–20.
(19) Maier, J. A.; Martinez, C.; Kasavajhala, K.; Wickstrom, L.; Hauser, K. E.; Simmerling, C. ff14SB: Improving the Accuracy of Protein Side Chain and Backbone Parameters from ff99SB. *J. Chem. Theory Comput.* **2015**, *11* (8), 3696–3713.
(20) Jorgensen, W. L.; Chandrasekhar, J.; Madura, J. D.; Impey, R. W.; Klein, M. L. Comparison of Simple Potential Functions for Simulating Liquid Water. *J. Chem. Phys.* **1983**, *79* (2), 926–935.
(21) Dickson, C. J.; Madej, B. D.; Skjevik, Å. A.; Betz, R. M.; Teigen, K.; Gould, I. R.; Walker, R. C. Lipid14: The Amber Lipid Force Field. *J. Chem. Theory Comput.* **2014**, *10* (2), 865–879.
(22) Cieplak, P.; Caldwell, J.; Kollman, P. Molecular Mechanical Models for Organic and Biological Systems Going beyond the Atom Centered Two Body Additive Approximation: Aqueous Solution Free Energies of Methanol and N-Methyl Acetamide, Nucleic Acid Base, and Amide Hydrogen Bonding and Chloroform/. *J. Comput. Chem.* **2001**, *22* (10), 1048–1057.
(23) Caldwell, J. W.; Kollman, P. A. Structure and Properties of Neat Liquids Using Nonadditive Molecular Dynamics: Water, Methanol, and N-Methylacetamide. *J. Phys. Chem.* **1995**, *99* (16), 6208–6219.
(24) Joung, I. S.; Cheatham, T. E. Determination of Alkali and Halide Monovalent Ion Parameters for Use in Explicitly Solvated Biomolecular Simulations. *J.*

Phys. Chem. B **2008**, *112* (30), 9020–9041.

(25) Cornell, W. D.; Cieplak, P.; Bayly, C. I.; Gould, I. R.; Merz, K. M.; Ferguson, D. M.; Spellmeyer, D. C.; Fox, T.; Caldwell, J. W.; Kollman, P. A. A Second Generation Force Field for the Simulation of Proteins, Nucleic Acids, and Organic Molecules. *J. Am. Chem. Soc.* **1995**, *117* (19), 5179–5197.

(26) Bayly, C. I.; Cieplak, P.; Cornell, W.; Kollman, P. A. A Well-Behaved Electrostatic Potential Based Method Using Charge Restraints for Deriving Atomic Charges: The RESP Model. *J. Phys. Chem.* **1993**, *97* (40), 10269–10280.

(27) Wang, J.; Wolf, R. M.; Caldwell, J. W.; Kollman, P. A.; Case, D. A. Development and Testing of a General Amber Force Field. *J. Comput. Chem.* **2004**, *25* (9), 1157–1174.

(28) Case, D. A.; Babin, V.; Berryman, J. T.; Betz, R. M.; Cai, Q.; Cerutti, D. S.; Cheatham, T. E.; Darden, T. A.; Duke, R. E.; Gohlke, H.; Goetz, A. W.; Gusarov, S.; Homeyer, N.; Janowski, P.; Kaus, J.; Kolossváry, I.; Kovalenko, A.; Lee, T. S.; LeGrand, S.; Luchko, T.; Luo, R.; Madej, B.; Merz, K. M.; Paesani, F.; Roe, D. R.; Roitberg, A.; Sagui, C.; Salomon-Ferrer, R.; Seabra, G.; Simmerling, C. L.; Smith, W.; Swails, J.; Walker, R. C.; Wang, J.; Wolf, R. M.; Wu, X.; Kollman, P. A. AMBER 14, University of California, San Francisco. 2014.

(29) Ryckaert, J.-P.; Ciccotti, G.; Berendsen, H. J. C. Numerical Integration of the Cartesian Equations of Motion of a System with Constraints: Molecular Dynamics of N-Alkanes. *J. Comput. Phys.* **1977**, *23* (3), 327–341.

(30) Darden, T.; York, D.; Pedersen, L. Particle Mesh Ewald: An $N \cdot \log(N)$ Method for Ewald Sums in Large Systems. *J. Chem. Phys.* **1993**, *98* (12), 10089–10092.

(31) Jo, S.; Lim, J. B.; Klauda, J. B.; Im, W. CHARMM-GUI Membrane Builder for Mixed Bilayers and Its Application to Yeast Membranes. *Biophys. J.* **2009**, *97* (1), 50–58.

(32) Pastor, R. W.; Brooks, B. R.; Szabo, A. An Analysis of the Accuracy of Langevin and Molecular Dynamics Algorithms. *Mol. Phys.* **1988**, *65* (6), 1409–1419.

(33) Berendsen, H. J. C.; Postma, J. P. M.; van Gunsteren, W. F.; DiNola, A.; Haak, J. R. Molecular Dynamics with Coupling to an External Bath. *J. Chem. Phys.* **1984**, *81* (8), 3684–3690.

(34) Kučerka, N.; Nieh, M.-P.; Katsaras, J. Fluid Phase Lipid Areas and Bilayer Thicknesses of Commonly Used Phosphatidylcholines as a Function of Temperature. *Biochim. Biophys. Acta - Biomembr.* **2011**, *1808* (11), 2761–2771.

(35) Roe, D. R.; Cheatham, T. E. PTRAJ and CPPTRAJ: Software for Processing and Analysis of Molecular Dynamics Trajectory Data. *J. Chem. Theory Comput.* **2013**, *9* (7), 3084–3095.

(36) Humphrey, W.; Dalke, A.; Schulten, K. VMD - Visual Molecular Dynamics. *J.*

Mol. Graph. **1996**, *14*, 33–38.
(37) Franks, F. *Water*; RSC Paperbacks; The Royal Society of Chemistry, 2000.
(38) Lu, L.; Voth, G. A. The Multiscale Coarse-Graining Method. VII. Free Energy Decomposition of Coarse-Grained Effective Potentials. *J. Chem. Phys.* **2011**, *134* (22), 224107.
(39) Pomès, R.; Roux, B. Molecular Mechanism of H+ Conduction in the Single-File Water Chain of the Gramicidin Channel. *Biophys. J.* **2002**, *82* (5), 2304–2316.
(40) Hodgkin, A. L.; Keynes, R. D. The Potassium Permeability of a Giant Nerve Fibre. *J. Physiol.* **1955**, *128* (1), 61–88.
(41) Guillot, B. A Molecular Dynamics Study of the Far Infrared Spectrum of Liquid Water. *J. Chem. Phys.* **1991**, *95* (3), 1543–1551.
(42) Lee, M.-T.; Chen, F.-Y.; Huang, H. W. Energetics of Pore Formation Induced by Membrane Active Peptides. *Biochemistry* **2004**, *43* (12), 3590–3599.
(43) Lee, M.-T.; Hung, W.-C.; Chen, F.-Y.; Huang, H. W. Mechanism and Kinetics of Pore Formation in Membranes by Water-Soluble Amphipathic Peptides. *Proc. Natl. Acad. Sci. U. S. A.* **2008**, *105* (13), 5087–5092.

Chapter 3

Spontaneous Insertion of a β-helical Peptide into Membrane: A Theoretical Study on Polytheonamide B

Introduction

The process of insertion of peptides into the cell membrane is crucial for toxin actions,[1] viral infections,[2] and antimicrobial defense.[3] The understanding of the mechanism of membrane insertion is essential for the development of novel therapeutic drugs against bacterial and viral infections. Moreover, the process of pore formation in the membrane is also related to the insertion of peptides into the membrane.[4] There are two types of membrane insertion processes: “direct” and “indirect” insertion processes. The indirect insertion occurs with the assistance of translocon channels which themselves are α-helical membrane proteins that already reside in the membrane, and is the most common process for the natively synthesized membrane proteins in all organisms.[5–9] On the other hand, the peptide spontaneously inserts into the membrane in the direct insertion, a process predominantly taken by pore-forming toxins and antimicrobial peptides.[10–16]

In both direct and indirect insertions, the system needs to overcome a finite energy barrier thermodynamically to accomplish the membrane insertion. In the translocon-assisted membrane insertion, the protein environment of the translocon lowers the energy barrier for insertion, thereby making the membrane insertion of de

novo synthesized transmembrane proteins smoother and faster.[17] On the other hand, the energy barriers for the spontaneous membrane insertion of peptides are overcome by complex competition and cooperation between hydrophilic and hydrophobic interactions involving peptides and membrane.[18]

The polytheonamide B (pTB) is one such pore-forming cytotoxin obtained from marine sponge *Theonella swinhoei*.[16,19–27] The potent cytotoxicity of pTB is related to its channel-forming activity across the target cell membrane by spontaneously inserting into the membrane.[16,20] The prefolding of the 48-residue long right-handed $\beta^{6.3}$-helix occurs in the aqueous environment before insertion.[27,28] The alternate D- and L-amino acids throughout the sequence allow the peptide to take a right-handed $\beta^{6.3}$-helical conformation, similar to the gramicidin A (gA) channel (see Fig. 3-1a).[29] There are eight types of unnatural amino acids in pTB: β-hydroxyvaline (Hva), *tert*-leucine (Tle), γ-N-methylasparagine (Asm), γ-N-methyl-*threo*-β-hydroxyasparagine (Ham), β-methylglutamine (Mgn), β-methylisoleucine (Mil), β,β-dimethylmethionine sulphoxide (Mme), and *allo*-threonine (aTh). Also, the hydrophobicity of residues decreases gradually from the N-terminal to the C-terminal. The long and short side chain – side chain hydrogen bond strands outside the pore reinforce the stability of the long $\beta^{6.3}$-helix of pTB (see Fig. 3-1a).[28] Structural features suggest that the pTB inserts into the membrane led by the hydrophobic N-terminal and stays in the membrane stably.[16,25,26,30,31] The highly hydrophobic N-terminal blocking group, 5,5-dimethyl-2-oxo-hexanoyl (Mhe, see Fig. 3-1a), is thought to anchor the spontaneous “vectorial insertion” of pTB into the target cell membrane.[16] The 40 Å long pTB can readily span the membrane as a monomeric channel and allows the permeation of monovalent cations.[16,20,25,26] As a simple model for the transmembrane peptide, the $\beta^{6.3}$-helix of pTB is an ideal peptide to explore the underlying mechanism of the spontaneous membrane insertion of prefolded single transmembrane peptides. However, the precise molecular

mechanism of the spontaneous membrane insertion of pTB is not well understood both experimentally and theoretically.

Molecular dynamics (MD) simulation is a powerful tool that provides atomistic details for understanding the membrane insertion process of various peptides, and its utility is strongly dependent on the accessible time scales and the accuracy of the force fields used. In fact, the observation of either the direct or indirect membrane insertion of peptides is rather time-consuming using the conventional MD simulations, due to the presence of a finite energy barrier for the insertion. Consequently, most of the theoretical and computational studies on the membrane insertion of peptides are centered around the free energies of peptide insertion.[17,32–39]

The recent developments in the computational efficiency and the underlying force fields of MD simulations have made it possible to study the spontaneous membrane insertion of various peptides, such as antimicrobial peptides,[40–43] thermostable peptides,[44–47] pH low-insertion peptide (pHLIP),[48] first transmembrane α-helix of CXCR4,[18] cell-penetrating HIV-1 TAT peptide,[49] and synthetic WALP and TMX peptides.[50–53] The simulations using the α-helix of CXCR4 suggest that both the membrane insertion and the preferred orientation of the transmembrane peptides during the insertion are determined by competition and cooperation between hydrophobic and electrostatic interactions, although successful spontaneous insertion was not observed.[18] The vectorial insertion, i.e., the one-directional membrane insertion led by the preferred terminal, found in the case of pTB[16] is also found for the α-helix of CXCR4.[18] Unlike pTB, the C-terminal was found to anchor the membrane insertion of the α-helix from CXCR4. The study using the thermostable peptides at a temperature of 80 ^{o}C reveals that the general pathways taken by membrane-inserting peptides consist of three phases: surface adsorption, interfacial folding, and folded transmembrane

insertion.[44,46] Despite these studies, the mechanism of the spontaneous membrane insertion of prefolded peptides at room temperature is currently not fully understood.

In this study, the membrane insertion of pTB is examined using all-atom MD simulations. The free energy profiles of insertion are analyzed using the replica-exchange umbrella sampling (REUS) simulations. I find a free energy barrier of 4.3 kcal/mol located at the membrane surface for pTB to get inserted into the membrane from bulk water, which is arising from the entropic bottleneck. In between the global free energy maximum and minimum, there is a “shoulder” region corresponding to the trapping of pTB in the upper leaflet. The Voronoi tessellation analysis of the area per lipid (APL) suggests that the insertion of pTB causes only the local lateral compression of the membrane. On the other hand, the membrane thickness remained almost constant during the insertion because of small “hydrophobic mismatch”.[54–56]

To clarify the membrane uptake mechanism, the membrane insertion pathways of pTB are investigated in detail using unconstrained MD simulations. My simulations confirm the experimental observation of the spontaneous membrane insertion of pTB led by the hydrophobic N-terminal.[16] The overall insertion process takes place in three successive phases: “landing,” “penetration,” and “equilibration” phases. The individual insertion process can occur in two possible pathways, namely “trapped” and “untrapped” insertions, according to whether or not pTB is trapped in the upper leaflet during the penetration phase.

My results can provide useful insights to clarify the membrane insertion mechanism of other spontaneously inserting prefolded single transmembrane peptides. The present study highlights the vectorial insertion of a transmembrane peptide, and reinforces the importance of membrane anchoring for the vectorial insertion. I found that the membrane uptake of pTB from bulk water is anchored by Mhe. Being the first

theoretical and computational study of the spontaneous membrane insertion of a β-helical peptide, my results can provide useful insights to synthesize novel peptides and therapeutic drugs that can spontaneously insert into target cell membranes in a vectorial fashion.[57]

This chapter is organized as follows. Section 2 describes the methods of system preparation and the simulation details. In Section 3, I present my simulation results and discuss the results using various analyses. Finally, conclusions are given in Section 4.

Methods

In the present study, I examined the insertion of pTB into the POPC bilayer using all-atom MD simulations. The POPC bilayer was chosen for this study because of its similarity with the DPhPC bilayer used in the experiments of pTB,[16,25] and the length of the pTB channel roughly matches the thickness of a POPC bilayer. The force field parameters for the natural amino acids were taken from the AMBER ff14SB force field.[58] The parameters for the non-standard groups in pTB (Hva, Tle, Asm, Ham, Mgn, Mil, Mme, and Mhe) were taken from my previous work.[27] The TIP3P model was used for water molecules.[59] The POPC bilayer parameters were taken from the Lipid14 force field.[60] The ions were modeled using the monovalent ion parameters developed by Joung and Cheatham.[61]

All MD simulations were performed at three-dimensional periodic boundary conditions using AMBER18 package.[62] The bonds involving hydrogen were constrained using the SHAKE algorithm,[63] enabling a time step of 2 fs. Long-range electrostatic interactions were taken into account using the particle mesh Ewald approach[64] with a real-space cutoff of 12 Å. For all simulations, the Langevin thermostat[65] with a collision frequency of $\gamma = 1.0$ ps^{-1} was used to maintain the temperature at the relevant

experimental temperature of 303 K[60], and the isotropic Berendsen barostat[66] with a pressure relaxation time of τ = 1.0 ps was used to maintain the pressure at 1 atm.

For the preparation of POPC bilayer, a fully hydrated POPC bilayer having 100 lipid molecules in each layer was first constructed using the CHARMM-GUI Membrane Builder.[67] The generated membrane patch had 58 Å thick hydration layer on each side, and 0.15 M CsCl salt concentration added to bulk water. The CsCl salt was chosen because of the high ionic conductivity of Cs^+ ions in the planar lipid bilayer experiments of the pTB channel.[16,25] The generated POPC bilayer was then undergone an energy minimization for 10000 steps, of which the first 5000 steps used the steepest descent method and the remaining steps used the conjugate gradient method.[68] This was followed by heating from 0 K to 303 K under the NVT conditions for 100 ps, and finally an equilibration run at the NPT conditions for 50 ns. The equilibration of the system was confirmed by comparing the average APL and membrane thickness, with those reported in the previous experimental and simulation studies.[60,69] The average APL and membrane thickness obtained are 65.6 $Å^2$ and 38.6 Å, respectively.

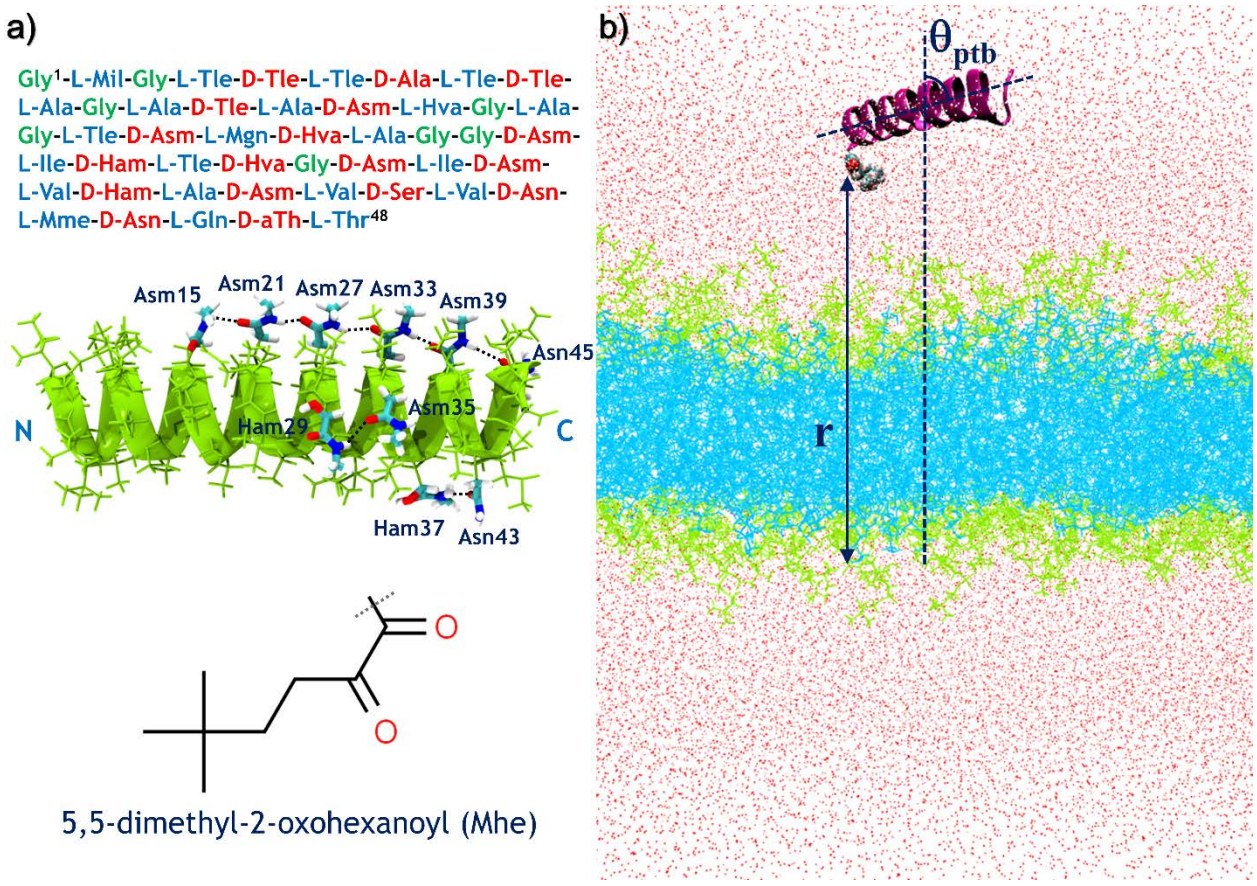

Figure 3-1: (a) Primary and tertiary structures of pTB, and structure of N-terminal blocking group (Mhe). In the primary structure, residues are numbered from the N-terminal to the C-terminal. The amino acid residues shown in green, red, and blue are Glycine, D-type, and L-type residues, respectively. The right-handed $\beta^{6.3}$-helical backbone of pTB is shown as a green ribbon and side chains as thin green stick models. The thick stick models represent the side chains of residues involved in the side chain – side chain hydrogen bonds, which are labeled with their residue numbers. The black dots indicate hydrogen bonds. **(b)** A snapshot image of the system under study. In the snapshot image, pTB is represented as a magenta ribbon model with Mhe shown as a van der Waals sphere model, and the membrane as thin stick models with lipid head and tail groups in light-green and cyan colors, respectively. Water and ions are represented as points. The definitions of the reaction coordinate, r, and the tilt angle, θ_{ptb}, are also indicated in the snapshot image.

Subsequently, the equilibrium structure of pTB in water, taken from my previous work,[27] was inserted into bulk water. The water molecules that overlap with the inserted pTB molecule were then removed. One Cs^+ ion was added for neutralizing the net charge of the deprotonated C-terminal of pTB. The final system was comprised of one pTB

molecule, 200 POPC lipid molecules, 23126 water molecules, 64 Cs^+ ions and 63 Cl^- ions, resulting in a total of 97032 atoms. The combined system was then undergone an energy minimization for 10000 steps, of which the first 5000 steps used the steepest descent method and the remaining steps used the conjugate gradient method.[68] This was followed by an equilibration run at the NPT conditions for 50 ns. The simulation cell dimensions of the fully equilibrated system were ~ 81 × ~ 81 × ~ 146 $Å^3$, and this system was used to initialize the subsequent free energy calculations. A snapshot image of the system under study is given in Fig. 3-1b. In all the simulations in this study, almost no deformation from the rectangular shape of the equilibrium system was observed.

The one-dimensional potential of mean force (1D-PMF) profile of insertion was calculated from the REUS simulations.[70,71] The reaction coordinate (RC) is taken to be the distance along the membrane normal, between the C atom at the center of the *tert*-butyl part of the N-terminal blocking group (Mhe) and the center of mass (COM) of P atoms of the headgroups in the lower leaflet (see Fig. 3-1b). The bilayer side having the shortest distance from pTB is termed as the upper leaflet and the other side is termed as the lower leaflet hereafter. The membrane normal is defined as the vector pointing from the COM of upper leaflet to that of lower leaflet. The RC was varied from 80 to 0 Å with a window spacing of 1.0 Å, resulting in a total of 81 windows, using harmonic biasing potential with a force constant of 1.0 kcal mol^{-1} $Å^{-2}$. The replicas for individual windows were well equilibrated for 1 μs at the NPT conditions prior to the REUS simulations. At each window, the system was undergone 3 μs REUS run at the NPT conditions with trajectory data recorded every 10 ps. For better statistics, the RC was recorded every 100 fs from the REUS simulations, resulting in a total of 30 million RC values for each window. The one-dimensional weighted histogram analysis method (1D-WHAM)[72–74] was used to construct the 1D-PMF profile from the RC data collected from the REUS simulations.

The two-dimensional potential of mean force (2D-PMF) profile was then constructed from the 1D REUS simulation data by introducing θ_{ptb} as the second RC, using the two-dimensional weighted histogram analysis method (2D-WHAM)[73,74] where the biasing function for the second RC is presumed to have a zero force constant. The θ_{ptb} is the angle pTB makes with the bilayer normal (see Fig. 3-1b). In this chapter, pTB is defined as the vector pointing from the COM of the first six Cα atoms at the C-terminal to that at the N-terminal.

For observing the spontaneous insertion of pTB into the POPC bilayer, I carried out 30 long unbiased MD simulations (each for > 1.5 μs) under the NPT conditions from different starting points farther than the transition state (TS) at the 1D-PMF profile. The initial configurations for the unbiased simulations were taken from the REUS simulations. The unbiased trajectory data was recorded every 10 ps.

The standard CPPTRAJ analysis routines[75] and in-house written scripts were applied for the analyses. The Voronoi tessellation of membrane surface was constructed using the APL@Voro program.[76] All snapshot images and movies from the simulations were generated using the Visual Molecular Dynamics (VMD) package.[77]

Results and Discussions

I first discuss the results on the free energy profile of insertion, followed by the results on the spontaneous insertion of pTB, and finally the footprints of membrane insertion.

Free Energy Profile of Membrane Insertion

Figure 3-2a shows the 1D-PMF profile of insertion. The pTB moved from 80 to 0 Å along the RC, r. The free energy change for r varying from 80 to 60 Å is 0.8 kcal/mol (1.3 k_BT, where k_B and T are the Boltzmann constant and the temperature of the

system, respectively), since the interaction between pTB and the membrane is very small. This corresponds to the “free-floating region” ($r \geq$ 60 Å) of the 2D-PMF profile shown in Fig. 3-2b, where the free energy contours along the tilt angle are broad, indicating the large orientational freedom of pTB due to the absence of strong interactions with the membrane.

The free energy shows a gradual increase from 60 Å as pTB moves toward the membrane surface (~ 42.5 Å), which corresponds to the “membrane sensing region” ($42.5 \leq r <$ 60 Å) of the 2D-PMF profile. In the membrane sensing region, larger tilt angles are restricted as pTB starts to feel the presence of membrane, thereby making the width of the free energy contours along the tilt angle bit smaller than those in the free-floating region. The distribution of θ_{ptb} is narrowed in this region due to the asymmetry in the pTB structure, i.e., the hydrophobicity of residues decreases gradually from the N-terminal to the C-terminal.[16] As a result, the N-terminal tends to be closer to the membrane surface than the C-terminal does. It is found that the highly hydrophobic N-terminal blocking group (Mhe) anchors the membrane approach of pTB from bulk water.

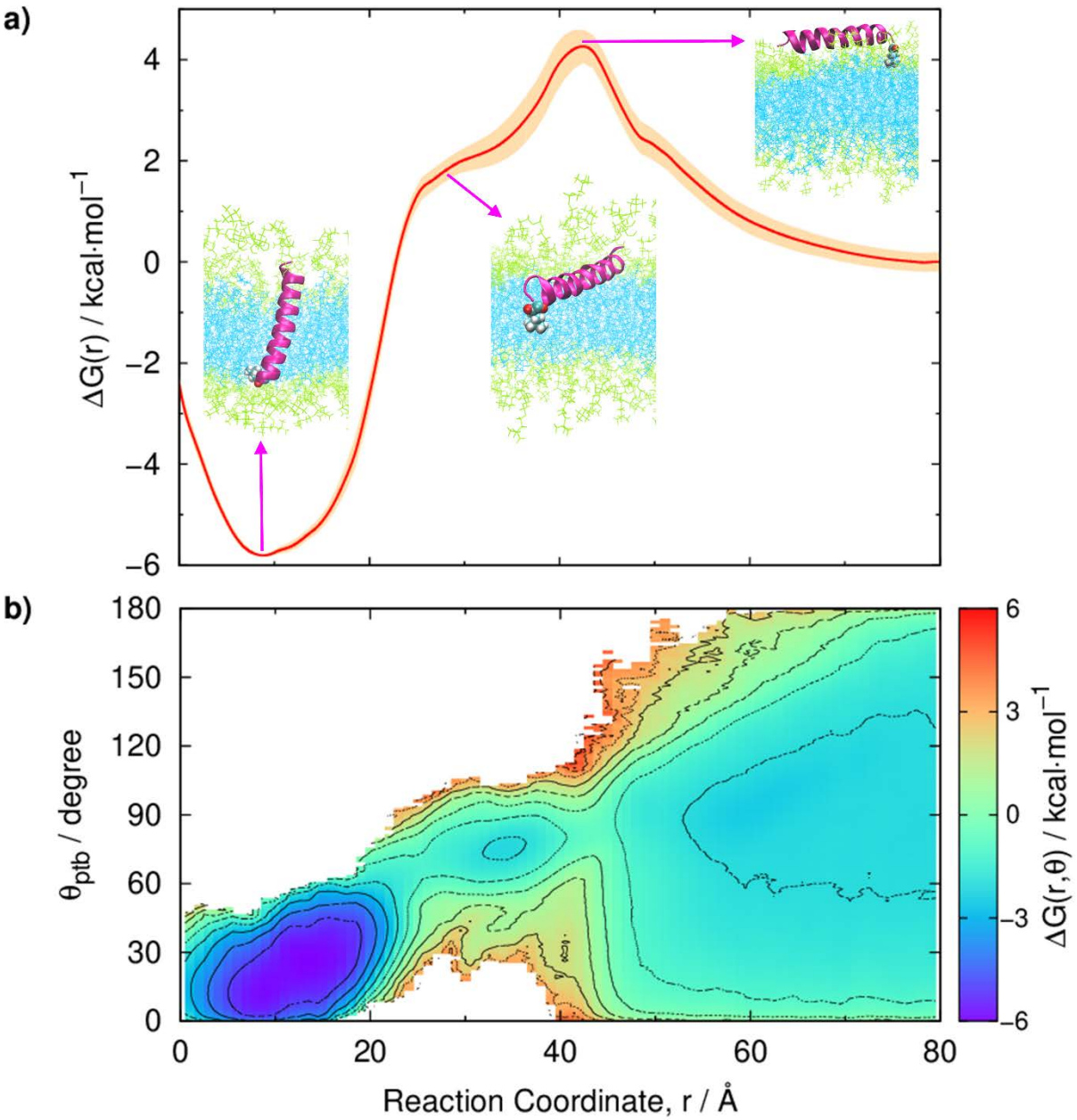

Figure 3-2: (a) One-dimensional free energy profile as a function of the reaction coordinate, r. Standard deviations of the free energies are represented by shaded regions. Snapshot images corresponding to the transition state, shoulder region, and global minimum are shown in the inset. In the snapshot images, pTB is represented as a magenta ribbon model with Mhe shown as a van der Waals sphere model, and the membrane as thin stick models with lipid head and tail groups in light-green and cyan colors, respectively. For clarity, water and ions are not shown in the snapshot images. **(b)** Two-dimensional free energy surface as a function of the reaction coordinate, r, and the tilt angle, θ_{ptb}.

This membrane anchoring by Mhe is driven by the unfavorable interactions of the

N-terminal in bulk water, and is important for the “vectorial insertion” of pTB found in the experimental studies.[16] The vectorial insertion of peptide, in which the peptide is inserted into the membrane in only one direction, is a result of the feature called the “axial amphipathicity”.[16] Therefore, it is important for the peptide to have membrane anchoring by the preferred terminal in order for the vectorial insertion into the membrane, as found in a previous study for the first transmembrane α-helix of CXCR4 where the C-terminal is found to anchor the membrane insertion process.[18]

Then, the free energy barrier of 4.3 kcal/mol (~ 7.2 k_BT) is found at 42.5 Å, which is the TS. The pTB lay on the surface of the upper leaflet with an average tilt angle of 78.6 ± 11.8^0 at the TS (see inset of Fig. 3-2a). The region below the TS corresponds to the “membrane penetrating region” ($r < 42.5$ Å) of the 2D-PMF profile. In the membrane penetrating region, the contours become narrow as pTB penetrates into the membrane, which is due to the restricted orientational freedom of pTB arising from the strong interactions with the membrane. After crossing the barrier, the free energy gradually decreases. It is noted that the membrane penetration of pTB occurs specifically with the N-terminal and is driven by the hydrophobic interactions between the N-terminal and the tailgroups of the membrane, consistent with the experimental results.[16]

The pTB then reaches a “shoulder region” of 10 Å length from 35 to 25 Å, which corresponds to the trapping of pTB in the upper leaflet (see inset of Fig. 3-2a). Due to the asymmetry in the structure of pTB, the shoulder region is stabilized by the hydrophilic interactions between the C-terminal and the headgroups, and the hydrophobic interactions between the N-terminal and the tailgroups of the upper leaflet. After the shoulder region, the free energy decreases steeply and reaches the global minimum at 8.5 Å with a stabilization of -5.8 kcal/mol relative to the solution phase.

At the global free energy minimum, the pTB was fully inserted with the N-terminal residing just below the headgroup region of the lower leaflet and the C-terminal touching the membrane surface of the upper leaflet (see inset of Fig. 3-2a), as found in my previous work.[27] The average θ_{ptb} value at the global free energy minimum is 16.9 ± 8.1^0. The $\beta^{6.3}$-helix of pTB remained intact throughout the insertion process. Finally, the free energy starts to increase again as pTB penetrates further from the global minimum toward the headgroup region of the lower leaflet.

The free energy barrier obtained with POPC bilayer for the membrane insertion of the α-helical antimicrobial peptide, melittin, is 13.2 kcal/mol,[38] while that for a closed and pristine 5 nm long single-walled carbon nanotube is 4.9 kcal/mol.[78] The high free energy barrier associated with the membrane insertion of melittin can be seen as a result of the large hydration of melittin arising from the presence of multiple charged residues. On the other hand, the small hydration in the case of pristine carbon nanotube results in the small free energy barrier for its membrane uptake.

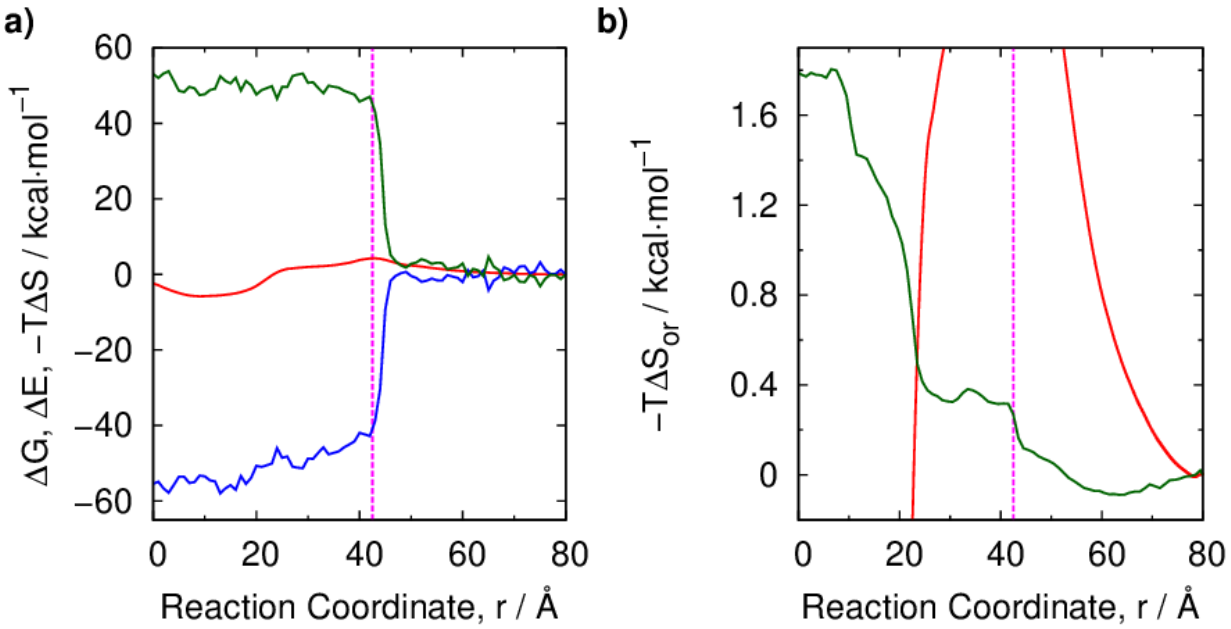

Figure 3-3: (a) Free energy (ΔG, red), energy (ΔE, blue), and entropy (-TΔS, dark-green) as a function of the reaction coordinate, r. **(b)** Orientational entropy ($-T\Delta S_{or}$, dark-green) as a function of the reaction coordinate, r. Free energy (ΔG, red) is also shown for reference. In both the figures, r = 42.5 Å (transition state) is marked with pink dashed lines.

The average energy (ΔE) and entropy (-TΔS) along r are given in Fig. 3-3a. The average energies are calculated from the REUS simulation data using the equation $< E(r)e^{\beta U(r)} > / < e^{\beta U(r)} >$, where E(r) and U(r) are respectively the total potential energy of the system and the umbrella potential at r, $\beta = 1/k_BT$, and $< \cdots >$ denotes ensemble average. The total potential energy is defined as $E = E_{ptb} + E_{popc} + E_{water} + E_{ion} + E_{ptb\text{-}popc} + E_{ptb\text{-}water} + E_{ptb\text{-}ion} + E_{popc\text{-}water} + E_{popc\text{-}ion} + E_{water\text{-}ion}$, where the subscripts specify the various components of the total potential energy, and these components along r are given in Figs. S3-1 - S3-3 of Supporting Information. The standard deviations of the total potential energy of the system are large because of the slow convergence of the total energy and are therefore not shown in Fig. 3-3a. The entropy (-TΔS) is evaluated as -TΔS = ΔG-ΔE-PΔV. It is found that the pressure-volume term (PΔV) is negligibly small. As seen in Fig. 3-3a, both the energy and entropic terms are rather flat when $r \geq 46$ Å and then they gradually change as pTB moves further

toward the TS resulting in a barrier (no barrier) in the entropy (energy) profile at 42.5 Å. Therefore, it is now clear that the free energy barrier at 42.5 Å arises from the "entropic bottleneck" rather than enthalpic term. After crossing the TS, ΔE slightly decreases, whereas $-T\Delta S$ is rather flat compared with ΔE.

As seen in Fig. 3-2b, the restriction of the orientation of pTB with respect to the membrane normal, i.e., the restriction of θ_{ptb}, as r varies from 80 to 0 Å leads to a decrease in orientational entropy. The orientational entropy along r can be evaluated by $S_{or}(r) = -k_B \int_0^{\pi} \rho(r, \theta_{ptb}) \ln \rho(r, \theta_{ptb}) \sin \theta_{ptb} \, d\theta_{ptb}$, where $\rho(r, \theta_{ptb})$ is the 2D probability density of r and θ_{ptb}.[79] This orientational entropic contribution, $-TS_{or}(r)$, to the observed free energy barrier is ~ 0.4 kcal/mol as seen in Fig. 3-3b, which is only 9 % of the total barrier. Note that the entropic contribution estimated here is not the overall entropic contribution to the free energy barrier, instead the contribution just from the tilt angle of pTB.

The analyses of various energy components given in Figs. S3-1 - S3-3 of Supporting Information led to the following conclusions. The energy change associated with the insertion is defined as the change in energy when pTB moves from 80 to 9 Å along r ($E_{9\,Å}$-$E_{80\,Å}$). The N- and C-terminals of pTB show fluctuations in bulk water because the surrounding water molecules can easily break the backbone hydrogen bonds near the terminals by forming stable hydrogen bonds with the backbone atoms, as found in my previous work.[27] These fluctuations are largely suppressed in the process of going from bulk water to the hydrophobic core of the membrane, resulting in an energy stabilization of -46.9 kcal/mol in E_{ptb}. On the other hand, E_{popc} has an energy destabilization of 47.1 kcal/mol in the process, arising from the destabilization of the bilayer structure caused by the insertion of pTB. There is a large destabilization of 423.3 kcal/mol in $E_{ptb\text{-}water}$ as pTB loses its solvation structure in bulk water for

getting inserted into the membrane. The loss of solvation of pTB by water molecules in bulk water, in turn, causes an increase in water-water interactions, resulting in a stabilization of -300.6 kcal/mol in E_{water}. When pTB gets fully inserted into the membrane, $E_{ptb\text{-}popc}$ has a stabilization of -360.3 kcal/mol due to the maximization of pTB-membrane interactions. Also, there is a gradual decrease in the membrane-water interactions as pTB becomes closer to the membrane surface, due to the displacement of many water molecules which are closer to the membrane surface by pTB, resulting in a destabilization of 193 kcal/mol in $E_{popc\text{-}water}$. No such significant changes are seen in the remaining energy components $E_{ptb\text{-}ion}$, $E_{popc\text{-}ion}$, $E_{water\text{-}ion}$, and E_{ion} as pTB moves from bulk water to the hydrophobic core of the membrane. It is now clear that the global free energy minimum is mainly obtained by the stabilization of both water-water and pTB-membrane interactions. Therefore, it is found that the stabilization of $E_{ptb} + E_{ptb\text{-}popc} + E_{water}$ in going from bulk water to the hydrophobic core of the membrane is partially canceled with the destabilization of $E_{popc} + E_{ptb\text{-}water} + E_{popc\text{-}water}$, giving rise to a stabilization of -53.3 kcal/mol in the total potential energy E.

Also, the free energy increase as pTB further inserts from the global minimum is due to the decrease of both pTB-water and membrane-water interactions. As pTB moves to the lower leaflet, the number of water molecules in contact with the pTB and the membrane surfaces decreases because the terminals of pTB displace the water molecules near the respective surfaces, resulting in the increase of $E_{ptb\text{-}water}$ and $E_{popc\text{-}water}$ components.

Spontaneous Membrane Insertion

To reveal the molecular processes in the membrane insertion of pTB, I carried out 30 long unbiased MD simulations from $r > 42.5$ Å as described in the Methods section. A

total of 8 successful spontaneous membrane insertion trajectories are obtained out of the 30 tries. The analyses of the 8 successful insertion trajectories clearly show two distinct insertion pathways, which are termed as “trapped” and “untrapped” insertions hereafter (Figs. 3-4 and 3-5). In the trapped insertion, the pTB gets trapped in the upper leaflet for several hundred nanoseconds (see Fig. 3-5). The period for which the pTB got trapped in the upper leaflet is called the “quiescent period” during the trapped insertion. The quiescent period is in the range of ~ 250-450 ns for the 3 trapped trajectories I obtained. On the other hand, there occurs no such trapping in the untrapped insertion (see Fig. 3-4). The remaining 6 insertion trajectories are shown in Figs. S3-4 - S3-9 of Supporting Information. Out of the 8 independent insertion trajectories, untrapped insertion occurs for 5 trajectories and trapped insertion occurs for the remaining 3 trajectories. Therefore, it is conceivable that untrapped insertion is the dominant insertion pathway for pTB.

Irrespective of the type of insertion pathway, the insertion process can be described by three successive phases: “landing,” “penetration,” and “equilibration” phases. As time passes, the pTB which is initially placed in bulk water lands on the surface of the upper leaflet, thereby reaching the TS of the 1D-PMF profile. This is the “landing” phase, in which the pTB takes a lower tilt angle prior to the membrane “penetration” phase, and its duration is in the range of 0.1-1.2 μs depending on the trajectory. The penetration phase is followed by an “equilibration” phase, in which the pTB embedded membrane system equilibrates. It is noted that the pTB could penetrate only till the head/tail interface of the lower leaflet ($r \approx 8.5$ Å, the global free energy minimum) in all the insertion trajectories, as expected from the 1D-PMF profile.

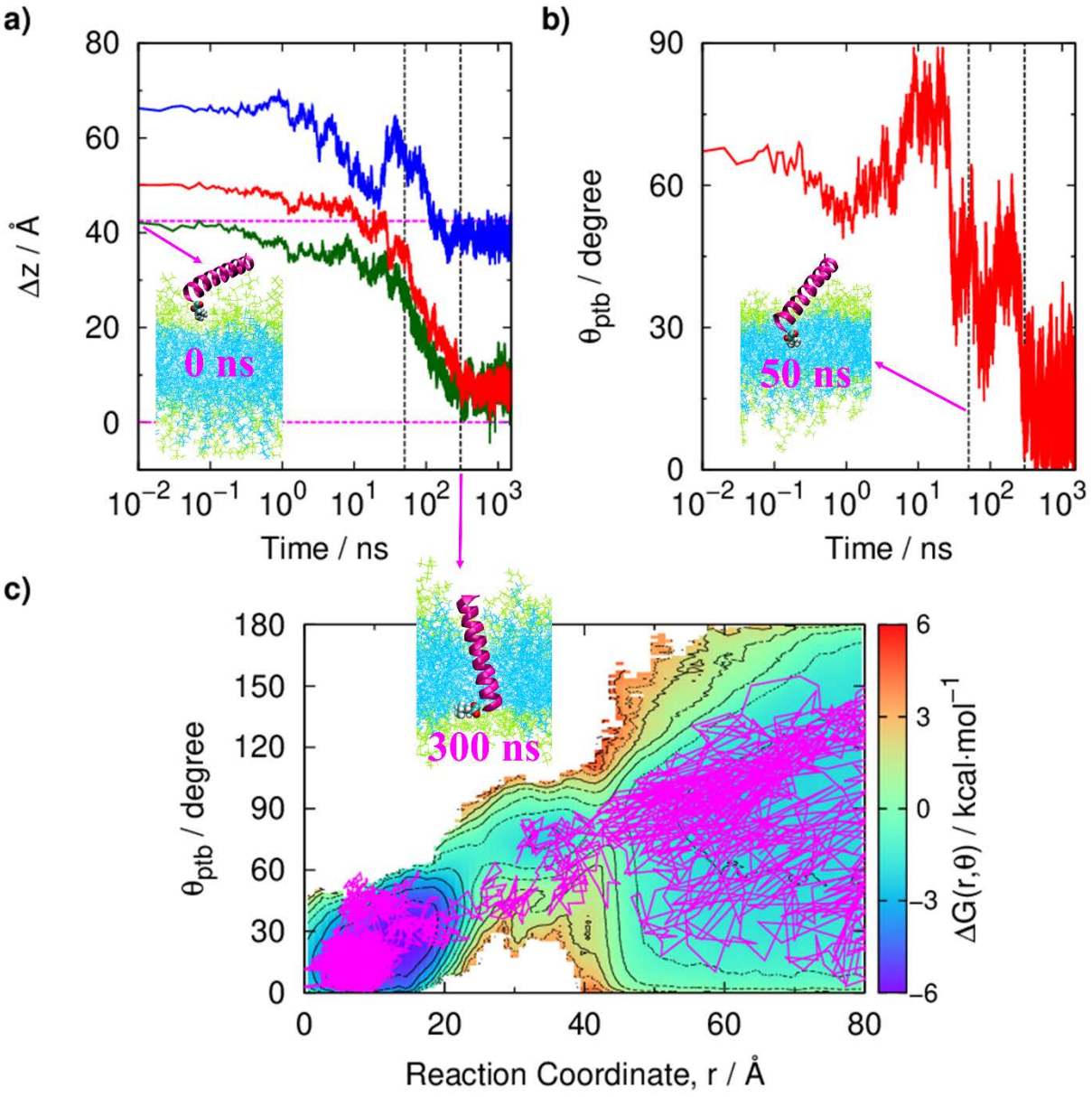

Figure 3-4: Characteristic example of an untrapped insertion of pTB. Time courses of **(a)** reaction coordinate, r (dark-green), z-distances of the N- (red) and C- (blue) terminals from the membrane surface of the lower leaflet, and **(b)** tilt angle, θ_{ptb}, during insertion. **(c)** Mapping of (r, θ_{ptb}) values on the 2D-PMF profile using pink lines. In the top left figure, the transition state (Δz = 42.5 Å) and the membrane surface of the lower leaflet (Δz = 0 Å) are marked by pink dashed lines. Characteristic times 50 and 300 ns are marked with black dashed lines. Snapshot images at 0, 50, and 300 ns are also shown. In the snapshot images, pTB is represented as a magenta ribbon model with Mhe shown as a van der Waals sphere model, and the membrane as thin stick models with lipid head and tail groups in light-green and cyan colors, respectively. For clarity, water and ions are not shown in the snapshot images.

The insertion pathways are analyzed below in terms of the time courses of the RC (r), the z-distances of the N- and C-terminals from the membrane surface of the lower leaflet, and the tilt angle (θ_{ptb}). The N- and C-terminals are defined as the COMs of the first six Cα atoms at the respective terminals. In addition, the (r, θ_{ptb}) values are projected onto the 2D-PMF profile. All the insertion trajectories shown in this chapter are time-shifted trajectories such that r is at the TS (42.5 Å) at t = 0 ns. That means that the time evolution of pTB before finally crossing the TS (for $r > 42.5$ Å), corresponding to the "landing" phase, is not shown in the time-course profiles. On the other hand, the (r, θ_{ptb}) mapping on the 2D-PMF surface is done using the whole insertion trajectory ($0 \leq r \leq 80$ Å).

First, I examine the untrapped membrane insertion of pTB. A characteristic example of an untrapped insertion is shown in Fig. 3-4. The "penetration" phase starts as pTB begins to penetrate the membrane led by the highly hydrophobic N-terminal blocking group (Mhe), with a tilt angle of 67^0 taken during the "landing phase". The penetration phase is a two-step process: the first and second steps represent the initial penetration of ~ 15 Å long region of the upper leaflet (~ $25 < r < 42.5$ Å) and the subsequent penetration of ~ 20 Å long region until pTB reaches the head/tail interface of the lower leaflet (~ $8.5 < r <$ ~ 25 Å), respectively. As seen in Fig. 3-4a, the pTB completes the first step of the penetration phase in ~ 50 ns when r reaches ~ 25 Å with a tilt angle of ~ 45^0. As pTB penetrates deeper into the hydrophobic core of the membrane, the tilt angle gradually changes to lower values and reaches a value of ~ 15^0 when pTB is fully inserted into the membrane at t = 300 ns. The duration of the second step of the penetration phase is ~ 250 ns in this example. The penetration phase is followed by an "equilibration" phase. It is noted that the periods of the three phases strongly depend on the trajectory. Fig. 3-4c shows that the untrapped insertion process in this example almost follows the minimum energy path of the 2D-PMF surface.

Next, I examine the trapped membrane insertion of pTB. A characteristic example of a trapped insertion of pTB is shown in Fig. 3-5. After the initial “landing” phase, the pTB starts penetrating the membrane led by Mhe with a tilt angle of 73^0. The Mhe reaches at r = ~ 25 Å in ~ 220 ns, with a tilt angle of ~ 60^0, corresponding to the first step of the “penetration” phase. As seen in Fig. 3-5a, the N-terminal was not able to move much from there and stayed there for ~ 400 ns before penetrating into the lower leaflet, i.e., the pTB got trapped in the upper leaflet for the “quiescent period” of ~ 400 ns (see inset of Fig. 3-5b). The trapping occurs because the C-terminal tries to go deep inside the headgroup region of the upper leaflet in the meantime, instead of staying near the surface of the upper leaflet as in the case of untrapped insertion trajectories. This corresponds to the “shoulder region” of the 1D-PMF profile, and is a result of the stabilization of the hydrophilic and hydrophobic interactions between the terminals of pTB and the head-tail groups of the upper leaflet. A trapped insertion can be distinguished from the untrapped one by the distribution of large tilt angles in the shoulder region, as highlighted in Fig. 3-5c.

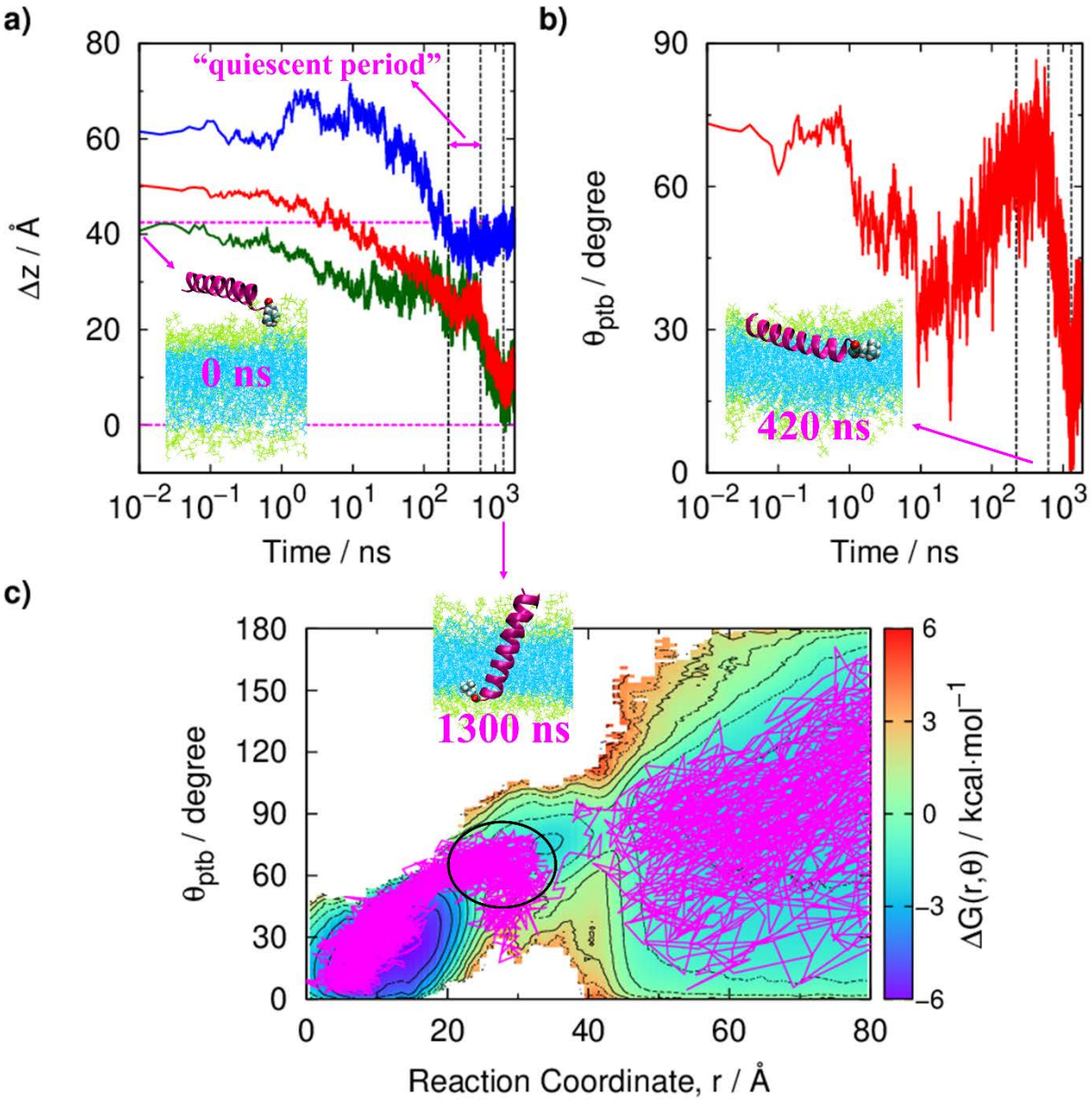

Figure 3-5: Characteristic example of a trapped insertion of pTB. Time courses of **(a)** reaction coordinate, r (dark-green), z-distances of the N- (red) and C- (blue) terminals from the membrane surface of the lower leaflet, and **(b)** tilt angle, θ_{ptb}, during insertion. **(c)** Mapping of (r, θ_{ptb}) values on the 2D-PMF profile using pink lines. In the top left figure, the transition state (Δz = 42.5 Å) and the membrane surface of the lower leaflet (Δz = 0 Å) are marked by pink dashed lines. Characteristic times 220, 620, and 1300 ns are marked with black dashed lines. Snapshot images at 0, 420, and 1300 ns are also shown. In the snapshot images, pTB is represented as a magenta ribbon model with Mhe shown as a van der Waals sphere model, and the membrane as thin stick models with lipid head and tail groups in light-green and cyan colors, respectively. For clarity, water and ions are not shown in the snapshot images. The "quiescent period" during the trapped insertion is highlighted in the top left figure, and the evolution of (r, θ_{ptb}) during the quiescent period is marked with a black oval in the bottom figure.

When the C-terminal is closer to the surface of the upper leaflet again, the pTB starts the second step of the penetration phase at t = 620 ns with a tilt angle of ~ 60^0. As seen in Fig. 3-5a, Mhe paves the way for the further penetration of pTB when restarting the insertion after the quiescent period. Finally, the pTB gets fully inserted into the membrane at t = 1300 ns with a tilt angle of ~ 15^0. The duration of the second step of the penetration phase is ~ 680 ns. Due to the trapping of pTB in the upper leaflet, the penetration phase took much longer time than that of the untrapped insertion. This was followed by an "equilibration" phase. Interestingly, the trapped insertion process in this example also almost follows the minimum energy path of the 2D-PMF surface, as seen in Fig. 3-5c.

The "surface adsorbed" phase seen in the spontaneous insertion of thermostable peptides[44,46] is not observed in the case of pTB because of the strong hydrophobicity of the N-terminal. That's the reason the 1D-PMF profile has the TS at the membrane surface instead of a free energy well. For the highly hydrophobic N-terminal of pTB, staying inside the hydrophobic core of the membrane is energetically more favorable than staying at the surface. To maximize the interaction of pTB with the membrane, the N-terminal stays at the head/tail interface of the lower leaflet while the C-terminal stays at the surface of the upper leaflet in the fully membrane inserted state.

Different from the membrane insertion of pTB, the penetration phase is followed by a "sliding" phase in the insertion pathway for the membrane uptake of carbon nanotubes.[78] The sliding phase, where the carbon nanotube slides along its axis deeper into the hydrophobic core of the membrane, is due to the lack of strong interactions of the rather hydrophobic carbon nanotube with the hydrophilic headgroups of the membrane. On the other hand, the membrane insertion of pTB is a result of the strong interactions of pTB with both the head and tail groups of the membrane, arising from

the structural asymmetry of pTB. As a result, the sliding phase is not observed in the insertion of pTB.

In both trapped and untrapped insertions, the pore of pTB allows the water molecules to permeate through the channel in a single-file fashion, as found in my previous study.[27] It is found that the water column inside the pTB is carried during the membrane penetration process, and is connected to bulk water from the C-terminal side as the penetration occurs with the N-terminal side. Once the pTB is fully inserted into the membrane, the water column near the N-terminal side also connects to bulk water from the other side. A similar mechanism was recently reported for the gramicidin A (gA) dimerization process to form the gA channel inside the membrane.[80] The water columns inside the two gA monomers join at the membrane center and connect to bulk water from the other two terminals during the channel formation process.

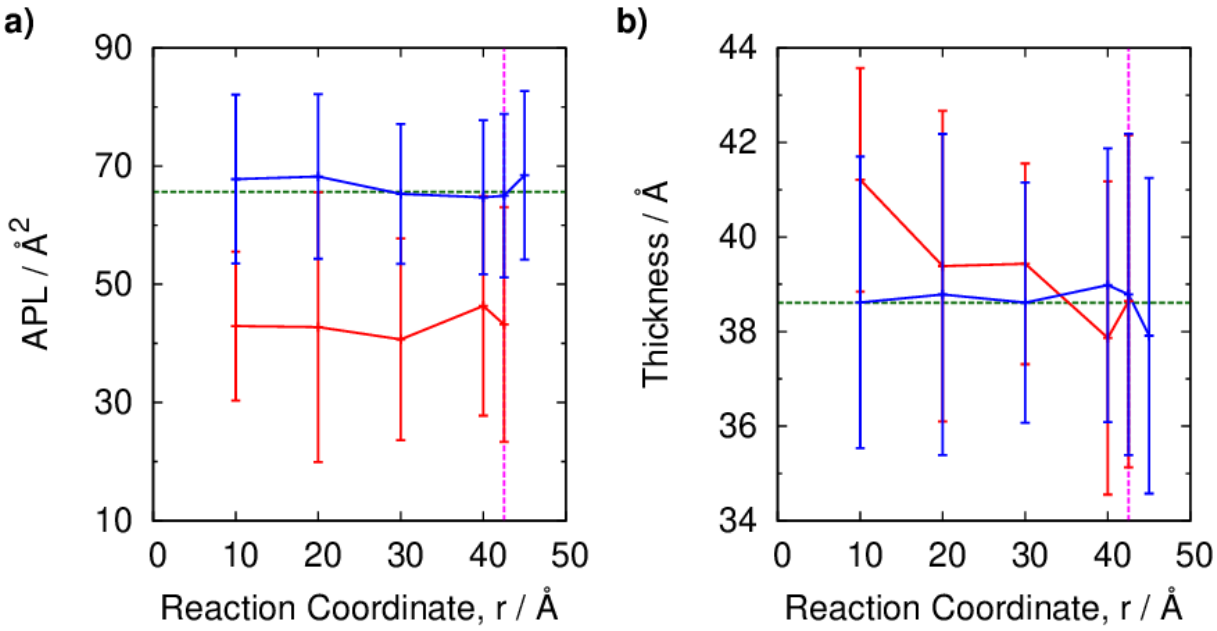

Figure 3-6: (a) Area per lipid (APL) and **(b)** membrane thickness for neighboring (red) and non-neighboring (blue) lipids as a function of the reaction coordinate, r. Standard deviations are shown as error bars. The equilibrium values before the insertion of pTB are marked with dark-green dashed lines. In the figures, r = 42.5 Å (transition state) is indicated with pink dashed lines.

To characterize the perturbation of the bilayer during the insertion of pTB, I examined the average APL and membrane thickness for r = 45, 42.5, 40, 30, 20, and 10 Å at their most probable angles, using the REUS simulation data. I first analyzed the Voronoi cells associated with the APL of lipids in the upper leaflet. The surface of the upper leaflet is chosen for the Voronoi analysis because the pTB did not cross the head/tail interface of the lower leaflet during insertion. The Voronoi polyhedra are constructed using the P atoms of lipid headgroups in the upper leaflet. The equilibrium APL and membrane thickness before the insertion are 65.6 Å^2 and 38.6 Å, respectively. The average APL and thickness of "neighboring" and "non-neighboring" lipids at characteristic r values

are shown in Fig. 3-6. Lipids in the first lipid shell around pTB are referred to as "neighboring" lipids and the rest as "non-neighboring" lipids. The Voronoi tessellations of the membrane surface at characteristic r values are shown in Fig. 3-7.

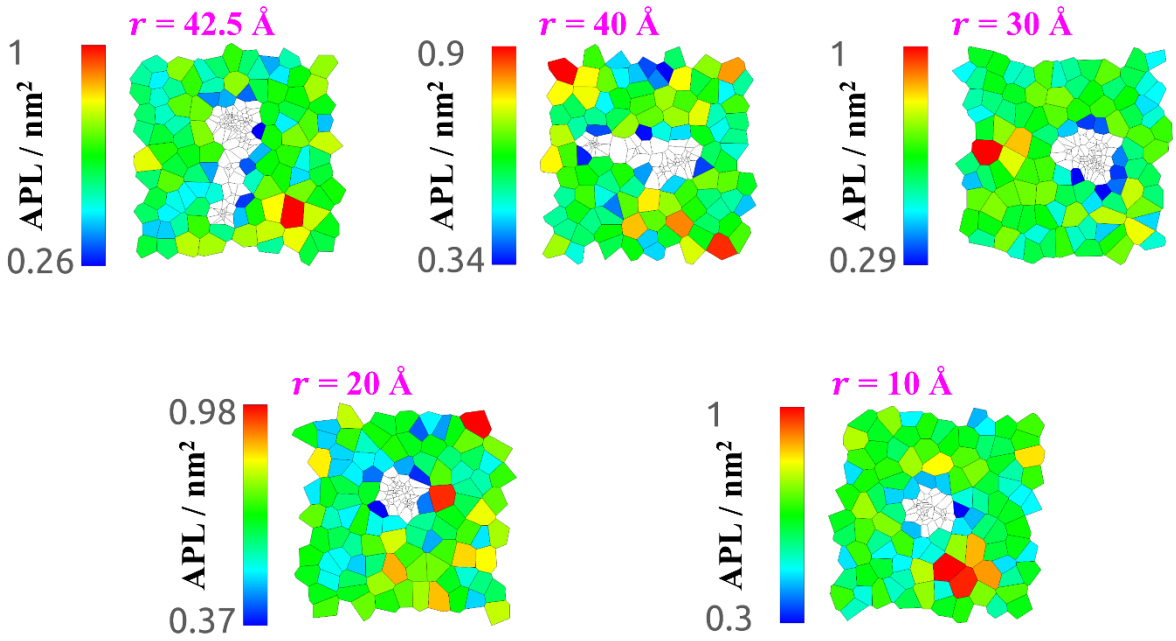

Figure 3-7: Voronoi cells associated with the area per lipid (APL) of lipids in the upper leaflet at r = 42.5, 40, 30, 20, and 10 Å. White areas in Voronoi diagrams correspond to the area occupied by pTB.

As seen in Fig. 3-6, both the APL and thickness of non-neighboring lipids, irrespective of r, remained close to the equilibrium value. The pTB is not present on the surface of the upper leaflet even at r = 45 Å and starts to touch the surface from the TS onwards. As a result, the APL of neighboring lipids from r = 42.5 Å onwards, decreases by ~ 35 % from the equilibrium value. The observed changes in the neighborhood of pTB during the insertion are because of the fact that the neighboring lipids need to make some spatial adjustments in order to occupy the inserted pTB channel. Interestingly, the APL even at the second lipid shell around pTB remained

close to the equilibrium value, as seen in Fig. 3-7. In addition, the density of the bilayer remained almost constant during the insertion, which I attribute to the large size of the bilayer chosen in this study. The present result shows that the insertion of pTB causes only the local lateral compression of the membrane and proceeds as “nanoneedle” like one proposed in the penetration of the carbon nanotube into the membrane.[81] On the other hand, the thickness at neighboring lipids slightly increases by ~ 5 % from the equilibrium value. This can be seen as a result of the small “hydrophobic mismatch”[54–56] in the case of pTB, i.e., the pTB channel has approximately the same thickness as the membrane it spans.

Conclusions

The membrane insertion process of pTB is explored in detail using all-atom MD simulations. My simulations show that the $\beta^{6.3}$-helix of pTB remained stable throughout the insertion process. The free energy calculations using the REUS simulations show that there is a small barrier of 4.3 kcal/mol located at the membrane surface for the membrane uptake of pTB from bulk water. Dissecting the free energy into enthalpic and entropic components reveals that the observed free energy barrier arises from the entropic bottleneck. The “shoulder” region in between the global free energy maximum and minimum corresponds to the trapping of pTB in the upper leaflet. The Voronoi cells associated with the APL suggest that the insertion of pTB proceeds with only the local lateral compression of the membrane. The small “hydrophobic mismatch” in the case of pTB helped the membrane thickness to remain almost constant during the insertion.

To elucidate the underlying mechanism of the spontaneous membrane insertion of pTB, I performed multiple unbiased MD simulations. My results reinforce the experimental observation of the spontaneous membrane insertion of pTB led by the hydrophobic N-terminal.[16] The spontaneous membrane uptake of pTB occurs in three

consecutive phases: “landing,” “penetration,” and “equilibration” phases. My simulations suggest two possible insertion pathways, namely “trapped” and “untrapped” insertions, depending on whether or not pTB is trapped in the upper leaflet during the penetration phase.

The present study is the first theoretical and computational study of the spontaneous membrane insertion of a β-helical peptide, and provides useful insights to understand the membrane insertion mechanism of other spontaneously inserting prefolded single transmembrane peptides. My results on the “vectorial insertion” of pTB, where the membrane uptake of pTB from bulk water is anchored by the highly hydrophobic N-terminal blocking group (Mhe), further emphasize the significance of membrane anchoring for the vectorial insertion of transmembrane peptides. Since recently there have been several studies on the total synthesis[24,82,83] and the biomimetic synthesis[84,85] of pTB, the understanding of the membrane insertion of pTB can help in the biosynthesis of pTB and the de novo design of peptides and therapeutic drugs that can exhibit spontaneous vectorial insertion into target cell membranes.[57]

The cytotoxicity of pTB is related to its channel activity across the target cell membrane after spontaneously inserting into the membrane.[16] It has been reported in experiments that the pTB channel allows permeation of monovalent cations with the current in the order of $H^+ > Cs^+ > Rb^+ > K^+ > Na^+ > Li^+$.[16,25,26] It is, therefore, important to understand the ion permeation mechanism of the pTB channel, which is not well understood both experimentally and theoretically.

Supporting Information

Energy Decomposition Analysis

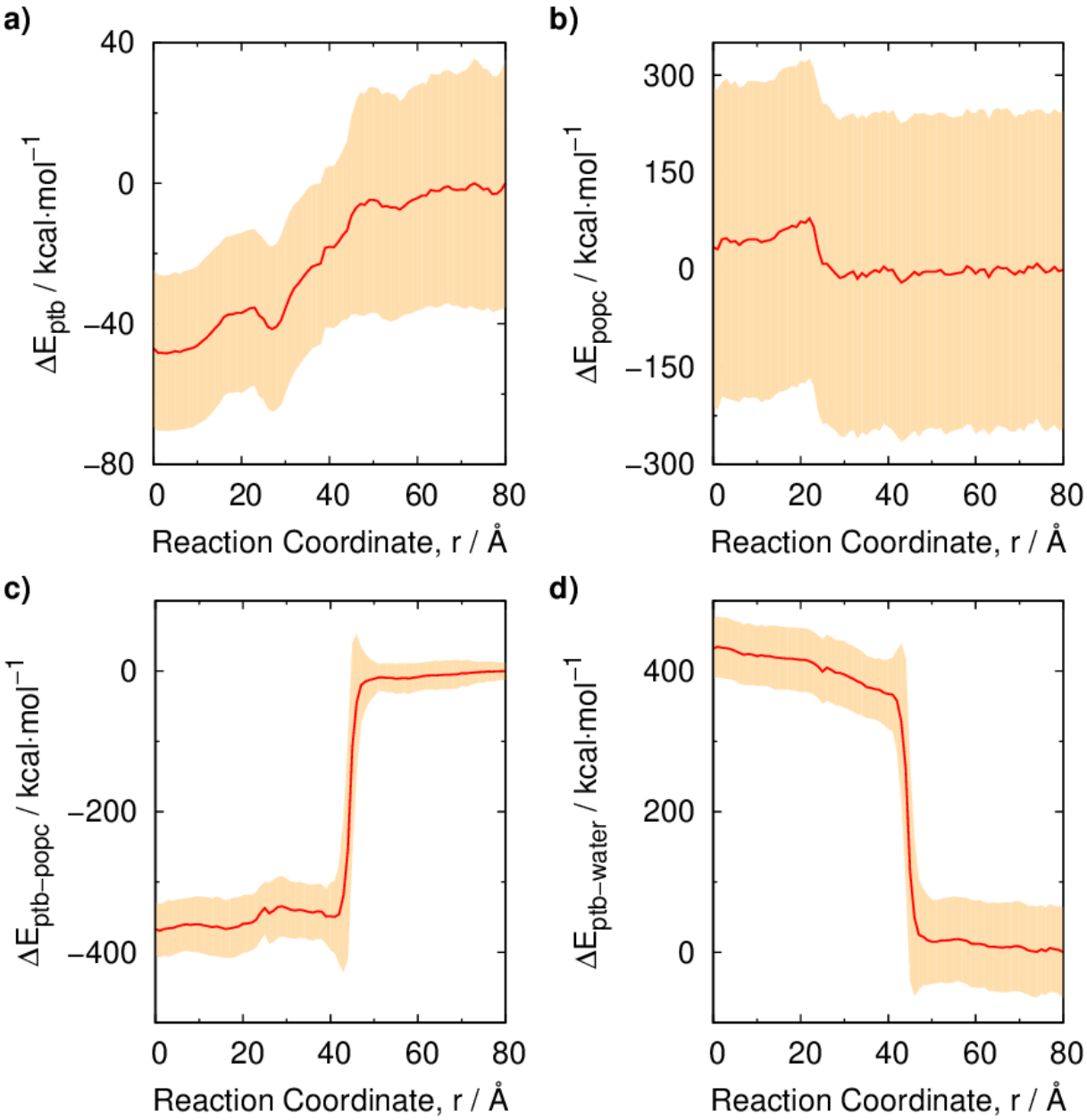

Figure S3-1: Average potential energies along the reaction coordinate, r. Standard deviations of the energies are represented by shaded regions. **(a)** Total energy of pTB. **(b)** Total energy of POPC bilayer. **(c)** Intermolecular energy between pTB and POPC bilayer. **(d)** Intermolecular energy between pTB and water molecules.

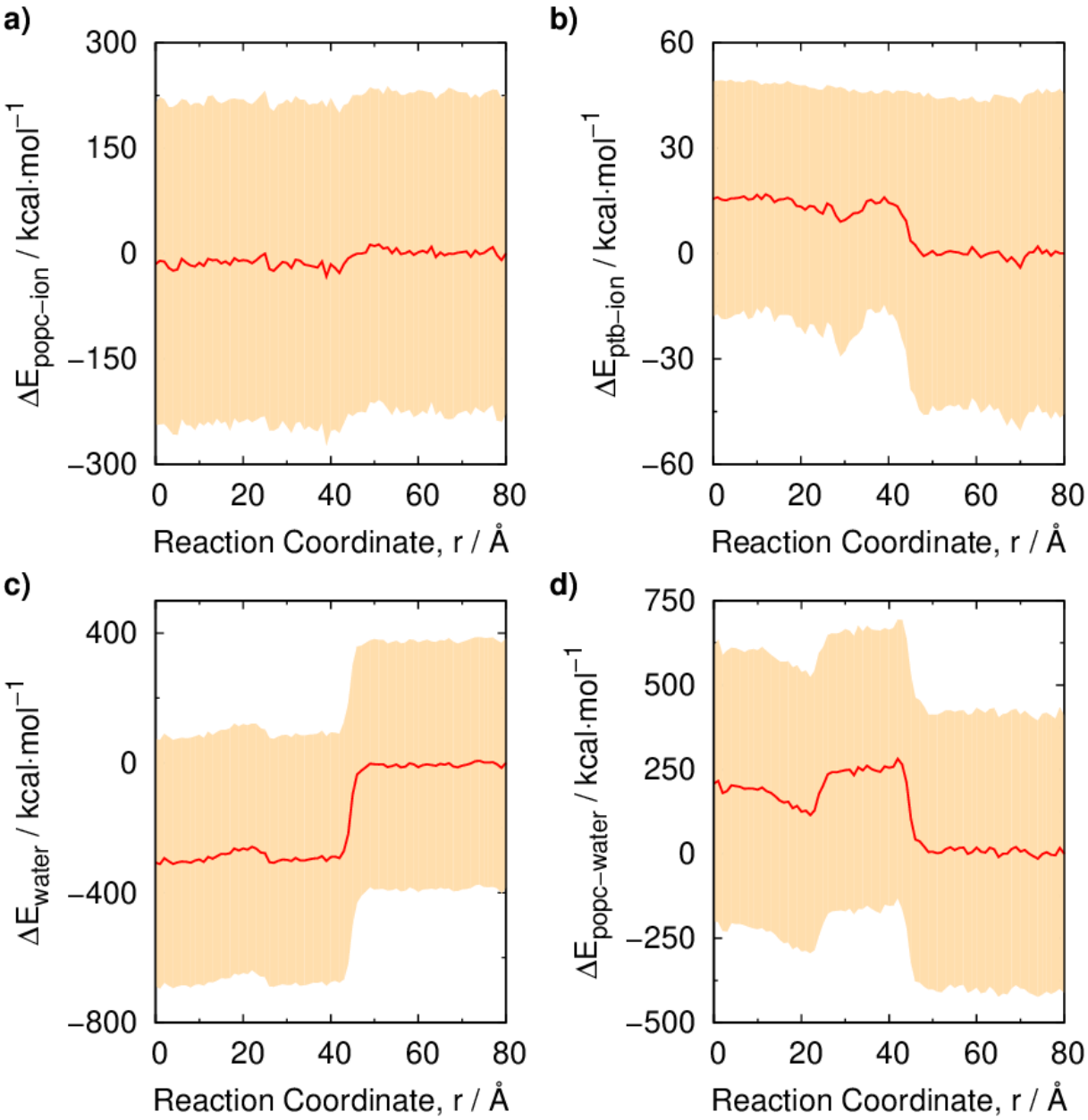

Figure S3-2: Average potential energies along the reaction coordinate, r. Standard deviations of the energies are represented by shaded regions. **(a)** Intermolecular energy between POPC bilayer and ions. **(b)** Intermolecular energy between pTB and ions. **(c)** Intermolecular energy between water molecules. **(d)** Intermolecular energy between POPC bilayer and water molecules.

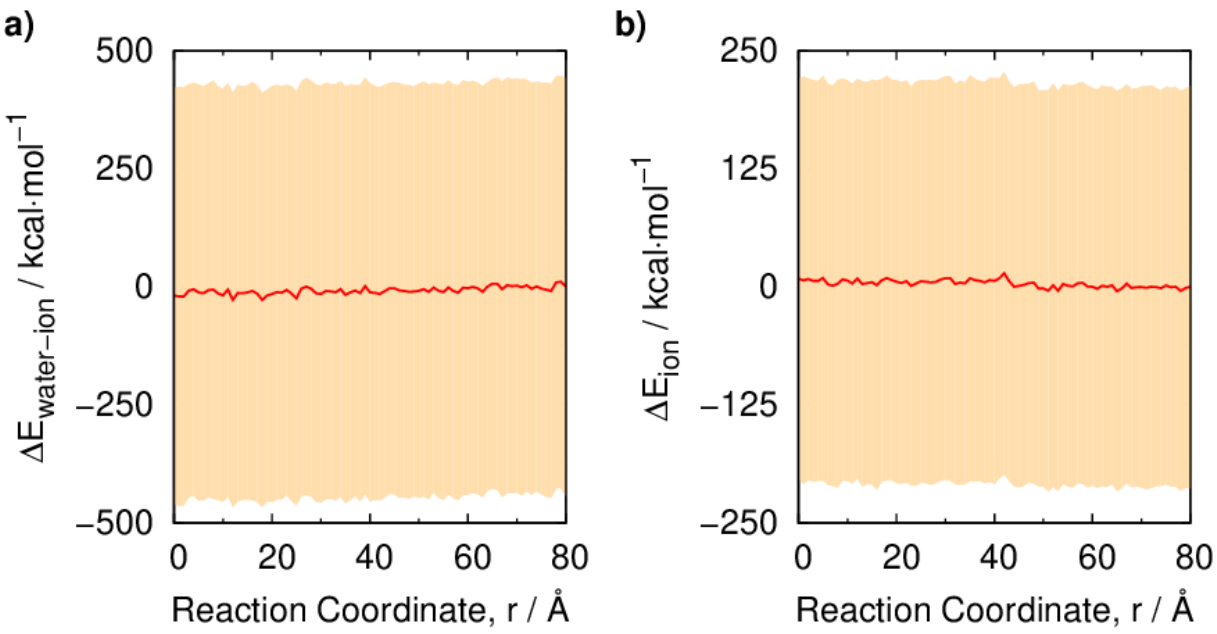

Figure S3-3: Average potential energies along the reaction coordinate, r. Standard deviations of the energies are represented by shaded regions. **(a)** Intermolecular energy between water molecules and ions. **(b)** Intermolecular energy between ions.

Untrapped Insertion Trajectories

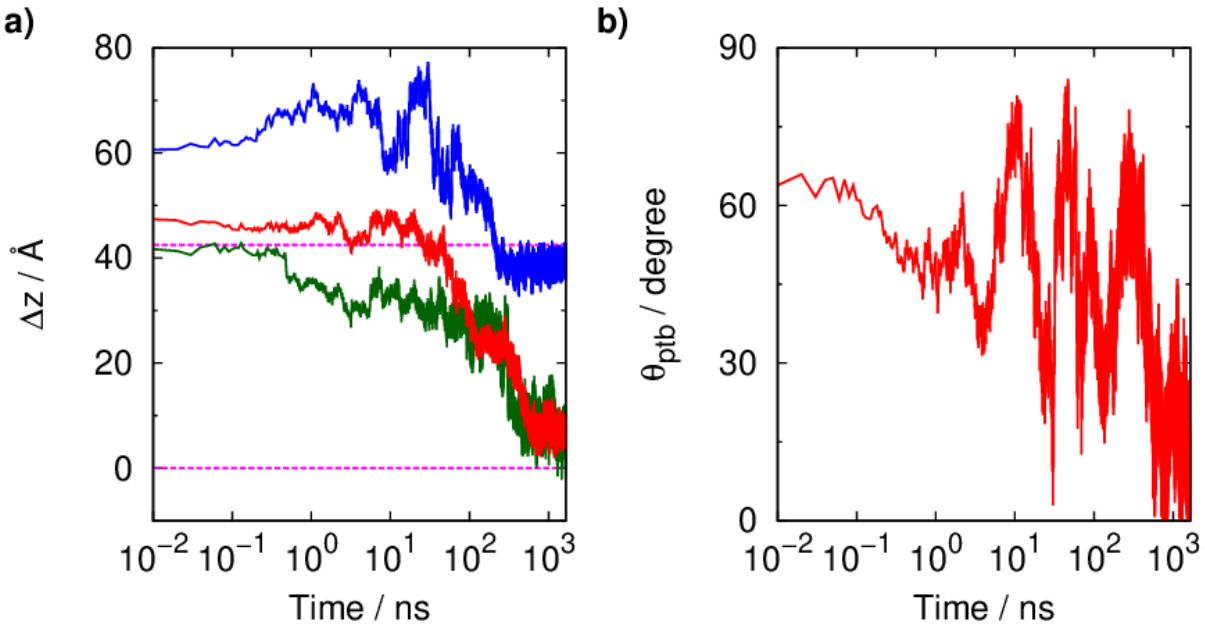

Figure S3-4: Time courses of **(a)** reaction coordinate, r (dark-green), z-distances of the N- (red) and C- (blue) terminals from the membrane surface of the lower leaflet, and **(b)** tilt angle, θ_{ptb}, during insertion. In the left figure, the transition state ($\Delta z = 42.5$ Å) and the membrane surface of the lower leaflet ($\Delta z = 0$ Å) are marked by pink dashed lines.

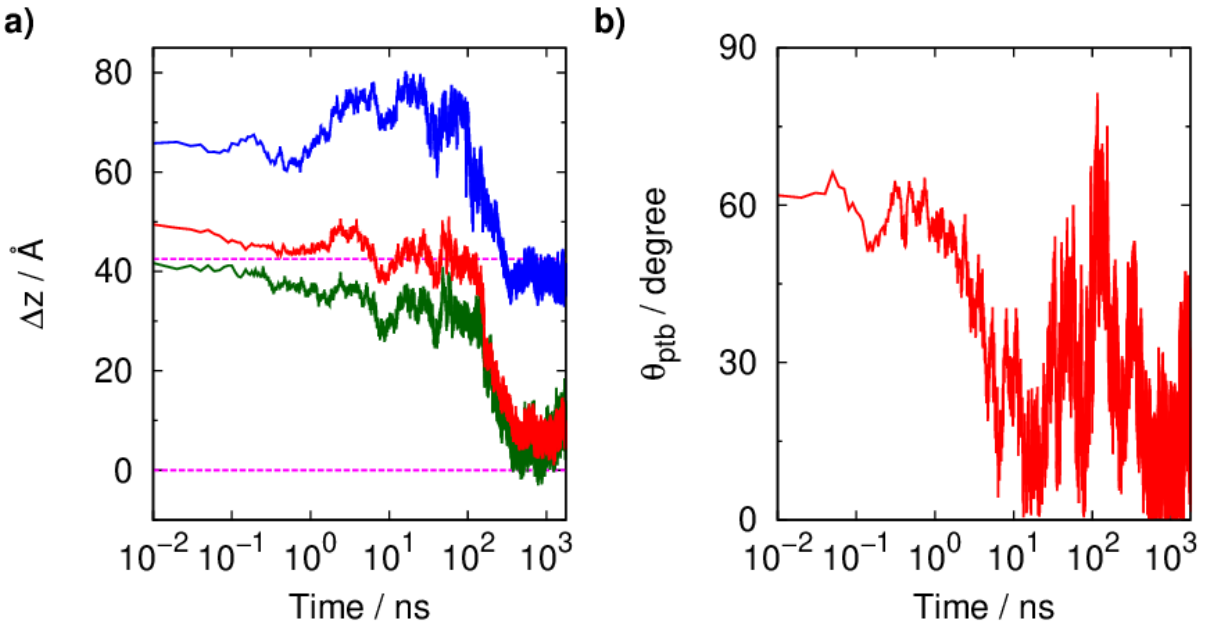

Figure S3-5: Time courses of **(a)** reaction coordinate, r (dark-green), z-distances of the N- (red) and C- (blue) terminals from the membrane surface of the lower leaflet, and **(b)** tilt angle, θ_{ptb}, during insertion. In the left figure, the transition state ($\Delta z =$ 42.5 Å) and the membrane surface of the lower leaflet ($\Delta z =$ 0 Å) are marked by pink dashed lines.

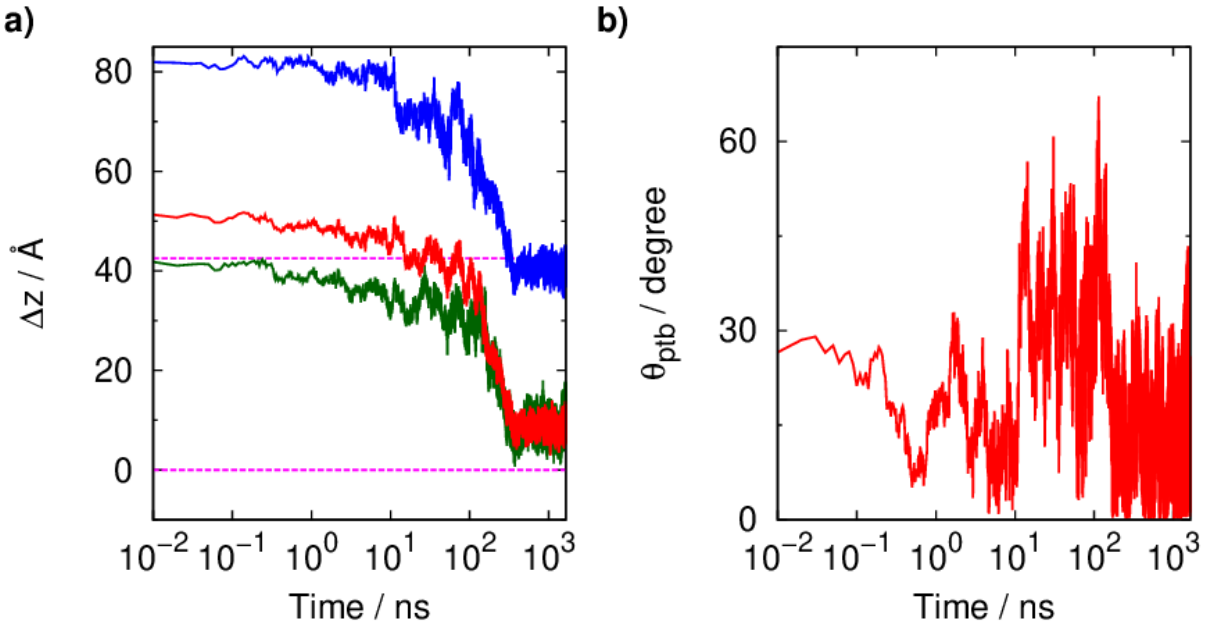

Figure S3-6: Time courses of **(a)** reaction coordinate, r (dark-green), z-distances of the N- (red) and C- (blue) terminals from the membrane surface of the lower leaflet, and **(b)** tilt angle, θ_{ptb}, during insertion. In the left figure, the transition state ($\Delta z =$ 42.5 Å) and the membrane surface of the lower leaflet ($\Delta z =$ 0 Å) are marked by pink dashed lines.

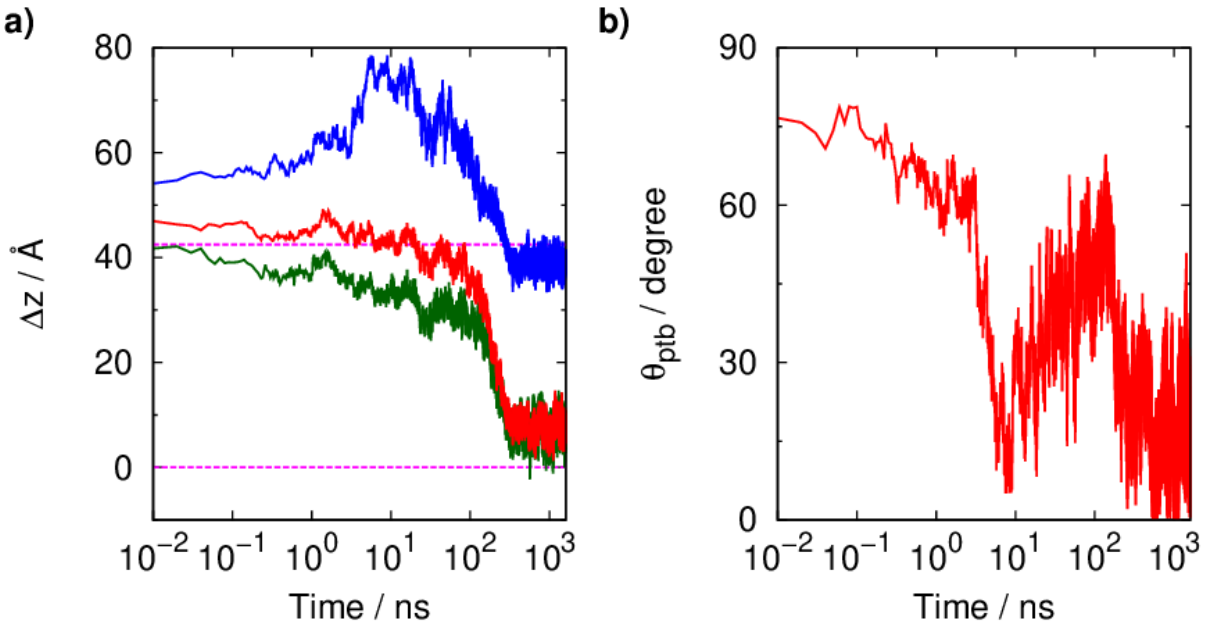

Figure S3-7: Time courses of **(a)** reaction coordinate, r (dark-green), z-distances of the N- (red) and C- (blue) terminals from the membrane surface of the lower leaflet, and **(b)** tilt angle, θ_{ptb}, during insertion. In the left figure, the transition state ($\Delta z = 42.5$ Å) and the membrane surface of the lower leaflet ($\Delta z = 0$ Å) are marked by pink dashed lines.

Trapped Insertion Trajectories

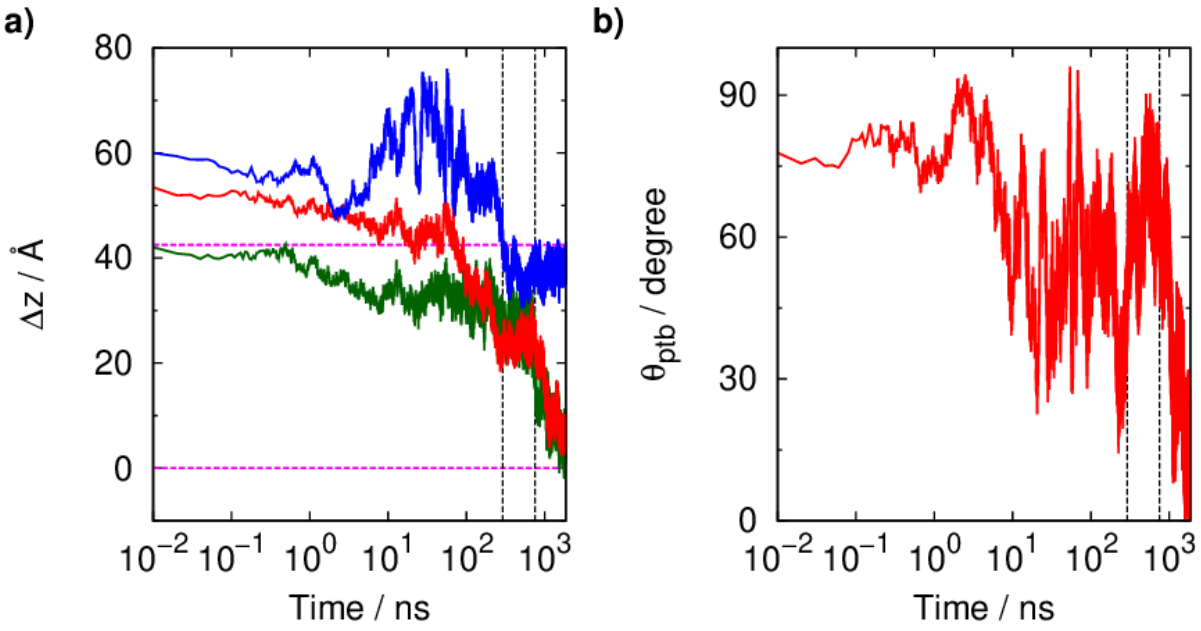

Figure S3-8: Time courses of **(a)** reaction coordinate, r (dark-green), z-distances of the N- (red) and C- (blue) terminals from the membrane surface of the lower leaflet, and **(b)** tilt angle, θ_{ptb}, during insertion. In the left figure, the transition state ($\Delta z = 42.5$ Å) and the membrane surface of the lower leaflet ($\Delta z = 0$ Å) are marked by pink dashed lines. The quiescent period is marked as the time spent between the two black dashed lines, and is ~ 450 ns.

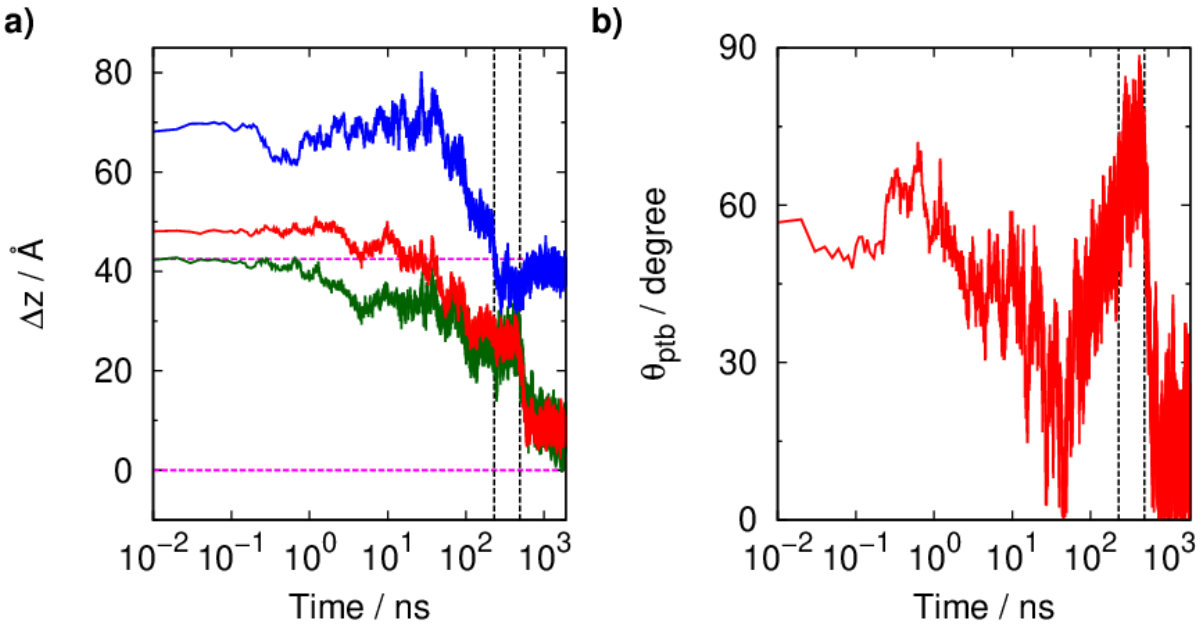

Figure S3-9: Time courses of **(a)** reaction coordinate, r (dark-green), z-distances of the N- (red) and C- (blue) terminals from the membrane surface of the lower leaflet, and **(b)** tilt angle, θ_{ptb}, during insertion. In the left figure, the transition state ($\Delta z =$ 42.5 Å) and the membrane surface of the lower leaflet ($\Delta z =$ 0 Å) are marked by pink dashed lines. The quiescent period is marked as the time spent between the two black dashed lines, and is ~ 250 ns.

References

(1) Sandvig, K.; van Deurs, B. Membrane Traffic Exploited by Protein Toxins. *Annu. Rev. Cell Dev. Biol.* **2002**, *18* (1), 1–24.

(2) Minna M. Poranen; Rimantas Daugelavičius; Bamford, D. H. Common Principles in Viral Entry. *Annu. Rev. Microbiol.* **2002**, *56* (1), 521–538.

(3) Yeaman, M. R.; Yount, N. Y. Mechanisms of Antimicrobial Peptide Action and Resistance. *Pharmacol. Rev.* **2003**, *55* (1), 27–55.

(4) Lee, M.-T.; Chen, F.-Y.; Huang, H. W. Energetics of Pore Formation Induced by Membrane Active Peptides. *Biochemistry* **2004**, *43* (12), 3590–3599.

(5) White, S. H.; von Heijne, G. The Machinery of Membrane Protein Assembly. *Curr. Opin. Struct. Biol.* **2004**, *14* (4), 397–404.

(6) White, S. H.; von Heijne, G. Transmembrane Helices before, during, and after Insertion. *Curr. Opin. Struct. Biol.* **2005**, *15* (4), 378–386.

(7) Hessa, T.; Kim, H.; Bihlmaier, K.; Lundin, C.; Boekel, J.; Andersson, H.; Nilsson, I.; White, S. H.; von Heijne, G. Recognition of Transmembrane Helices by the Endoplasmic Reticulum Translocon. *Nature* **2005**, *433*, 377.

(8) White, S. H.; von Heijne, G. How Translocons Select Transmembrane Helices. *Annu. Rev. Biophys.* **2008**, *37* (1), 23–42.

(9) Jaud, S.; Fernández-Vidal, M.; Nilsson, I.; Meindl-Beinker, N. M.; Hübner, N. C.; Tobias, D. J.; von Heijne, G.; White, S. H. Insertion of Short Transmembrane Helices by the Sec61 Translocon. *Proc. Natl. Acad. Sci.* **2009**, *106* (28), 11588–11593.

(10) Schlamadinger, D. E.; Wang, Y.; McCammon, J. A.; Kim, J. E. Spectroscopic and Computational Study of Melittin, Cecropin A, and the Hybrid Peptide CM15. *J. Phys. Chem. B* **2012**, *116* (35), 10600–10608.

(11) Bechinger, B. Structure and Functions of Channel-Forming Peptides: Magainins, Cecropins, Melittin and Alamethicin. *J. Membr. Biol.* **1997**, *156* (3), 197–211.

(12) Sato, H.; Feix, J. B. Peptide–Membrane Interactions and Mechanisms of Membrane Destruction by Amphipathic α-Helical Antimicrobial Peptides. *Biochim. Biophys. Acta - Biomembr.* **2006**, *1758* (9), 1245–1256.

(13) Ulmschneider, J. P. Charged Antimicrobial Peptides Can Translocate across Membranes without Forming Channel-like Pores. *Biophys. J.* **2017**, *113* (1), 73–81.

(14) Upadhyay, S. K.; Wang, Y.; Zhao, T.; Ulmschneider, J. P. Insights from Micro-Second Atomistic Simulations of Melittin in Thin Lipid Bilayers. *J. Membr. Biol.* **2015**, *248* (3), 497–503.

(15) Wang, Y.; Chen, C. H.; Hu, D.; Ulmschneider, M. B.; Ulmschneider, J. P. Spontaneous Formation of Structurally Diverse Membrane Channel

Architectures from a Single Antimicrobial Peptide. *Nat. Commun.* **2016**, *7* (1), 13535.

(16) Iwamoto, M.; Shimizu, H.; Muramatsu, I.; Oiki, S. A Cytotoxic Peptide from a Marine Sponge Exhibits Ion Channel Activity through Vectorial-Insertion into the Membrane. *FEBS Lett.* **2010**, *584* (18), 3995–3999.

(17) Gumbart, J.; Chipot, C.; Schulten, K. Free-Energy Cost for Translocon-Assisted Insertion of Membrane Proteins. *Proc. Natl. Acad. Sci.* **2011**, *108* (9), 3596–3601.

(18) Yue, T.; Sun, M.; Zhang, S.; Ren, H.; Ge, B.; Huang, F. How Transmembrane Peptides Insert and Orientate in Biomembranes: A Combined Experimental and Simulation Study. *Phys. Chem. Chem. Phys.* **2016**, *18* (26), 17483–17494.

(19) Hamada, T.; Sugawara, T.; Matsunaga, S.; Fusetani, N. Polytheonamides, Unprecedented Highly Cytotoxic Polypeptides, from the Marine Sponge Theonella Swinhoei. *Tetrahedron Lett.* **1994**, *35* (5), 719–720.

(20) Oiki, S.; Muramatsu, I.; Matsunaga, S.; Fusetani, N. A Channel-Forming Peptide Toxin: Polytheonamide from Marine Sponge (Theonella Swinhoei). *Nihon Yakurigaku Zasshi.* **1997**, *110* (Suppl. 1), 195P-198P.

(21) Hamada, T.; Matsunaga, S.; Yano, G.; Fusetani, N. Polytheonamides A and B, Highly Cytotoxic, Linear Polypeptides with Unprecedented Structural Features, from the Marine Sponge, Theonella Swinhoei. *J. Am. Chem. Soc.* **2005**, *127* (1), 110–118.

(22) Hamada, T.; Matsunaga, S.; Fujiwara, M.; Fujita, K.; Hirota, H.; Schmucki, R.; Güntert, P.; Fusetani, N. Solution Structure of Polytheonamide B, a Highly Cytotoxic Nonribosomal Polypeptide from Marine Sponge. *J. Am. Chem. Soc.* **2010**, *132* (37), 12941–12945.

(23) Mori, T.; Kokubo, H.; Oiki, S.; Okamoto, Y. Dynamic Structure of the Polytheonamide B Channel Studied by Normal Mode Analysis. *Mol. Simul.* **2011**, *37* (12), 975–985.

(24) Shinohara, N.; Itoh, H.; Matsuoka, S.; Inoue, M. Selective Modification of the N-Terminal Structure of Polytheonamide B Significantly Changes Its Cytotoxicity and Activity as an Ion Channel. *ChemMedChem* **2012**, *7* (10), 1770–1773.

(25) Iwamoto, M.; Matsunaga, S.; Oiki, S. Paradoxical One-Ion Pore Behavior of the Long β-Helical Peptide of Marine Cytotoxic Polytheonamide B. *Sci. Rep.* **2014**, *4*, 3636.

(26) Matsuki, Y.; Iwamoto, M.; Mita, K.; Shigemi, K.; Matsunaga, S.; Oiki, S. Rectified Proton Grotthuss Conduction Across a Long Water-Wire in the Test Nanotube of the Polytheonamide B Channel. *J. Am. Chem. Soc.* **2016**, *138* (12), 4168–4177.

(27) Kalathingal, M.; Sumikama, T.; Mori, T.; Oiki, S.; Saito, S. Structure and Dynamics of Solvent Molecules inside the Polytheonamide B Channel in Different Environments: A Molecular Dynamics Study. *Phys. Chem. Chem. Phys.* **2018**, *20* (5), 3334–3348.
(28) Renevey, A.; Riniker, S. The Importance of N-Methylations for the Stability of the B6.3 -Helical Conformation of Polytheonamide B. *Eur. Biophys. J.* **2017**, *46* (4), 363–374.
(29) Andersen, O. S.; Koeppe, R. E.; Roux, B. Gramicidin Channels. *IEEE Trans. Nanobioscience* **2005**, *4* (1), 10–20.
(30) Iwamoto, M.; Oiki, S. Contact Bubble Bilayers with Flush Drainage. *Sci. Rep.* **2015**, *5*, 9110.
(31) Iwamoto, M.; Oiki, S. Membrane Perfusion of Hydrophobic Substances Around Channels Embedded in the Contact Bubble Bilayer. *Sci. Rep.* **2017**, *7* (1), 6857.
(32) Johansson, A. C. V.; Lindahl, E. Position-Resolved Free Energy of Solvation for Amino Acids in Lipid Membranes from Molecular Dynamics Simulations. *Proteins Struct. Funct. Bioinforma.* **2007**, *70* (4), 1332–1344.
(33) MacCallum, J. L.; Bennett, W. F. D.; Tieleman, D. P. Partitioning of Amino Acid Side Chains into Lipid Bilayers: Results from Computer Simulations and Comparison to Experiment. *J. Gen. Physiol.* **2007**, *129* (5), 371–377.
(34) Dorairaj, S.; Allen, T. W. On the Thermodynamic Stability of a Charged Arginine Side Chain in a Transmembrane Helix. *Proc. Natl. Acad. Sci.* **2007**, *104* (12), 4943–4948.
(35) Gumbart, J.; Roux, B. Determination of Membrane-Insertion Free Energies by Molecular Dynamics Simulations. *Biophys. J.* **2012**, *102* (4), 795–801.
(36) Gumbart, J. C.; Ulmschneider, M. B.; Hazel, A.; White, S. H.; Ulmschneider, J. P. Computed Free Energies of Peptide Insertion into Bilayers Are Independent of Computational Method. *J. Membr. Biol.* **2018**, *251* (3), 345–356.
(37) Babakhani, A.; Gorfe, A. A.; Kim, J. E.; McCammon, J. A. Thermodynamics of Peptide Insertion and Aggregation in a Lipid Bilayer. *J. Phys. Chem. B* **2008**, *112* (34), 10528–10534.
(38) Irudayam, S. J.; Pobandt, T.; Berkowitz, M. L. Free Energy Barrier for Melittin Reorientation from a Membrane-Bound State to a Transmembrane State. *J. Phys. Chem. B* **2013**, *117* (43), 13457–13463.
(39) Yeh, I.-C.; Olson, M. A.; Lee, M. S.; Wallqvist, A. Free-Energy Profiles of Membrane Insertion of the M2 Transmembrane Peptide from Influenza A Virus. *Biophys. J.* **2008**, *95* (11), 5021–5029.
(40) Tieleman, D. P.; Sansom, M. S. P. Molecular Dynamics Simulations of Antimicrobial Peptides: From Membrane Binding to Trans-Membrane Channels. *Int. J. Quantum Chem.* **2001**, *83* (3–4), 166–179.

(41) Santo, K. P.; Berkowitz, M. L. Difference between Magainin-2 and Melittin Assemblies in Phosphatidylcholine Bilayers: Results from Coarse-Grained Simulations. *J. Phys. Chem. B* **2012**, *116* (9), 3021–3030.
(42) Santo, K. P.; Irudayam, S. J.; Berkowitz, M. L. Melittin Creates Transient Pores in a Lipid Bilayer: Results from Computer Simulations. *J. Phys. Chem. B* **2013**, *117* (17), 5031–5042.
(43) Pokhrel, R.; Bhattarai, N.; Baral, P.; Gerstman, B. S.; Park, J. H.; Handfield, M.; Chapagain, P. P. Molecular Mechanisms of Pore Formation and Membrane Disruption by the Antimicrobial Lantibiotic Peptide Mutacin 1140. *Phys. Chem. Chem. Phys.* **2019**, *21* (23), 12530–12539.
(44) Ulmschneider, M. B.; Doux, J. P. F.; Killian, J. A.; Smith, J. C.; Ulmschneider, J. P. Mechanism and Kinetics of Peptide Partitioning into Membranes from All-Atom Simulations of Thermostable Peptides. *J. Am. Chem. Soc.* **2010**, *132* (10), 3452–3460.
(45) Ulmschneider, M. B.; Smith, J. C.; Ulmschneider, J. P. Peptide Partitioning Properties from Direct Insertion Studies. *Biophys. J.* **2010**, *98* (12), L60–L62.
(46) Ulmschneider, J. P.; Smith, J. C.; White, S. H.; Ulmschneider, M. B. In Silico Partitioning and Transmembrane Insertion of Hydrophobic Peptides under Equilibrium Conditions. *J. Am. Chem. Soc.* **2011**, *133* (39), 15487–15495.
(47) Ulmschneider, M. B.; Ulmschneider, J. P.; Schiller, N.; Wallace, B. A.; von Heijne, G.; White, S. H. Spontaneous Transmembrane Helix Insertion Thermodynamically Mimics Translocon-Guided Insertion. *Nat. Commun.* **2014**, *5* (1), 4863.
(48) Deng, Y.; Qian, Z.; Luo, Y.; Zhang, Y.; Mu, Y.; Wei, G. Membrane Binding and Insertion of a PHLIP Peptide Studied by All-Atom Molecular Dynamics Simulations. *Int. J. Mol. Sci.* **2013**, *14* (7), 14532–14549.
(49) Herce, H. D.; Garcia, A. E. Molecular Dynamics Simulations Suggest a Mechanism for Translocation of the HIV-1 TAT Peptide across Lipid Membranes. *Proc. Natl. Acad. Sci.* **2007**, *104* (52), 20805–20810.
(50) Nymeyer, H.; Woolf, T. B.; Garcia, A. E. Folding Is Not Required for Bilayer Insertion: Replica Exchange Simulations of an α-Helical Peptide with an Explicit Lipid Bilayer. *Proteins Struct. Funct. Bioinforma.* **2005**, *59* (4), 783–790.
(51) Im, W.; Brooks, C. L. Interfacial Folding and Membrane Insertion of Designed Peptides Studied by Molecular Dynamics Simulations. *Proc. Natl. Acad. Sci.* **2005**, *102* (19), 6771–6776.
(52) Ulmschneider, M. B.; Ulmschneider, J. P. Folding Peptides into Lipid Bilayer Membranes. *J. Chem. Theory Comput.* **2008**, *4* (11), 1807–1809.
(53) Ulmschneider, J. P.; Doux, J. P. F.; Killian, J. A.; Smith, J. C.; Ulmschneider, M.

B. Peptide Partitioning and Folding into Lipid Bilayers. *J. Chem. Theory Comput.* **2009**, *5* (9), 2202–2205.

(54) Nielsen, C.; Andersen, O. S. Inclusion-Induced Bilayer Deformations: Effects of Monolayer Equilibrium Curvature. *Biophys. J.* **2000**, *79* (5), 2583–2604.

(55) Bruno, M. J.; Koeppe, R. E.; Andersen, O. S. Docosahexaenoic Acid Alters Bilayer Elastic Properties. *Proc. Natl. Acad. Sci.* **2007**, *104* (23), 9638–9643.

(56) Yoo, J.; Cui, Q. Membrane-Mediated Protein-Protein Interactions and Connection to Elastic Models: A Coarse-Grained Simulation Analysis of Gramicidin A Association. *Biophys. J.* **2013**, *104* (1), 128–138.

(57) Wimley, W. C.; White, S. H. Designing Transmembrane α-Helices That Insert Spontaneously †. *Biochemistry* **2000**, *39* (15), 4432–4442.

(58) Maier, J. A.; Martinez, C.; Kasavajhala, K.; Wickstrom, L.; Hauser, K. E.; Simmerling, C. Ff14SB: Improving the Accuracy of Protein Side Chain and Backbone Parameters from Ff99SB. *J. Chem. Theory Comput.* **2015**, *11* (8), 3696–3713.

(59) Jorgensen, W. L.; Chandrasekhar, J.; Madura, J. D.; Impey, R. W.; Klein, M. L. Comparison of Simple Potential Functions for Simulating Liquid Water. *J. Chem. Phys.* **1983**, *79* (2), 926–935.

(60) Dickson, C. J.; Madej, B. D.; Skjevik, Å. A.; Betz, R. M.; Teigen, K.; Gould, I. R.; Walker, R. C. Lipid14: The Amber Lipid Force Field. *J. Chem. Theory Comput.* **2014**, *10* (2), 865–879.

(61) Joung, I. S.; Cheatham, T. E. Determination of Alkali and Halide Monovalent Ion Parameters for Use in Explicitly Solvated Biomolecular Simulations. *J. Phys. Chem. B* **2008**, *112* (30), 9020–9041.

(62) Case, D. A.; Ben-Shalom, I. Y.; Brozell, S. R.; Cerutti, D. S.; Cheatham, T. E.; III; Cruzeiro, V. W. D.; Darden, T. A.; Duke, R. E.; Ghoreishi, D.; Gilson, M. K.; Gohlke, H.; Goetz, A. W.; Greene, D.; Harris, R.; Homeyer, N.; Huang, Y.; Izadi, S.; Kovalenko, A.; Kurtzman, T.; Lee, T. S.; LeGrand, S.; Li, P.; Lin, C.; Liu, J.; Luchko, T.; Luo, R.; Mermelstein, D. J.; Merz, K. M.; Miao, Y.; Monard, G.; Nguyen, C.; Nguyen, H.; Omelyan, I.; Onufriev, A.; Pan, F.; Qi, R.; Roe, D. R.; Roitberg, A.; Sagui, C.; Schott-Verdugo, S.; Shen, J.; Simmerling, C. L.; Smith, J.; Salomon-Ferrer, R.; Swails, J.; Walker, R. C.; Wang, J.; Wei, H.; Wolf, R. M.; Wu, X.; Xiao, L.; York, D. M.; Kollman, P. A. AMBER 2018, University of California, San Francisco. 2018.

(63) Ryckaert, J.-P.; Ciccotti, G.; Berendsen, H. J. C. Numerical Integration of the Cartesian Equations of Motion of a System with Constraints: Molecular Dynamics of n-Alkanes. *J. Comput. Phys.* **1977**, *23* (3), 327–341.

(64) Darden, T.; York, D.; Pedersen, L. Particle Mesh Ewald: An $N \cdot \log(N)$ Method for Ewald Sums in Large Systems. *J. Chem. Phys.* **1993**, *98* (12), 10089–10092.

(65) Pastor, R. W.; Brooks, B. R.; Szabo, A. An Analysis of the Accuracy of Langevin and Molecular Dynamics Algorithms. *Mol. Phys.* **1988**, *65* (6), 1409–1419.

(66) Berendsen, H. J. C.; Postma, J. P. M.; van Gunsteren, W. F.; DiNola, A.; Haak, J. R. Molecular Dynamics with Coupling to an External Bath. *J. Chem. Phys.* **1984**, *81* (8), 3684–3690.

(67) Jo, S.; Lim, J. B.; Klauda, J. B.; Im, W. CHARMM-GUI Membrane Builder for Mixed Bilayers and Its Application to Yeast Membranes. *Biophys. J.* **2009**, *97* (1), 50–58.

(68) Press, W. H.; Teukolsky, S. A.; Vetterling, W. T.; Flannery, B. P. *Numerical Recipes 3rd Edition: The Art of Scientific Computing*; Cambridge University Press, 2007.

(69) Kučerka, N.; Nieh, M.-P.; Katsaras, J. Fluid Phase Lipid Areas and Bilayer Thicknesses of Commonly Used Phosphatidylcholines as a Function of Temperature. *Biochim. Biophys. Acta - Biomembr.* **2011**, *1808* (11), 2761–2771.

(70) Torrie, G. M.; Valleau, J. P. Nonphysical Sampling Distributions in Monte Carlo Free-Energy Estimation: Umbrella Sampling. *J. Comput. Phys.* **1977**, *23* (2), 187–199.

(71) Park, S.; Kim, T.; Im, W. Transmembrane Helix Assembly by Window Exchange Umbrella Sampling. *Phys. Rev. Lett.* **2012**, *108* (10), 108102.

(72) Kumar, S.; Rosenberg, J. M.; Bouzida, D.; Swendsen, R. H.; Kollman, P. A. THE Weighted Histogram Analysis Method for Free-energy Calculations on Biomolecules. I. The Method. *J. Comput. Chem.* **1992**, *13* (8), 1011–1021.

(73) Kumar, S.; Rosenberg, J. M.; Bouzida, D.; Swendsen, R. H.; Kollman, P. A. Multidimensional Free-energy Calculations Using the Weighted Histogram Analysis Method. *J. Comput. Chem.* **1995**, *16* (11), 1339–1350.

(74) Grossfield, A. WHAM: The Weighted Histogram Analysis Method, Version 2.0.10.

(75) Roe, D. R.; Cheatham, T. E. PTRAJ and CPPTRAJ: Software for Processing and Analysis of Molecular Dynamics Trajectory Data. *J. Chem. Theory Comput.* **2013**, *9* (7), 3084–3095.

(76) Lukat, G.; Krüger, J.; Sommer, B. APL@Voro: A Voronoi-Based Membrane Analysis Tool for GROMACS Trajectories. *J. Chem. Inf. Model.* **2013**, *53* (11), 2908–2925.

(77) Humphrey, W.; Dalke, A.; Schulten, K. VMD - Visual Molecular Dynamics. *J. Mol. Graph.* **1996**, *14*, 33–38.

(78) Kraszewski, S.; Bianco, A.; Tarek, M.; Ramseyer, C. Insertion of Short Amino-Functionalized Single-Walled Carbon Nanotubes into Phospholipid Bilayer Occurs by Passive Diffusion. *PLoS One* **2012**, *7* (7), e40703.

(79) Mitchell-Koch, K. R.; Thompson, W. H. How Important Is Entropy in Determining the Position-Dependent Free Energy of a Solute in a Nanoconfined Solvent? *J. Phys. Chem. C* **2007**, *111* (32), 11991–12001.
(80) Sun, D.; He, S.; Bennett, W. F. D.; Bilodeau, C. L.; Andersen, O. S.; Lightstone, F. C.; Ingólfsson, H. I. Atomistic Characterization of Gramicidin Channel Formation. *J. Chem. Theory Comput.* **2021**, *17* (1), 7–12.
(81) Kostarelos, K.; Lacerda, L.; Pastorin, G.; Wu, W.; Wieckowski, S.; Luangsivilay, J.; Godefroy, S.; Pantarotto, D.; Briand, J.-P.; Muller, S.; Prato, M.; Bianco, A. Cellular Uptake of Functionalized Carbon Nanotubes Is Independent of Functional Group and Cell Type. *Nat. Nanotechnol.* **2007**, *2*, 108.
(82) Inoue, M.; Shinohara, N.; Tanabe, S.; Takahashi, T.; Okura, K.; Itoh, H.; Mizoguchi, Y.; Iida, M.; Lee, N.; Matsuoka, S. Total Synthesis of the Large Non-Ribosomal Peptide Polytheonamide B. *Nat Chem* **2010**, *2* (4), 280–285.
(83) Itoh, H.; Inoue, M. Chemical Construction and Structural Permutation of Potent Cytotoxin Polytheonamide B: Discovery of Artificial Peptides with Distinct Functions. *Acc. Chem. Res.* **2013**, *46* (7), 1567–1578.
(84) Freeman, M. F.; Gurgui, C.; Helf, M. J.; Morinaka, B. I.; Uria, A. R.; Oldham, N. J.; Sahl, H.-G.; Matsunaga, S.; Piel, J. Metagenome Mining Reveals Polytheonamides as Posttranslationally Modified Ribosomal Peptides. *Science (80-.).* **2012**.
(85) Freeman, M. F.; Helf, M. J.; Bhushan, A.; Morinaka, B. I.; Piel, J. Seven Enzymes Create Extraordinary Molecular Complexity in an Uncultivated Bacterium. *Nat. Chem.* **2017**, *9* (4), 387–395.

Chapter 4

Conclusions

Polytheonamide B (pTB) is a channel-forming peptide toxin synthesized in bacteria. The peptide is hydrophobic with an unusual hydrophobic N-terminal blocking group (Mhe), while the peptide is folded to β-helical structure in an aqueous solution. Spontaneous “vectorial insertion” of pTB into membrane has been revealed experimentally. In the present Ph.D. thesis, the structure, fluctuations, and dynamics of pTB channel and solvent molecules inside the channel in different environments; and the energetics and dynamics of membrane insertion of pTB were investigated theoretically at the molecular level using all-atom molecular dynamics (MD) simulations.

In Chapter 2, the $\beta^{6.3}$-helical channel of pTB was examined in water, POPC bilayer, and 1:1 chloroform/methanol mixture. The average structures and fluctuations of the pTB channel in the three environments were analyzed. The validation of the parameters used for the non-standard groups in pTB was performed by comparing the average structural properties of pTB in the mixed solvent with the experimental structure obtained in the mixed solvent. The configuration and dynamics of solvent molecules inside the pore in the three environments were investigated in detail. It was found that the water molecules inside the pore show collective motions in which all water molecules tend to orient in the same direction along the channel axis, and translate by one water-water distance at a time, due to the strong hydrogen bonds between neighboring water molecules. It was suggested that such a collective behavior of water

molecules inside the pore is indispensable in understanding the ion permeation mechanism of the pTB channel. On the other hand, the motions of methanol molecules inside the pore were not correlated because of the absence of strong hydrogen bonds between adjacent methanol molecules.

In Chapter 3, the membrane insertion of pTB was examined in detail. The free energy profiles of insertion were analyzed using the replica-exchange umbrella sampling simulations. A free energy barrier of 4.3 kcal/mol was found at the membrane surface for pTB to get inserted into the membrane from bulk water. The decomposition of free energy clarified that the free energy barrier arises from the entropic bottleneck. A “shoulder” region was found in between the global free energy maximum and minimum, corresponding to the trapping of pTB in the upper leaflet of the membrane. To clarify the membrane uptake mechanism, the membrane insertion pathways of pTB were investigated in detail using unconstrained MD simulations. The simulations confirmed the experimental observation of the spontaneous “vectorial insertion” of pTB into the membrane led by the hydrophobic N-terminal. It was found that the membrane uptake of pTB from bulk water was anchored by Mhe. The overall insertion process took place in three successive phases: “landing,” “penetration,” and “equilibration” phases. The individual insertion process can occur in two possible pathways, namely “trapped” and “untrapped” insertions, according to whether or not pTB was trapped in the upper leaflet during the penetration phase. The Voronoi tessellation analysis revealed that the insertion of pTB causes only the local lateral compression of the membrane. On the other hand, the membrane thickness remained almost constant during the insertion because of small “hydrophobic mismatch.” The present results can provide useful insights to synthesize novel peptides and therapeutic drugs that can spontaneously insert into target cell membranes in a vectorial fashion.

The findings of Chapters 2 and 3 contribute to the molecular understanding of pTB and its cytotoxic action against target cell membranes. The cytotoxicity of pTB is related to its channel activity, e.g., motions of ions and water molecules, across the target cell membrane after spontaneously inserting into the membrane. Single-channel current recordings using planar lipid bilayer experiments in various ionic concentrations and membrane potentials reveal that the current-voltage curves are asymmetric with symmetric ionic concentrations across the membrane. This phenomenon is called “rectification,” i.e., the ionic flux from the C-terminal to the N-terminal is found to be higher than that from the opposite. In addition, experimental results suggest a “paradoxical” one-ion permeation mechanism such that ions permeate through the pTB channel by stepping between two binding sites in the pore, but never occupy these sites simultaneously. For the better molecular understanding of these results, the ion-permeation through the pTB channel needs to be investigated in detail, and is the subject of ongoing studies.